REDUCING HARMFUL VIBRATION OF ROTARY-WING AIRCREW SEATS USING MAGNETORHEOLOGICAL DAMPERS.

ATTÉNUATION DES VIBRATIONS DE SIÈGE D'HÉLICOPTÈRE AVEC LES AMORTISSEURS MAGNETORHEOLOGIQUES.

A Thesis Submitted to the Division of Graduate Studies
of the Royal Military College of Canada
by

Austin Gian Thind

In Partial Fulfillment of the Requirements for the Degree of
Master of Applied Science in Mechanical Engineering

December 2016

Abstract

The aim of this study was to investigate the use of magnetorheological (MR) dampers to protect rotary-wing aircrew from harmful vibration that exists in cockpits. Four semi-active control policies were developed to vary the force provided by these dampers for a given excitation state. To simulate the proposed control schemes in conjunction with the dampers, the dampers were characterized through experimental excitation and fitted to a Bouc Wen model through parameterization. A CH-124 aircrew seat is examined and a suggestion for MR damper placements is postulated. The entire system is reduced to a sprung mass-damper system for use in simulations. A base excitation similar to that found in rotary-wing cockpits and an impact disturbance were used in the simulations and the resulting accelerations of the seat were compared to determine how well each controller attenuated the external force transferred to the aircrew seat. It was found that the controllers either marginally under-performed or equally-performed compared to a damper kept at a constant minimum input current during constant harmonic vibration tests, but outperformed the passive scenario when subjected to a sudden impact disturbance.

Résumé

Le but de cette étude était d'étudier l'utilisation des amortisseurs a base magnéto-rhéologique (MR) afin de protéger l'équipage des hélicoptères contre les vibrations qui se produisent dans les cockpits. Quatre méthodes de contrôle semi-actif ont été développées. Afin de vérifier l'efficacité des méthodes de contrôle proposés, une étude expérimentale pour déterminer les paramètres d'un amortisseur a base magnéto-rhéologique a été effectuée et un modèle mathématique basé sur le modèle de Bouc Wen a été développé. Le modèle de l'amortisseur a base magnéto-rhéologique et par suite utilisé avec un modèle de siège d'équipage d'un hélicoptère de type CH-124. Une excitation ayant des fréquences similaire à celles retrouvées dans les cockpits des hélicoptères ainsi que des perturbations externes ont été utilisées dans les simulations. Les accélérations du siège ont été comparé afin d'évaluer la performance de chaque méthode de contrôle et sa capacité de réduire les vibrations transmise à l'équipage.

Contents

List of Tables

List of Figures

Nomenclature

α	Hysteresis shaping parameter
β	Hysteresis shaping parameter
$\dot{\gamma}$	Rate of shear deformation
η	Fluid viscosity
γ	Hysteresis shaping parameter
ω	Forcing frequency
ω_0	Natural frequency
τ	Total shear stress
ζ	Damping ratio
A	Hysteresis shaping parameter
A_i	Amplitude of the input
A_o	Amplitude of the response
$a_w(t)$	Frequency-weighted acceleration samples
a_{rms}	Root mean square acceleration
c_0	Damping coefficient
c_1	Damping coefficient (Modified Bouc-Wen)
c_{max}	Maximum achievable damping coefficient
c_{min}	Minimum achievable damping coefficient
c_{sky}	Variable Skyhook damping coefficient
f_0	Offset force from accumulator
f_c	Frictional force from fluid yield stress
F_d	MR damping force
I	Input current

k_0	Stiffness coefficient
k_1	Stiffness coefficient (Modified Bouc-Wen)
n	Hysteresis shaping parameter
Q	State vector weighting matrix
R	Control vector weighting matrix
s	Relative suspension displacement
T	Transmissibility
t_s	Sample time
v	Extra displacement variable for Modified Bouc-Wen
$x(t)$	Displacement of the sprung mass
$y(t)$	Displacement of the base excitation
z	Evolutionary hysteresis variable

1 Introduction

1.1 Background

Rotary-wing pilots have long suffered chronic and debilitating pain stemming from severe vibration within helicopter cockpits. However, very little has been done to address this issue, both in design of new helicopters or in retroactive modifications. Currently, only passive suppression methods in the form of seat cushions are available to provide any form of protection. Because body-types amongst aircrew vary greatly, as do the vibration levels given different flight conditions, it stands to reason that adaptable forms of vibration control are preferable and may provide better results, translating to safer working environments for aircrew. Requirements for a vibration suppression system are seriously limited by the stringent conditions within a rotary-wing cockpit. Power requirements cannot be too great, weight must be kept to a minimum, and the system must have an inherent fail-safe in the event of power loss. Taking the above into consideration, semi-active, controllable dampers appear to be an ideal candidate.

1.2 Research Objectives and Thesis Organization

The aim of this study is to investigate the potential candidacy of Magnetorheological (MR) dampers to suppress vibration in rotary-wing crew seats. The thesis is organized into five sections. Chapter 2 is a literature review of the topics to be researched. It provides background in the injury rate among rotary-wing aircrew and why the vibration they're exposed to warrants mitigation. It also investigates MR dampers and the various existing models associated with them. Finally, various control policies used in semi-active vibration control are reviewed. Chapter 3 outlines the experimental characterization of the MR damper used in this study, and the process by which the resulting experimental data was fitted to a model. Chapter 4 describes the

overall system in question, which includes the crew seat. Ways in which to incorporate the damper into the seat without requiring too many modifications are investigated, and simplifying the system for purposes of simulation is also covered. Chapter 5 develops and tests various controllers, and results are simulated using the models produced in the previous two chapters. Chapter 6 compares the advantages and disadvantages of each controller, and investigates whether or not semi-active control has merits over traditional passive methods. Finally, conclusions and recommendations for further research are presented in Chapter 7.

1.2.1 Contributions

This thesis strives to implement a model that accurately captures hysteresis into semi-active control policies. Current research uses Bingham plastic equivalent models, which are piece-wise linear and do not incorporate hysteresis. The popularity of such models stems from their ease of solving. In order to use more complex hysteresis models, the dynamic equations will be presolved in the form of lookup tables.

2 Literature Review

2.1 Injuries induced by vibration in rotary-wing aircrew

Back pain among helicopter pilots has been reported for almost 50 years. Among all occupations under review in 25 studies, the strongest association with back pain was found among helicopter pilots [1]. While back pain is generally experienced by 62% of the greater population, it currently affects over 80% of Canadian Forces helicopter aircrew [1]. The reduced wellbeing of crew members has several consequences including operational safety and efficiency. Significant costs to the military are incurred as well, as it remains the second most frequent cause for operational grounding [1]. Sources of discomfort for pilots have been attributed to poor posture and vibration. Fixed-wing aircraft have similar seating geometries but lack the vibration present in a helicopter, and have much lower rates of reported back pain amongst aircrew. It can thus be concluded that vibration poses enough harm to warrant mitigation. Currently, the Canadian Forces has only addressed the issue by providing a protocol of neuromuscular facilitation by stretching, focusing on major muscle groups such as the hips, legs and chest [1]. Although the Canadian Forces has not conducted any formal studies with respect to the prevalence of lower back pain amongst aircrew, other militaries have, and their conclusions are summarized below [1]:

The International Organization for Standardization has evaluated human exposure to whole-body vibration under the Mechanical Vibration and Shock standard ISO 2631 [2]. The standard provides a maximum weighted RMS acceleration value that the human body can tolerate for a given frequency and exposure period, and is displayed graphically in Figure 2.1.

Table 2.1: The prevalence of back pain among rotary aircrew from various national militaries.

Author	Year	Rotary-Wing Subjects	Sample Size	Prevalence of Back Pain (%)
Bongers [3]	1990	Dutch military/civilian pilots vs nonflying control group	133/228	68/17
Bridger [4]	2002	British Royal Navy pilots	185	80
Cunningham [5]	2010	Royal Air Force pilots vs civilian pilots	78/52	83/81
Froom [6]	1987	Israeli AH-1 Cobra pilots	18	72
Hansen [7]	2001	Royal Norwegian Air Force vs fixed-wing control group	105/99	51/18
Shanahan [1]	1984	U.S. Army pilots	802	73
Sheard [8]	1996	British Royal Navy aircrew vs nonflying control group	138/228	82/52
Thomae [9]	1998	Royal Australian Navy and Army pilots	131	92

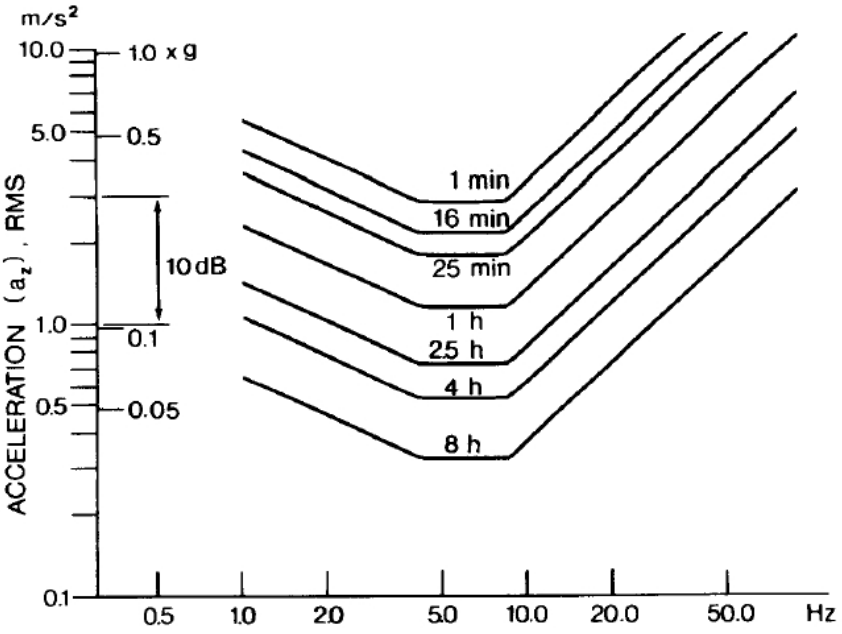

Figure 2.1: The ISO 2631 Mechanical Vibration and Shock standard [2].

According to the ISO 2631 standard, the most dangerous frequencies to human health are those that are similar to the whole body resonance frequency. Figure 2.1 suggests that $5 - 10\ Hz$, shown in the valley of each time curve, is the most dangerous frequency range. At these frequencies, internal organ damage and serious joint displacements can occur [10]. Headaches are also often associated with exposure to frequencies of 10 Hz and above. Cognitive performance can even be affected, as studies have shown that mental arithmetic and short term memory are significantly hindered at frequencies between 5 Hz and 16 Hz [10]. The human body is also especially sensitive to vibration in the vertical direction, so mitigation of vibration in the vertical direction should be the primary objective. Hiemenz [11] extensively characterized a human body seated in a helicopter seat as a lumped parameter model. The body was divided into four parts: the pelvis, upper torso, viscera and head. It was assumed that 29% of the body weight is supported by the feet. The mass of the pelvis was assumed to be 59% of the seated mass, the viscera was 9%, the upper torso was 25% and the head and neck were 7% when taking into account the helmet worn by aircrew. The parameters used for the seat

frame, cushions and human body are shown in Table 2.2.

Table 2.2: Parameters for a lumped mass approximation of a seated human body [11].

Body Part	Mass (kg)	Damping $\left(\frac{Ns}{m}\right)$	Stiffness $\left(\frac{N}{m}\right)$
Seat Frame	15	41	148299
Seat Cushion	1	390	47700
Lower Torso	48.4	2475	49340
Viscera	7.4	330	20000
Upper Torso	20.2	200	10000
Head and Neck	5.6	250	134400
Spine	-	909.1	192000

2.2 Forms of Vibration Control

2.2.1 Passive Isolation

Methods of vibration control can be divided into three broad categories: passive, active and semi-active control. Passive isolation is fixed in design and requires no power to operate. Examples include energy-absorbing materials such as those used in seat cushions and tuned-mass absorbers, which use classical spring-mass systems tuned to absorb energy at specific frequencies. Seat cushions are currently the most widely used method of isolation in helicopter cockpits, as they are simple in design, reliable, and provide shock protection in the event of a crash. Lack of adaptability means that only moderate vibration reduction is provided in certain flight conditions, and combined with the fact that a significant weight penalty is incurred, it stands that other methods should be more preferable.

2.2.2 Active Isolation

Active vibration reduction systems generally contain four main components: sensors, actuators, a power supply unit and a controller. Based on sensor input and a mathematical model of the system, the actuator opposes disturbances by generating an anti-vibration field as identical as possible to the uncontrolled vibration field but with opposite phase. These systems reduce vibration levels effectively and their adaptability makes them effective in a variety of flight conditions. Power requirements are significant, however, and stability is not guaranteed, depending solely on the performance of the controller.

2.2.3 Semi-Active Isolation

Semi-active control provides a compromise between the two aforementioned methods. It does not provide energy to the system like in active control, but it can alter the properties of the system such as damping, and thereby maintains adaptability. The secondary control force applied by the semi-active control scheme is related to the motion of the system, and stability is generally guaranteed as the control force opposes the motion of the structure. Combined with the fact that they have relatively low power requirements and will still provide some form of isolation if power is cut, semi-active control systems are favourable for use in helicopter cockpits to achieve reduction of vibration levels. A comparison of the control forces for each method is shown in Figure 2.2.

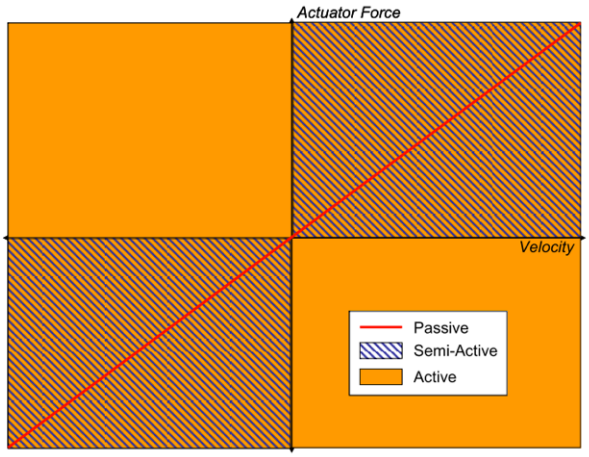

Figure 2.2: A comparison of control forces available for given vibration suppression methods.

The passive methods are represented by a linear line, suggesting that only a single force can result from a given local velocity, whereas semi-active and fully active methods encompass an area resulting in a continuous range of force scenarios for the same single local velocity. Semi-active methods only vary the damping coefficient, and can therefore provide a range of force magnitudes but are restricted to the same direction as the relative local velocity. Figure 2.2 demonstrates this by restricting the available control force to quadrants where the force and velocity have the same direction. Because fully active control can provide energy to a system, it is not constrained by the local velocities of

the system and can independently provide any force within its capabilities.

2.2.4 Helicopter-Specific Research

In 1994, the US Army Aeromedical Research Laboratory Aircrew Protection Division [10] studied various seat cushions and their performance in a simulated cockpit. Pilots were asked to sit in a crew seat with three different sets cushions for an hour each, rating their comfort levels afterwards. The cushion sets comprised of the standard ones found in an Apache AH-64 helicopter, as well as two modified with foam and air cells respectively. It was found that the prototype air-filled and foam-filled seat cushions performed better than the standard AH-64 seat cushion in terms of attenuating both lower and higher frequency vibrations. This translated to a significant improvement in comfort assessments.

Few attempts have been made to design a helicopter seat that use non-passive methods to isolate crew members from vibration. Notably, Wickramasinghe et al. attempted to reduce vibration using active control methods, claiming that MR dampers are known to provide low apparent stiffness at high frequencies and high apparent stiffness at low frequency excitations. In other words, at low velocities the damper will appear stiff and difficult to actuate, greatly reducing its damping capabilities. ISO 2631, described in Section 2.1, states that relatively low frequencies are most harmful to human health, and so semi-active control was deemed unsuitable. The recent development of smaller MR dampers by the Lord corporation have mitigated this problem, providing an alternative to the larger automotive dampers that Wickramasinghe was considering. The actuator used in this case was a stacked piezoelectric with a stroke rating of 0.2 mm and a maximum tensile force of 1000 lbs(f). Sinusoidal tone tests were used to evaluate the effectiveness of the design, generating harmonic peaks of 1/rev, 2/rev, 4/rev and 8/rev with a fundamental frequency of 5.4 Hz. Overall, the 2/rev and 4/rev harmonics were reduced by 49% and 25% respectively, while the 1/rev and 8/rev harmonics remained relatively unchanged. Hiemenz [11] observed similar limitations of older MR dampers with respect to high apparent stiffness and identified the problem was due to high off-state viscous damping and high friction. By designing an MR damper that mitigated these issues, an effective suspension system for vibration isolation was implemented in SH-60 Seahawk helicopter. Experimentally it was shown that such a system reduced 4/rev vibrations transmitted to the crew in the vertical axis by 76% while adding 1.8 kg to the seat, a net gain in weight of 8%. Hiemenz chose to use the Continuous Skyhook control scheme, to be discussed below. It should be noted that Lord Corporation has since produced

smaller MR dampers meant for low-energy applications that do not require the higher frequencies that older MR dampers needed for smooth movement. These smaller dampers were used in this study.

2.3 Magnetorheological Damper Design

Robustness and simplicity in design are important aspects of any design to be used in a rotary-wing cockpit. Any design should also be fail-safe in the event of power loss. Magnetorheological dampers meet this requirement and are a natural candidate for a semi-active device. MR dampers first debuted in 2003, developed by Delphi Automotive Systems for use in high-end automobiles. They allowed the driver a choice of a more comfortable or sportier drive and adapted to various road profiles. Unlike traditional passive viscous dampers which use oil to dissipate energy, MR dampers gain their controlability through the use of specially designed MR fluids, which comprise of two parts: a carrier fluid and ferromagnetic particles. The carrier fluid is normally either silicone oil, kerosene or synthetic oil, and must also contain additives to prevent sedimentation of the ferromagnetic particles. The particulate, 3 to 5 microns in diameter, saturates the fluid between $20 - 40\%$, and are often carbonyl, but sometimes more expensive iron-cobalt and iron-nickel alloys are used as well to achieve higher yield stresses from the fluid. These particles form linear chains when subjected to a magnetic field. The chains form parallel to the applied field and impede flow, thereby reversibly changing the fluid from a viscous liquid to a semi-solid with increasing yield strength proportional to the applied magnetic field until the fluid is magnetically saturated. At this point, an increase in magnetic flux density will have no effect on the yield strength. As MR damper design varies greatly, specifics pertaining to the Lord RD-1005-3 damper are given in Chapter 3. A general diagram showing the basic design principles of MR dampers are shown in Figure 2.3.

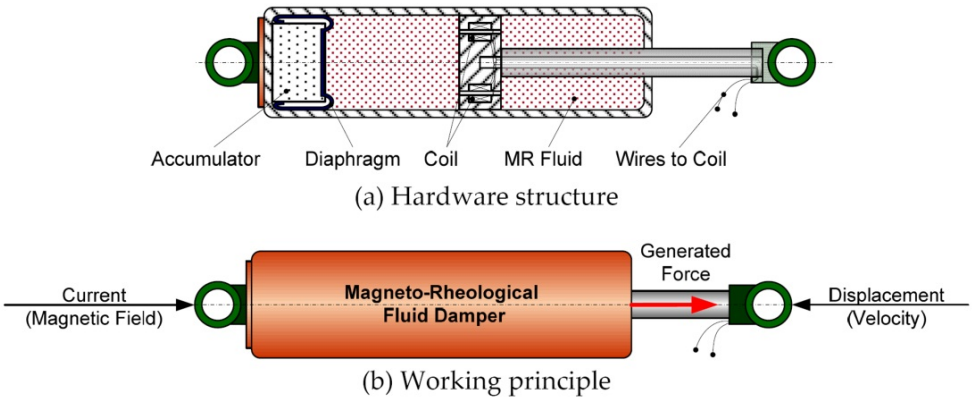

Figure 2.3: The components that make up an MR damper [12]

2.4 Vibration Classification

2.4.1 Transmissibility: The case for variable damping

Transmissibility is a measurement used in the classification of materials for vibration management characteristics, and is used for systems undergoing base excitation as shown in Figure 2.4, where $y(t)$ is the base displacement and $x(t)$ is the resulting sprung mass displacement. Transmissibility is defined as the ratio of vibrational amplitude being measured in a system to the vibrational amplitude entering a system, or simply the percentage of vibrational energy that is being transmitted through a structure.

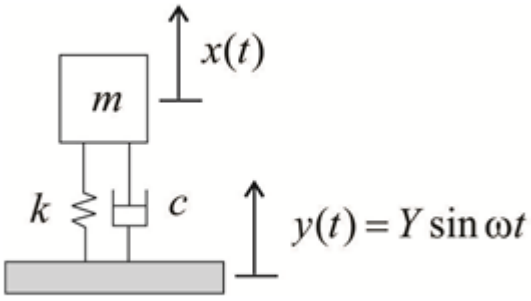

Figure 2.4: A sprung-mass system undergoing a sinusoidal base excitation [13].

A transmissibility value greater than 1 signifies amplification, whereas a value less than 1 indicates vibration isolation. As expected, the maximum transmissibility value for a system occurs when the forcing frequency and natural frequency of a system coincide. The displacement transmissibility T of a base excitation system is defined mathematically as the ratio between the amplitudes of the response and the input, A_o and A_i respectively, or more fundamentally as follows:

$$T = \frac{A_o}{A_i} = \sqrt{\frac{1 + (2\zeta\frac{\omega}{\omega_0})^2}{(1 - (\frac{\omega}{\omega_0})^2)^2 + (2\zeta\frac{\omega}{\omega_0})^2}} \tag{2.1}$$

where ζ is the damping ratio, ω is the forcing frequency of the base excitation and ω_0 is the natural frequency.

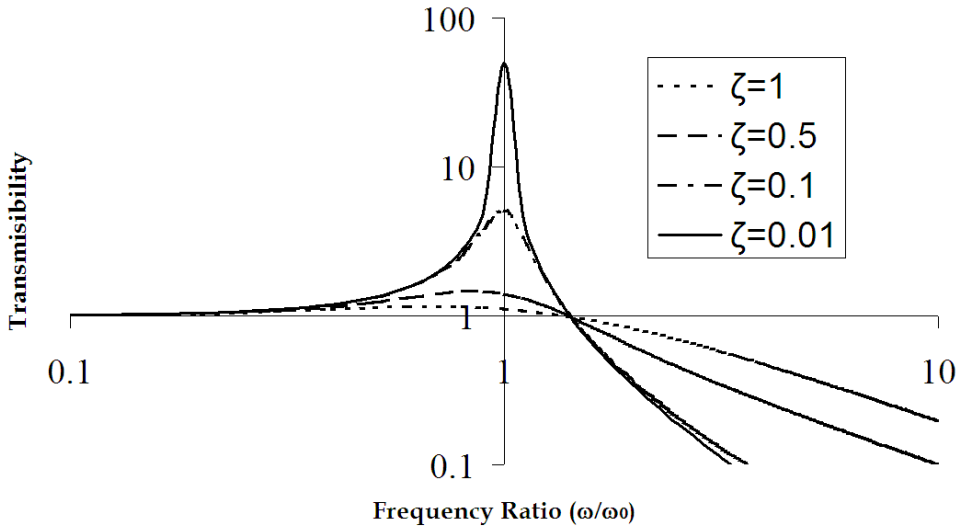

Figure 2.5: The transmissibility of a system at a given frequency ratio $\frac{\omega}{\omega_0}$ for various damping ratios ζ [13].

Various characteristic features can be seen from Figure 2.5. For forcing frequencies ω well below the natural frequency ω_0, transmissibility is approximately 1, so the motion of the mass is similar to that of the excitation. As the forcing frequency approaches the natural frequency, transmissibility is maximized for all ζ, and as ζ approaches zero the amplification reaches infinity.

2.4.2 Measurement and Analysis of Vibration

Measuring vibration requires three components: a transducer, an amplifier and a recording device. Transducers measure acceleration, velocity or displacement, however accelerometers are most commonly used for measuring vibration because of their small size and light weight. The amplifier is used to amplify the analog signal, producing an output in volts per unit of acceleration. The signal then undergoes a digital conversion and is stored on a computer. A variety of techniques are used to evaluate the response of the human body to vibration. The most commonly used method is the root mean square (RMS) acceleration because it evaluates the total energy across the entire frequency range of the vibration input [14]. RMS acceleration a_{rms} is

given by the following:

$$a_{rms} = \sqrt{\frac{1}{t_s}\int_0^{t_s} a_w(t)^2 dt} \tag{2.2}$$

where t_s is the sample time and $a_w(t)$ is the frequency-weighted acceleration samples. Frequency weightings are given by the ISO-2631 standard, and the resulting weighted RMS acceleration values can be compared to those given by the standard to evaluate the impact on a human body.

The Vibration Dose Value (VDV) method is more sensitive to peaks than the RMS method by applying the fourth power instead of the second power to the acceleration samples [14]:

$$VDV = \left\{ \int_0^{t_s} (a_w(t))^4 dt \right\}^{\frac{1}{4}} \tag{2.3}$$

Levels of perception based on VDV are provided below [15]:

Table 2.3: Levels of human perception corresponding to Vibration Dosage Values.

Level of Perception	**VDV** ($m/s^{1.75}$)
Reasonable	<0.66
Disturbing	0.66-2.38
Unacceptable	2.38-4.64
Panic	>4.64

2.5 Modelling of MR Dampers

Various modelling techniques are used to characterize MR dampers, however all fall under two broad categories: piecewise continuous models and dynamic structure models. Piecewise continuous models characterize the hysteretic properties by either equivalent linear or piecewise linear viscous damping constants, such as the commonly used Bingham plastic model and the nonlinear hysteretic biviscous model. Dynamic structure models incorporate and evolution variable, examples of which the Bouc-Wen model.

2.5.1 Bingham Plastic Model

An ideal Bingham plastic behaves as a solid until a minimum yield stress τ_y is exceeded and then exhibits a linear relation between the total shear stress

τ and shear strain $\eta\dot{\gamma}$, where η is the fluid viscosity and $\dot{\gamma}$ is the rate of shear or deformation. This is depicted by the following equation [16]:

$$\tau = \tau_y signum(\dot{\tau}) + \eta\dot{\gamma} \tag{2.4}$$

In simple terms, a Bingham plastic requires a yield stress before it begins to flow. A classic example of this is holding a bottle of ketchup upside down, requiring a shake (the yield stress) to cause flow (a rate of shear). This differs from a Newtonian fluid that will give a rate of shear for any finite value of shear stress. The difference is illustrated in Figure 2.6.

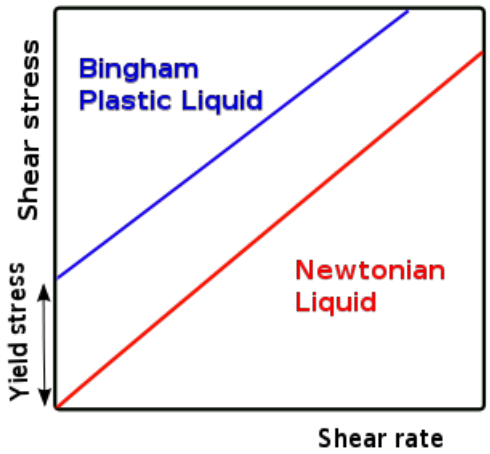

Figure 2.6: Bingham plastic flow compared to Newtonian fluid flow [16].

A mechanical Bingham model that combines viscous and Coulomb friction was developed by Stanway [17] for dampers, with the dry friction represented as a signum function on the damper velocity [16]:

$$F_d = f_c signum(\dot{x}) + c_0\dot{x} + f_0 \tag{2.5}$$

where F_d is the force supplied by the damper, c_0 is the damping coefficient, f_c is the frictional force related to the fluid yield stress, and f_0 is the offset force to account for the nonzero mean observed in the measured force due to the presence of the accumulator. Given a 2.5 Hz sinusoidal excitation with 5 mm amplitude while supplying a current of 1.5 A to the damper, K.K. Ahn [18] found the following values to model the RD-1005-3 as a Bingham plastic:

$$\begin{aligned} c_0 &= 50\ \frac{Ns}{cm} \\ f_c &= 950\ N \\ f_0 &= 75\ N \end{aligned}$$

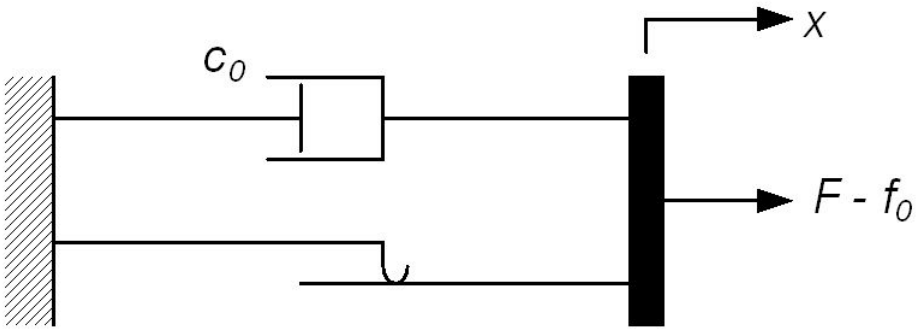

Figure 2.7: A mechanical Bingham model consisting of a viscous dashpot and Coulomb friction element connected in parallel [19].

This model does not, however, take into account the hysteresis present in dampers. The Extended Bingham model was developed by Gamota and Filisko [20] to qualitatively describe the hysteretic response of MR fluids in the pre-yield and post-yield region as well as the yield point.

2.5.2 Simple Bouc-Wen model

Structures that exhibit hysteresis produce a restoring force that depends not only on the specific moment of displacement, but also on the past events of the structure. The simple Bouc-Wen model developed by Bouc [21] in 1967 and extended upon by Wen [22] in 1976, mechanically consists of a spring, dashpot and Bouc-Wen element connected in parallel to one another as shown in Figure 2.8. The Bouc-Wen element provides hysteresis and allows the damper to be characterized as a dynamic structure, as opposed to the Bingham model which characterizes the system with a piecewise function. The mechanical configuration yields the following damping force equation:

$$F_d(t) = c_0\dot{x} + k_0(x - x_0) + \alpha z \tag{2.6}$$

where c_0 is the viscous damping coefficient, k_0 is the stiffness coefficient associated with the accumulator, x is the displacement of the system (with x_0 being the initial condition), and z is an evolutionary displacement variable that describes the internal movement within the damping fluid that gives rise to hysteresis. z given by Equation 2.7:

$$\dot{z} = -\gamma|\dot{x}|\, z|z|^{n-1} - \beta\dot{x}|z|^n + A\dot{x} \tag{2.7}$$

The parameters α ,β , n ,γ and A shape the model to the experimental data and depend on current, frequency of excitation and amplitude of excitation. More specifically, β, γ and A represent the control of linearity during unloading and the smoothness of the transition form the pre-yield to post-yield area and α represents the stiffness for the damping force associated with z.

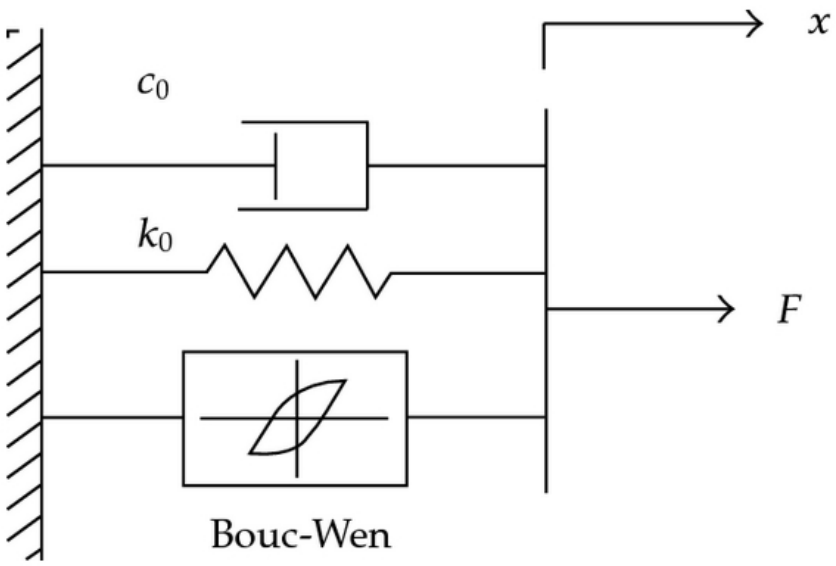

Figure 2.8: The mechanical Bouc-Wen model [23].

K.K. Ahn [18] identified the above variables for the RD-1005-3 damper as follows:

$$
\begin{aligned}
c &= 2.65 \times 10^3 \; I + 2.05 \times 10^3 \; \frac{Ns}{m} \\
k &= 1.99 \times 10^3 \; I + 5.57 \times 10^3 \; \frac{N}{m} \\
\alpha &= 2.11 \times 10^3 \; I + 1.68 \times 10^3 \; \frac{N}{m} \\
f_0 &= 0.6 \; I - 12.43 \; N \\
n &= 0.12 \; I + 1.58 \\
A &= 0.5 \times 10^5 \; I + 2.5 \times 10^5 \; kg \\
\beta &= 0.45 \times 10^6 \; I + 3.18 \times 10^6 \; m^{-1} \\
\gamma &= 0.39 \times 10^6 \; I + 3.6 \times 10^6 \; m^{-1}
\end{aligned}
$$

Note that I in this instance refers to the input current and is what allows the slope of the hysterisis curve to remain dependent on the control signal. Using these numbers and those in the previous section, force-displacement and force-velocity hysteresis curves were developed for the Bingham and Bouc-Wen models, shown in Figures 2.9 and 2.10.

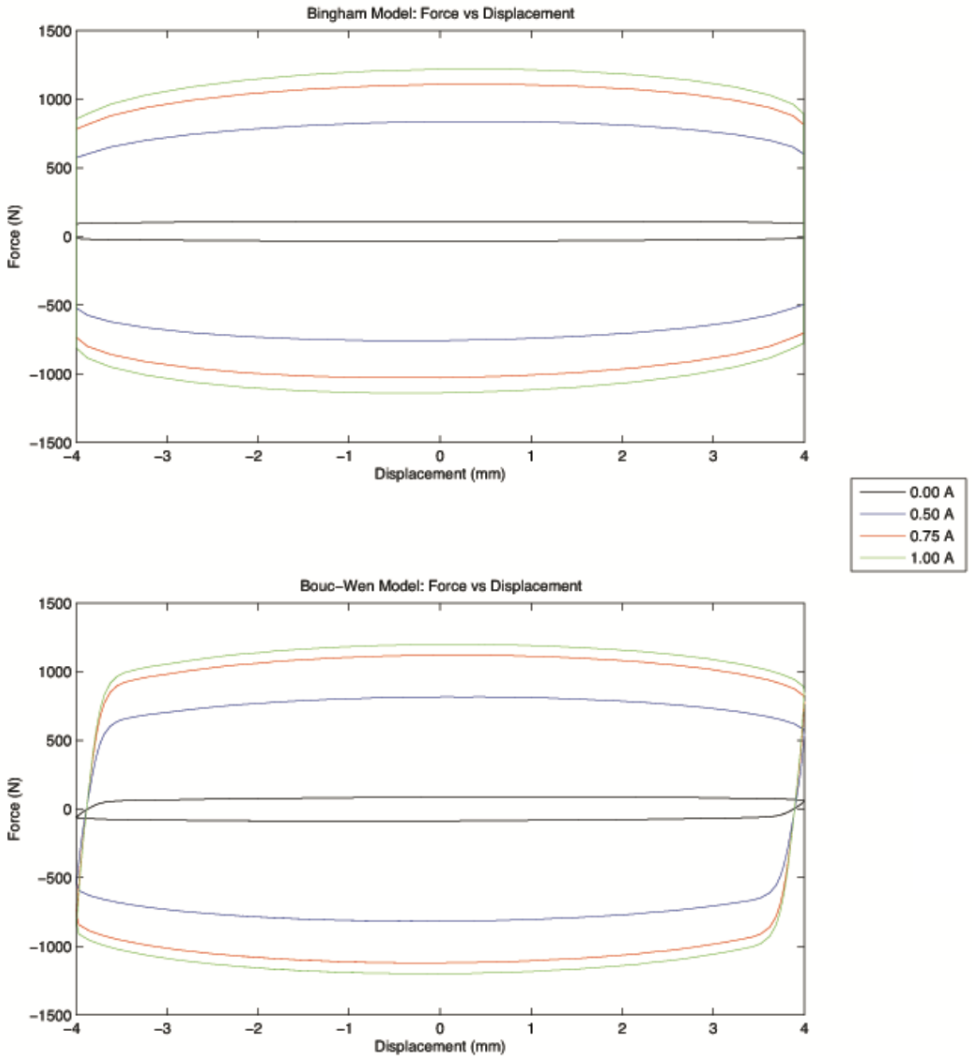

Figure 2.9: A comparison of force-displacement curves rendered by Bingham and Bouc-Wen models for an MR damper.

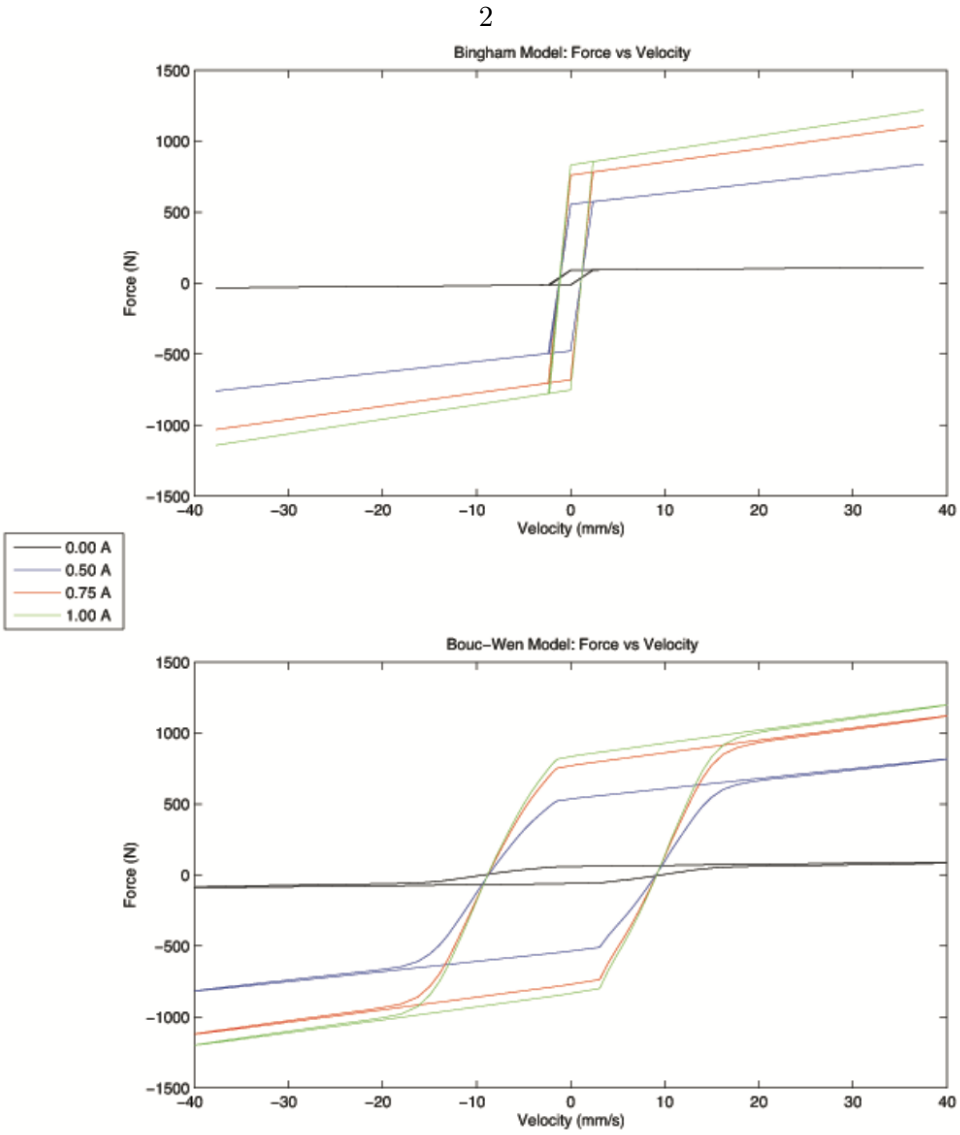

Figure 2.10: A comparison of force-velocity curves rendered by Bingham and Bouc-Wen models for an MR damper.

2.5.3 Modified Bouc-Wen Model

The modified Bouc-Wen model, developed by Spencer [12] in 1997, adds to the simple Bouc-Wen Model by placing a spring with stiffness k_1 in parallel with both a viscous dashpot with damping c_1 and the simple Bouc-Wen model connected in series, as shown in Figure 2.11. This provides the model with more flexibility and allows accurate representation of the damper's characteristics at low velocities. Because an extra degree of freedom has been added, the displacement variable v is now also necessary. For this model, the damping force is found by the following equations:

$$\begin{aligned} F_d(t) &= c_0(\dot{x} - \dot{v}) + k_0(x - v) + k_1(x - v) + \alpha z \\ &= c_1\dot{v} + k_1(x - x_0) \end{aligned} \tag{2.8}$$

$$\dot{z} = -\gamma|\dot{x} - \dot{v}|\, z|z|^{n-1} - \beta(\dot{x} - \dot{v})|z|^n + A(\dot{x} - \dot{v}) \tag{2.9}$$

$$\dot{v} = \frac{1}{c_0 + c_1}(c_0\dot{x} + k_0(x - v) + \alpha z) \tag{2.10}$$

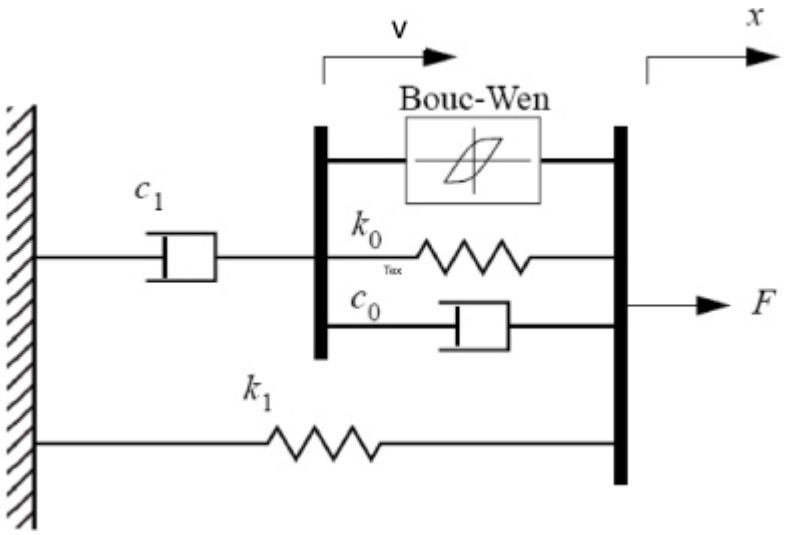

Figure 2.11: The modified Bouc-Wen model represented mechanically [24].

Using data from Sapinski [24] and comparing it to data obtained from

Ahn [18], force-velocity curves were developed for the three models discussed in this section, shown in Figure 2.12.

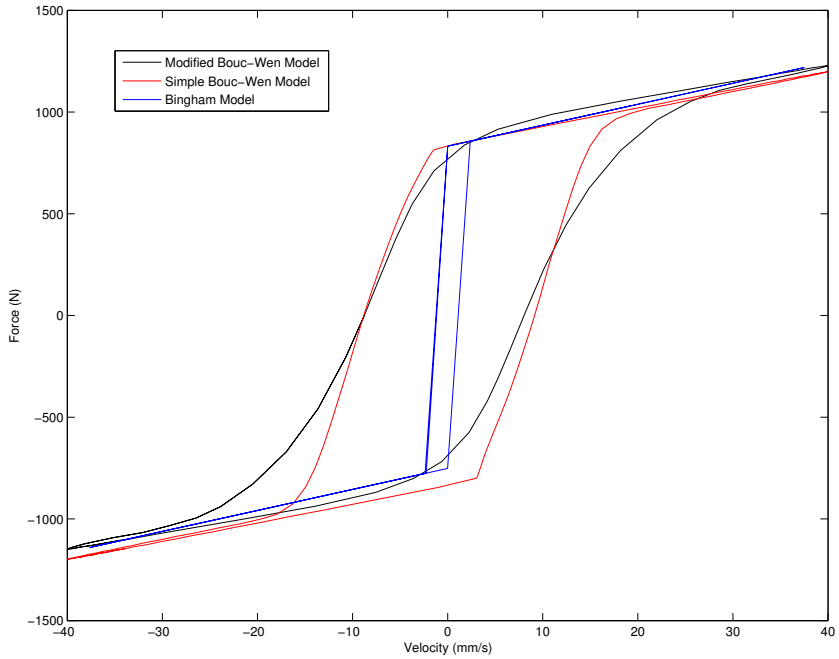

Figure 2.12: A comparison of the Bingham, simple Bouc-Wen, and modified Bouc-Wen models for an MR damper. The force-velocity graphs were produced using data from K.K. Ahn [18] and Sapinski [24].

A number of modifications have been proposed to provide an even more accurate depiction of MR dampers. These models all require experimental parameter identification, however, and thus require data and fitting before it can be considered an accurate model. A list of MR damper models, partially compiled by Sapinski [24], is shown in Table 2.4:

Table 2.4: Previously proposed models for a magnetorheological damper [24].

Modelling technique	**MR Damper Models**
Bingham Models	Original Bingham model [17] Modified Bingham model [19] Gamota and Filisko model [25] Updated Bingham model by Occhiuzzi et al. [17] Three-element model by Powell [26]
Bi-viscous models	BingMax model by Makris et al. [26] Nonlinear bi-viscous model [27] Nonlinear hysteretic bi-viscous model [27] Nonlinear hysteretic arctangent model [27] Lumped parameter bi-viscous model [27]
Visco-elastic-plastic models	General visco-elastic-plastic models [28] Stiffness-viscosity-elasto-slide (SVES) model
Hydro-mechanical model	Hydro-mechanical model [29]
Bouc-Wen models	Simple Bouc-Wen model [26] Modified Bouc-Wen model
Dahl models	Modified Dahl model Viscous Dahl model
LuGre models	LuGre Model Modified LuGre model by Jimenez and Alvarez [30]
Hyperbolic tangent models	Hyperbolic tangent model by Kwok et al
Sigmoid models	Sigmoid model by Wang et al and Ma et al
Equivalent models	Equivalent model by Oh and Onoda
Phase transition models	Phase transition model

2.6 MR Damper Semi Active Control

2.6.1 Skyhook Control

Many algorithms have been developed to control the variable damping of suspension systems, however the most prevalent technique is known as Skyhook control [31]. Theorized in the early 1970's but never implemented until the advent of MR dampers, the Skyhook strategy is preferred for its simplicity and applicability to any damper with a variable damping coefficient. It is predicated on the fact that a variable damper connected between the ground and a sprung mass is, if controlled optimally, analogous to a fictitious damper placed between a sprung mass and an absolute reference frame (fixed in the sky). This is demonstrated in Figure 2.13, however the example is for a vehicle and therefore includes two sprung masses representing the body and wheel.

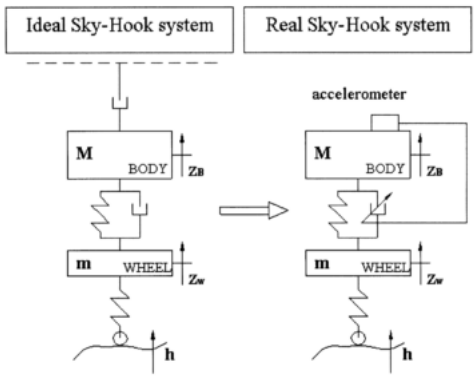

Figure 2.13: The ideal ficticious Skyhook configuration (left) realized through the use of an adjustable damper (right) [32].

A seat suspension with a single sprung mass and a damper can be approximated by the system shown in Figure 2.14.

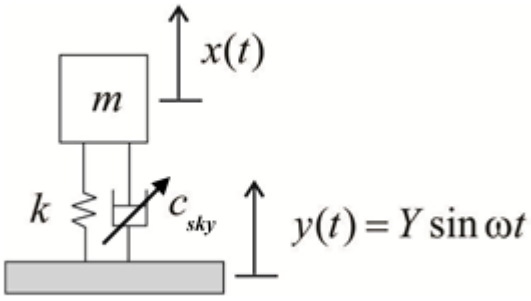

Figure 2.14: A sprung-mass system with a varibale damper undergoing a sinusoidal base excitation [13].

Figure 2.14 uses the variables x and y to represent the displacements of the sprung mass and base respectively. The relative suspension velocity is defined as the difference between these two absolute velocities, and is arbitrarily assigned to the variable $\dot{s}$:

$$\dot{s} = \dot{x} - \dot{y} \tag{2.11}$$

The variables will be used in the Skyhook control policy. The simplest variation of the Skyhook control policy is an on/off strategy known as two-state Skyhook control. It alternates between high and low damping coefficients at intervals that optimally isolate the sprung mass from the base excitation. Essentially, the control law dictates that the controlled damper deactivates, yielding a minimum damping constant c_{min} , when the body speed and suspension deflection speed have opposite signs and activates, yielding a maximum damping constant c_{max} , when the two aforementioned speeds are of the same sign [33].

$$c_{sky} = \begin{cases} c_{min} & \text{if } \dot{x}\dot{s} < 0 \\ c_{max} & \text{if } \dot{x}\dot{s} > 0 \end{cases}$$

An improved variation of the Skyhook strategy known as Skyhook Linear Approximation damper control also exists and takes full advantage of continuously variable dampers [34]:

$$c_{sky} = \begin{cases} c_{min} & \text{if } \dot{x}\dot{s} < 0 \\ sat_{c\in[c_{min}\ ;\ c_{max}]}\left(\frac{\alpha c_{max}\dot{s}+(1-\alpha)c_{max}\dot{x}}{\dot{s}}\right) & \text{if } \dot{x}\dot{s} > 0 \end{cases}$$

The saturation notation is used to demonstrate that the damping constant must be constrained to the minimum and maximum values (c_{min} and c_{max}) attainable by the given damper. The tuning parameter α can be used to adjust the emphasis on inputs from the base or sprung mass.

As mentioned in Section 2.2.4, Hiemenz noted a 76% decrease in transmitted vibration at critical frequencies when using an MR damper with an On-Off Skyhook policy compared to no damper at all. This comparison may be unfair however as a passive damper may have been able to produce similar results. Both Spelta [33] and Goncalves [31] noted a decrease of approximately 25% in the total rms acceleration when a Skyhook control policy was implemented as opposed to a passive damper.

A strategy known as Groundhook control has also been introduced by Spelta [33]. It differs from the Skyhook model in that now a fictitious damper is placed between the unsprung mass and the ground (an absolute reference frame). Unlike Skyhook control which puts emphasis on isolating the sprung mass from base excitations, Groundhook control focuses on isolating the unsprung mass from base excitations at the cost of excessive sprung mass motion. With respect to isolating aircrew in a cockpit, Skyhook control appears to be the more suitable method.

A whole host of modifications to Skyhook and Groundhook control have been proposed, such as merging the two to combine their benefits, incorporating gain scheduling and state estimation [35] , reducing dynamic jerk that may occur [36], and imposing force limits preventing damper lockup. Skyhook theory can also provide a rule base for Fuzzy Logic Controllers, expanded upon in Section 2.6.2.

2.6.2 Fuzzy Logic Control

A fuzzy logic controller (FLC) provides a formal methodology for representing, manipulating and implementing a human's heuristic knowledge about how to control a system [37]. The linguistic approach modeled after human thinking can provide a more effective capability to handle and process uncertainties found in complex systems. While classical control approaches make use of dynamic equations to model the plant, in fuzzy control the emphasis is on the use of a set of IF-THEN rules to control the plant. An FLC is comprised of the following four basic elements: the fuzzifier, the knowledge or rule base, the

fuzzy inference mechanism working on the fuzzy rules, and the defuzzifier. The fuzzifier converts the "crisp" inputs into fuzzy sets, the inference mechanism uses the rule base to infer fuzzy conclusions, and the defuzzifier converts these fuzzy conclusions into "crisp" outputs that the plant can use.

To understand fuzzy logic, one must first understand the idea of linguistic variables, linguistic values and linguistic rules. The variables are the fuzzy controller's inputs and outputs, which are often sensory information and control signals respectively. Variables change over time in the form of linguistic values. They can be described in any manner, such as "positive large", "negative small", or "zero". The linguistic variable and its corresponding value provide a method for human heuristic knowledge to be expressed. For example the mathematical representation of a velocity of 1 $\frac{mm}{s}$ could be replaced by the linguistic representation of "the speed is positive small".

Having defined the linguistic variable and values, the actual control of the system is captured in a series of IF-THEN rules using these terms. The general form of a rule is "IF premise THEN consequence". For example, given the previous linguistic variables and values, a control rule may be: "If the relative velocity is positive large and the absolute velocity is positive small, the output control signal is small." This example also serves to demonstrate that the rule does not necessarily have to involve just one premise. A fuzzy set is the set of input values that are described by a particular linguistic value. For example, velocities within the range of $0 - 10$ $\frac{mm}{s}$ may be considered "positive small" while those ranging from $5 - 15\frac{mm}{s}$ are classified as "positive large".

The fuzzy set is in turn represented by a membership function, which defines the degree of membership in that set [37]. The degree of membership is a value between 0 and 1 and corresponds to the certainty that the input can be described by that linguistic value. For example. If the degree of membership in the fuzzy set "positive large" is 1, it is absolutely certain that the value is "positive large". However if the degree is between 0 and 1 we are only partially certain that it is "positive large", in this case it can also be described to some degree by another linguistic value such as "positive small". If the degree is 0, then we are absolutely certain that the input cannot be described as "positive large". The degree to which a value is a member of each fuzzy set will depend on the shape of the membership function. Some commonly used shapes are triangular, trapezoidal, and bell-shaped. Specific examples and depictions of membership functions used in this research are shown in Chapter 5.

The fuzzifier converts the "crisp" inputs from the plant into information in the form that the inference mechanism can use to activate and apply rules. In general there are two possible choices for this mapping: singleton and non-

singleton [37]. The singleton fuzzifier is used when it is absolutely certain that the input takes on its measured value. In other words a velocity of 1 $\frac{mm}{s}$ is passed to the inference mechanism as 1 $\frac{mm}{s}$. This is the method used in this research. Non-singleton mapping delivers a probabilistic distribution to the inference mechanism and takes sensory error into account.

The inference engine interprets and applies the knowledge in the fuzzy rule base to control the plant [37]. The fuzzy inference engine performs the mapping from the fuzzy sets representing the input to the fuzzy sets representing the outputs, based on the fuzzy IF-THEN rules in the fuzzy rule base. The inference process involves two steps. The premises of all rules are first compared to the controller inputs to determine which rules apply to the current situation, commonly referred to as matching. Then conclusions are determined using the applicable rules. In general there is one conclusion for each rule. Each conclusion characterized by a fuzzy set and the degree of certainty that the input to the plant should take on a certain value. This is commonly known as the inference step.

The defuzzifier finally converts the fuzzy conclusions of the inference mechanism into actual outputs that are usable for plant control [37]. The defuzzifier maps the fuzzy sets determined by the inference mechanism to a crisp output value. In general there are three choices for this: maximum, centre of average, and modified centre of average. The defuzzification is typically more complicated than the fuzzification as there are several different conclusions that can be inferred, each to its own degree of certainty, which must be combined into usable outputs.

There are standard choices for the fuzzifier, defuzzifier and inference mechanism each with their own advantages and disadvantages. Therefore the main effort in the design process of a fuzzy logic controller lies in the synthesis of the rule base.

Sapinski [24] is credited with first developing a fuzzy logic controller for MR dampers. The absolute acceleration of the sprung mass was used here as the linguistic variable, with five linguistic values ranging from "zero" to "very large". The results were an improvement over using an on-off controller and were far more effective for a wider frequency range. Sapinski also notes that fuzzy controllers tend to regulate the input current smoothly compared to continuous controllers such as the popular Skyhook control which still acts more as an on-off controller at higher frequencies.

Fuzzy control expands on Skyhook control to provide more responses to certain conditions, such as a sudden increase in vibration or shock, and are built through trial and error [38]. Caponetto compared his fuzzy logic design to the standard skyhook method, and noted that the fuzzy controller per-

formed marginally better [38].

2.6.3 Full LQR control

Optimal control is concerned with operating a continuous-time linear system presented in state-space form at minimum cost. The cost function is defined as a sum of the deviations of selected measurements from their desired values. The control input is also included in the sum, limiting the amount of energy available to the control action. This cost J is in the form of a quadratic performance index shown in the following equation:

$$J = \frac{1}{2}\int_0^\infty (X^T Q X + u^T R u) dt \tag{2.12}$$

where Q and R are weighting matrices for the state vector X and control vector u respectively. These weighting factors place relative emphasis on each state and the input during the optimization process, and are chosen based on specified design goals. The following feedback control law provides the input that minimizes the cost function J:

$$u = -K_{LQR} x \tag{2.13}$$

where K_{LQR} is given by:

$$K_{LQR} = R^{-1} B^T P \tag{2.14}$$

and P is the symmetric positive semidefinite solution of the Algebraic Riccati equation:

$$0 = PA + A^T P + Q - PBR^{-1}BP \tag{2.15}$$

It should be noted that the Riccati equation can have more than one solution, but there is only one solution that is positive semidefinite.

2.6.4 Clipped Optimal Control

MR dampers are nonlinear due to hysteresis and time-variant because they alter the damping properties of the overall system, characteristically changing the plant that is being controller. Therefore optimal control methods cannot be applied directly. Furthermore, because damping force depends on local velocities, a damper cannot always supply the desired optimal force. To mitigate this an attenuated version of optimal control can be applied, a method known

as clipped-optimal control [39]. Essentially, the MR damper is modelled as an actuator, and the actual control force is clipped to match that of a damper, as shown in the block diagram represented in Figure 2.15.

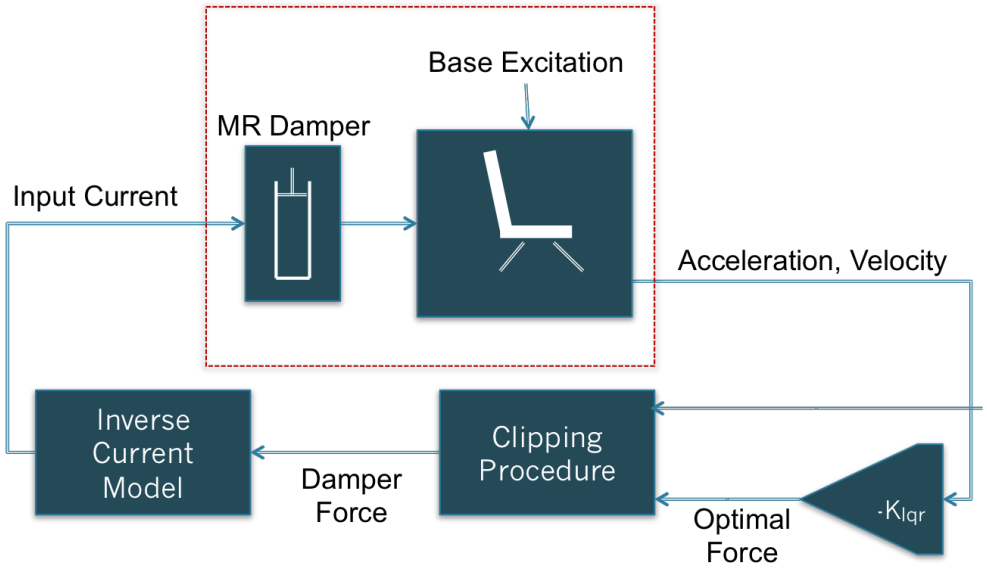

Figure 2.15: A general block diagram for clipped optimal control.

The desired damping force must be converted into a control current using an inverse model that calculates the required current to provide a damping force at a certain relative velocity. Various clipping strategies exist and should be chosen such that the damping force most closely resembles the optimal force provided by the optimal gain K_{lqr} while still remaining within the bounds of what is achievable by the MR damper. This is discussed in further detail in Chapter 5.

Dyke et al [39] first developed a clipped optimal controller in 2001 to reduce seismic movements in large structures. It was concluded that the controller performed significantly better than passive systems at reducing structural responses. Reductions in both acceleration and displacement were observed while using smaller control forces than the force produced by a passive damper.

3 MR Damper Characterization

Similar to conventional dampers, MR dampers are characterized by force-displacement and force-velocity curves that emphasize the presence of hysteresis. These curves are usually obtained experimentally by applying an external harmonic excitation and measuring the resulting force produced by the damper at given displacements and velocities. This data can subsequently be used to determine the parameters of the mathematical models used to model the behaviour of MR dampers. In this chapter, a physical description of the Lord RD-1005-3 is presented in Section 3.1.1. A detailed description of the experimental setup used to generate the force-displacement and force-velocity curves is presented in Section 3.1.2. Finally Section 3.2 introduces the fitting method used to parameterize the damper model from the experimental data to yield an accurate model and subsequent inverse model to be used in conjunction with control policies described in later chapters.

3.1 Damper Characterization

3.1.1 Lord RD-1005-3 MR Damper

The Lord RD-1005-3 MR damper examined in this thesis is comprised of several parts, including a nitrogen-charged accumulator, two MR fluid chambers separated by a piston with an annular orifice, and electromagnetic coils that produce a magnetic field when supplied with electrical current. The accumulator contains high pressure nitrogen gas and helps prevent cavitations in the fluid during normal operation. It also accounts for the volume of fluid displaced by the piston rod and thermal expansion of the fluid. Three fundamental characteristics of MR dampers are apparent from their design: the force produced by the damper is not centered at zero due to the presence of the accumulator, greater current levels supplied to the electromagnetic coil results in a greater damper force, and the change rate of force is faster at lower current levels because of the effect of magnetic field saturation. These charac-

teristics should all be evident in any experimental characterization. Specific physical characteristics for the RD-1005-3 include having a conventional cylindrical body configuration filled with 50 mL of MR fluid and a magnetic circuit with a coil resistance of 5 Ω. The enclosing cylinder is 41.4 mm in diameter and the damper is 208 mm long in its extended position with a ± 2.5 cm stroke. The device can operate within a current range from $0.0 - 2.0$ A with a recommended maximum input current of 1.0 A for continuous operation, allowing it to deliver a peak force of 2224 N at a velocity of 51 $\frac{mm}{s}$. The damper can reach at least 90% of maximum damping force during a 0.0 A to 1.0 A step input in less than 25 ms.

3.1.2 Experimental Testing

In order to properly parameterize any one of the damper models described previously in Chapter 2, accurate force data with respect to displacement and velocity is required from the damper. To obtain this, a hydraulic actuator was used to stroke a damper at a specific frequency and amplitude, as shown in Figure 3.1. Custom Clevis joints were fabricated to ensure that the damper could be supported securely to ensure accurate data collection. The actuator contains a built-in load cell and linear variable differential transformer (LVDT), sending these signals directly to the connected controller unit. The signals were a voltage, and a calibration process was used to set a linear relationship between voltage and force for the load cell, and voltage and displacement for the LVDT. For convenience, 1 V from the load cell and LVDT were chosen to equal 1000 N and 1 mm respectively.

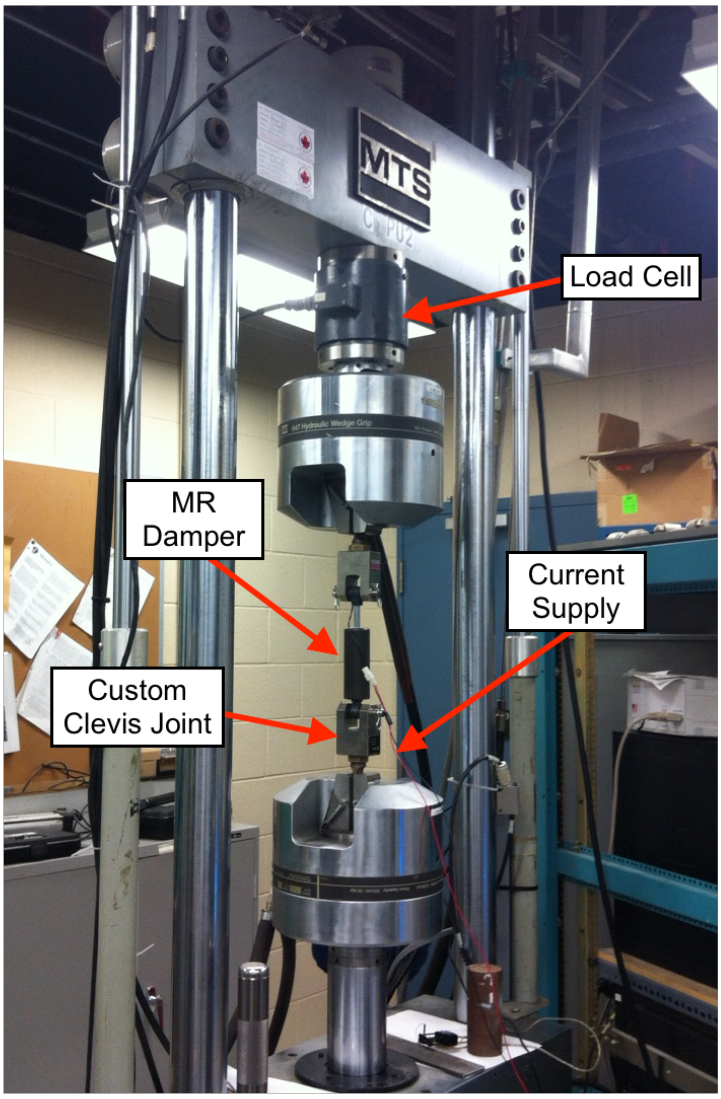

Figure 3.1: The actuator used to stroke the damper for classification.

The controller unit used in this experiment was the MTS 458 Micro-Console, shown in Figure 3.2. After selecting stroke control mode, the physical dials on the console were used to specify the set-point, zero the load cell signal, and set limits on the amplitude of oscillation. To produce a sinusoidal stroke signal, a program called FLEX was used to specify the frequency and amplitude of oscillation. For this experiment, an amplitude of 4 mm and a frequency of 4 Hz were selected. Ideally the damper would have been characterized at a frequency matching that found in a rotary-wing aircraft - approximately 5 Hz - however this was beyond the limitations of the actuator. For safety purposes, amplitude limitations were specified in both the FLEX software and the Micro-Console at 4.5 mm and 5.0 mm respectively. It was paramount that the actuator performed at a constant stroke, as the sinusoidal displacement signal would need to be derived to produce velocity data for force-velocity hysteresis curves.

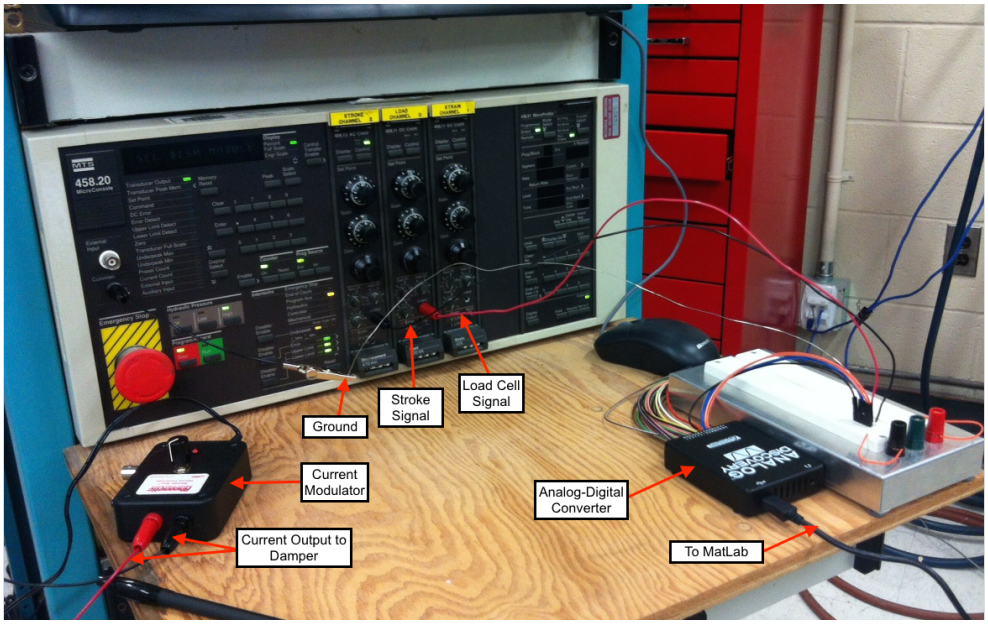

Figure 3.2: The controller used to govern the actuator

Also visible in Figure 3.2 is the Lord current-control box (bottom left) and the Analog Discovery oscilloscope and data collection unit. The current-control box was used to adjust the input current supplied to the damper for a given test cycle. The current was adjusted between 0.0 A and 1.1 A in

increments of 0.1 A, resulting in 12 trails.

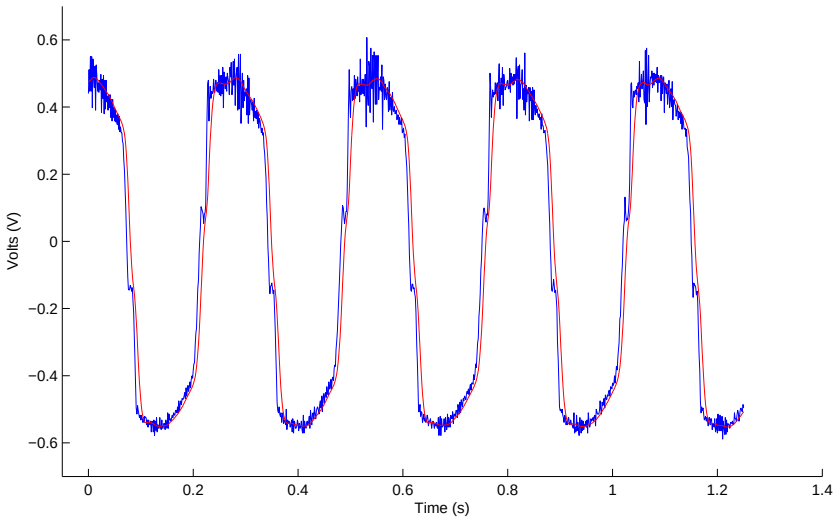

Figure 3.3: Raw data (blue) collected by the load cell, and subsequently smoother using a Butterworth filter (red), for an input current of 1.0 A and a stroke frequency of 4 Hz.

The resulting voltage data from the load cell for a supplied input current of 1.0 A is shown in Figure 3.3, and it is apparent that the unfiltered data (shown in blue) was relatively noisy. A low-pass Butterworth filter with a frequency cut-off of 6Hz was chosen to process the data before examining it. The conversion factor to yield force from voltage as determined in the calibration process was used to produce force data.

Using the filtered force data, hysteresis loops with respect to displacement and velocity were generated at each input current, shown in Figures 3.4 and 3.5 respectively. The voltage data from the LVDT did not require filtering, and was converted into displacement using the calibration factor described above and subsequently derived into velocity. The curves were similar in shape to those generated by other MR dampers - albeit much larger ones - that were investigated in the literature review.

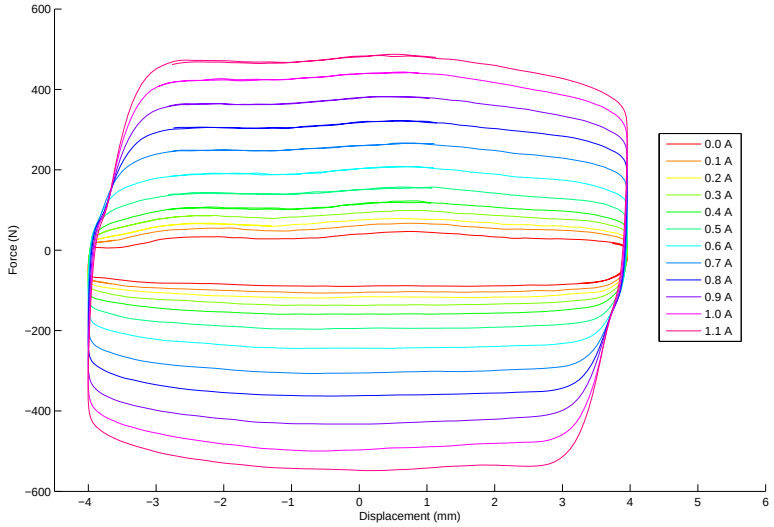

Figure 3.4: The force vs. displacement curve for the MR damper at multiple input currents

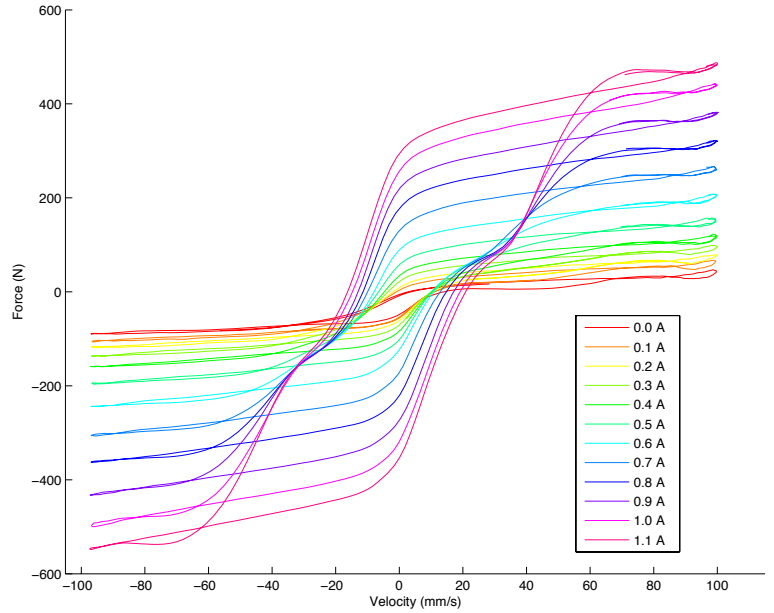

Figure 3.5: The force vs. velocity hysteresis curve for the MR damper at multiple input currents

3.2 System Identification

The data obtained experimentally was used to parameterize existing models for MR dampers that are described in Chapter 2. Inverse models were subsequently obtained and provided grounds for proper control policy implementation. This process is described in detail within this section.

3.2.1 Non-Linear Least Squares Analysis

Due to the highly non-linear nature of MR Dampers and the number of parameters that need to be determined for an accurate model, a non-linear curve fitting method was required to fit the experimental data. Non-linear least squares analysis fits a set of observations with a model that is non-linear by refining model parameters through successive iterations. Almost any function that can be written in closed form can be incorporated in a non-linear regression model and unlike linear regression, there are very few limitations on the way parameters can be used within the function. The way in which the unknown parameters in the function are estimated, however, is conceptually the same as it is in linear least squares regression [40].
Given a set of data points $(X_1, Y_1), (X_2, Y_2), ..., (X_m, Y_m)$ and a curve from the model function $Y = f(X, \mathbf{P})$, where $\mathbf{P}$ is a vector of n parameters to be determined such that the curve optimally fits the given data, the sum of squares is given by the following:

$$S = \sum_{i=1}^{m} r_i^2 \tag{3.1}$$

where r_i is the residual (error) for $i = 1, 2, ..., m$ given by

$$r_i = Y_i - f(X_i, \mathbf{P}) \tag{3.2}$$

The optimization requires that S be minimized. The minimum value of S occurs when the gradient given by Equation 3.3 is zero:

$$\frac{\partial S}{\partial \mathbf{P}_j} = 2 \sum_{i=1}^{m} r_i \frac{\partial r_i}{\partial \mathbf{P}_j} \tag{3.3}$$

where j indexes a specific parameter and ranges from 1 to n. The parameters are then refined by successive approximation.

The Bouc-Wen model, described in Section 2.5.2, was chosen as the candidate function f to be fitted, as it captured hysteresis using the least number

of parameters (also defined in the aforementioned section). For convenience, the relevant equations are presented again below:

$$\begin{aligned} F(t) &= c_0\dot{x} + k_0 x + \alpha z \\ \dot{z} &= -\gamma|\dot{x}|\, z|z|^{n-1} - \beta\dot{x}|z|^n + A\dot{x} \end{aligned}$$

The equations suggest that eight parameters will need to be determined, however n was set to equal 2 to keep the fitting process linear. This means that the parameter vector $\mathbf{P}$ will have a length of 7. The Bouc Wen model is dependent only on velocity as a variable, therefore X in this case is $\dot{x}$. The MatLab function 'lsqcurvefit' was used to parameterize the Bouc Wen model to match the experimental data set at each current interval. This exact process is described further by the flowchart depicted in Figure 3.6, and the code is available in the appendix.

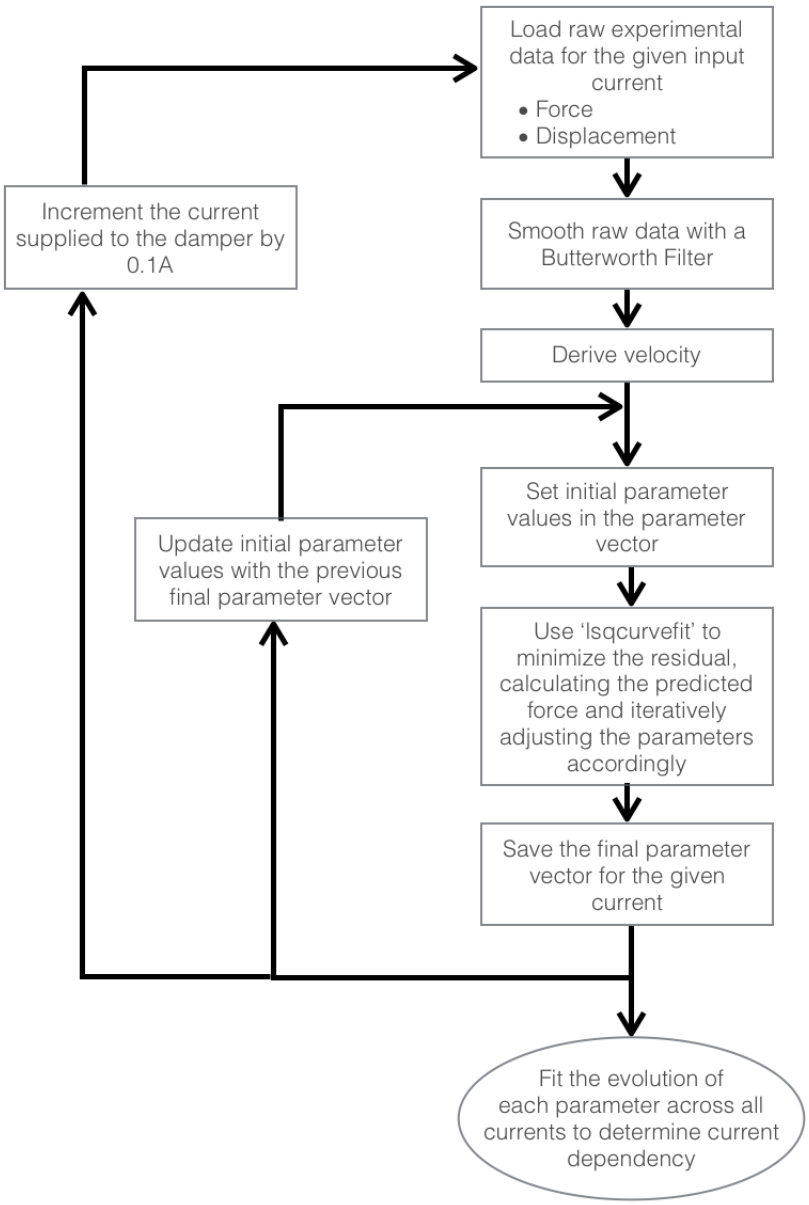

Figure 3.6: A flowchart for the methodology used in parameterizing the model to fit the experimental data.

For the data depicted in Figure 3.8, where the current was set to 1.0 A,

the following fitted parameter values were found to be as follows:

$$
\begin{aligned}
A &= 31.7313 \\
\beta &= -0.4165\ mm^{-2} \\
\gamma &= 2.0915\ mm^{-2} \\
c_0 &= 2.3264\ \frac{N \times s}{m} \\
k_0 &= 4.7250\ N/mm \\
\alpha &= 58.9512 \\
f_0 &= -29.4830\ N \\
n &= 2.013
\end{aligned}
$$

The parameters were entered into the Bouc Wen differential equations and solved using the Simulink process depicted in Figure 3.7 to yield the damping force produced for a disturbance that matched the physical disturbance applied during the experimental characterization. The resulting force-velocity results could then be compared to the experimental data, shown in Figure 3.8.

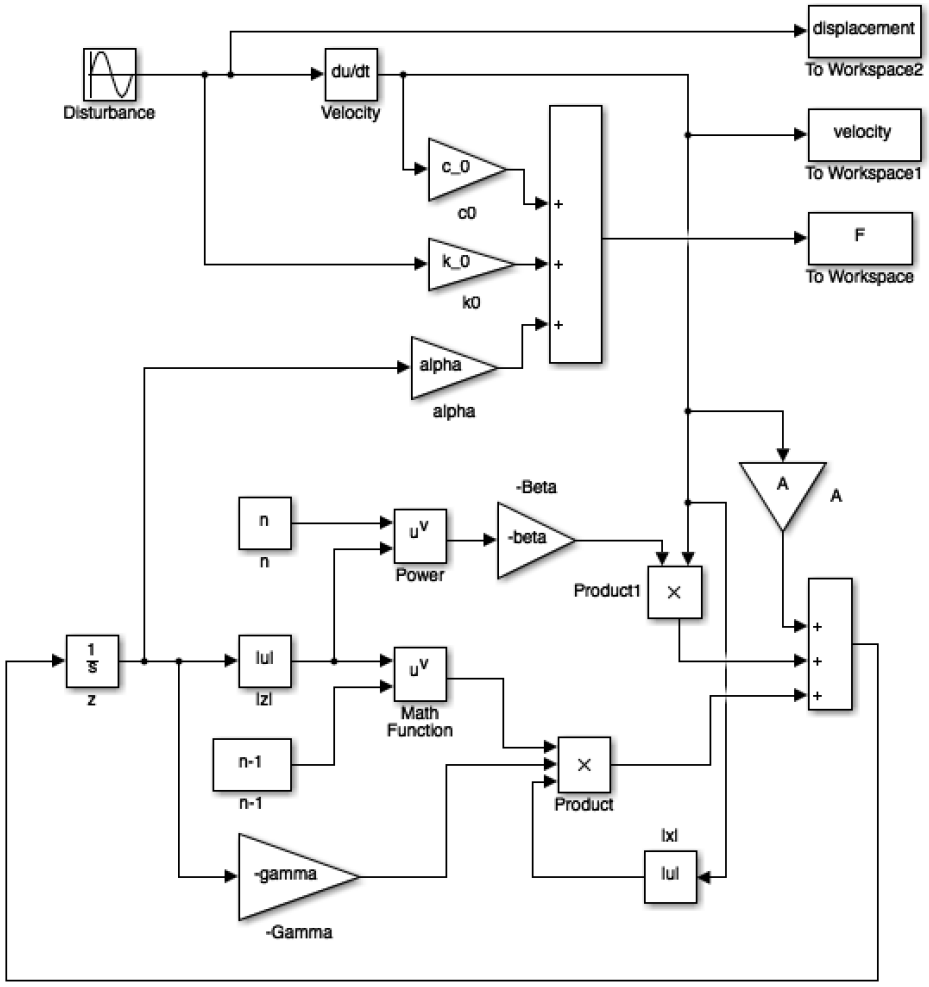

Figure 3.7: Simulink process for solving the Bouc Wen equations using the fitted parameters to yield damping force.

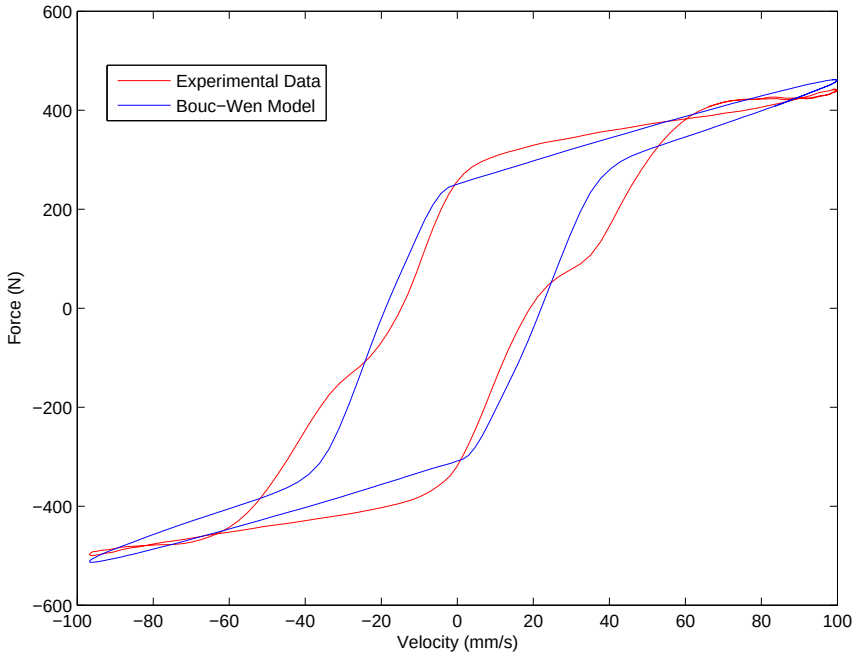

Figure 3.8: Force vs velocity data (red) and fitted Bouc-Wen model (blue) for an input current of 1.0 A.

Repeating the process for input currents ranging from 0.0 to 1.1 A in increments of 0.1 A, parameters were examined to determine whether any notable changes occurred, suggesting a current dependency. Figure 3.9 shows the evolution of the various parameters as current is increased between 0.0 and 1.1 A.

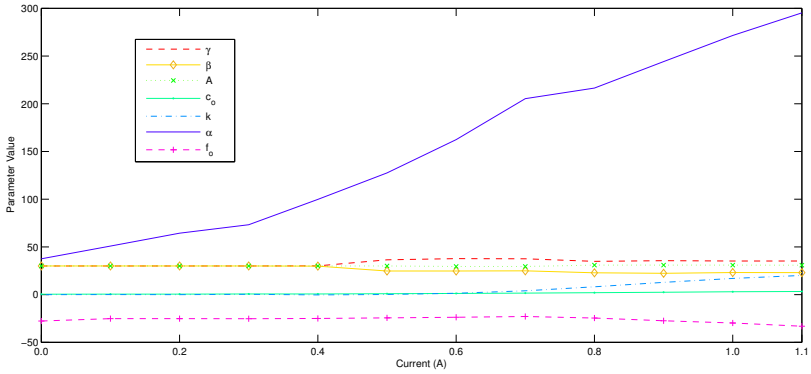

Figure 3.9: The variation of parameters in the fitted Bouc-Wen model for currents between 0.0 and 1.1 A.

The parameters that significantly exhibited current dependency are α and k_0. Fitting polynomials to each parameter for various input currents, the following parameter-current relationships are found:

$$\alpha(I) = -0.23I^3 + 5.10I^2 + 8.10I + 44.00 \tag{3.4}$$

$$k_0(I) = 0.01I^3 + 0.16I^2 - 1.40I + 1.90 \tag{3.5}$$

All other parameters were kept constant. Finally, a three dimensional surface plot of the force-velocity hysteresis curve derived from the fitted model was constructed over the entire current range, shown in Figure 3.10.

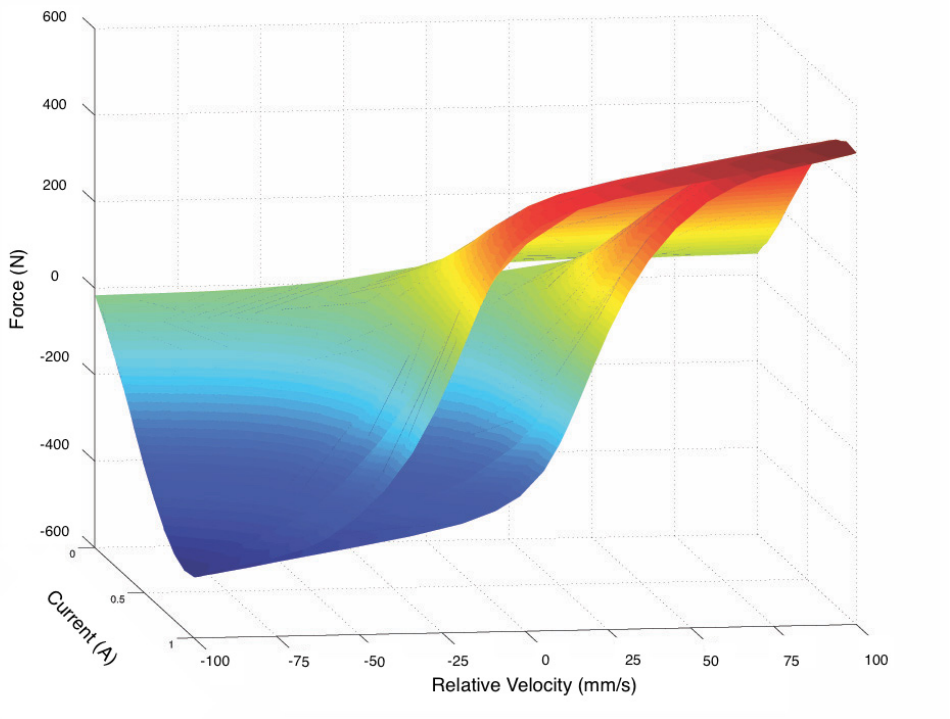

Figure 3.10: A 3D surface plot of the force-velocity hysteresis curve over the entire current range.

The surface plot demonstrates how the hysteresis curve varies for every input current. Characteristics of the MR damper exhibited during this particular test can be readily derived. Arbitrarily concerned with the damper's dynamics for positive velocities, attention is focused towards the right half of the figure. For any given current,the maximum velocity and maximum force (coincidentally, as expected) occur at the upper right edge of the plot. Since the damper was stroked at a constant frequency and amplitude, the maximum velocity remains the same for all currents at approximately 100 $\frac{mm}{s}$. The zero-force velocity intercept provides the piston velocity corresponding to zero velocity while the zero-velocity force intercept yields the damping force corresponding to zero velocity, all for a given current and excitation condition.

3.2.2 Model Portrayals in Lookup Tables

Although control algorithms provide an optimal damping force, an MR damper only accepts current as an input. Therefore a reverse model must be used to convert the desired optimal force into a corresponding current. The parametric fitted models implicitly rely on current, as was shown in Section 3.2.1, however they are intensive to evaluate. To avoid having to solve the model at every iteration to yield the needed current, the Bouc-Wen model depicted in Figure 3.10 was converted into a lookup table and interpolated, providing force values for a given current and relative velocity. Figure 3.10 clearly shows however that hysteresis causes two possible damping forces for a single relative velocity, depending on whether the damper is undergoing positive acceleration or negative acceleration. The 3D surface plot was therefore divided into positive and negative acceleration components to avoid having two possible force outputs for a given velocity input. Note that negative acceleration is this sense does not necessarily mean deceleration, so much as a rate of change in velocity in the negative direction. Transferring the data into lookup tables, the resulting discrete grids are depicted in Figures 3.11 and 3.12.

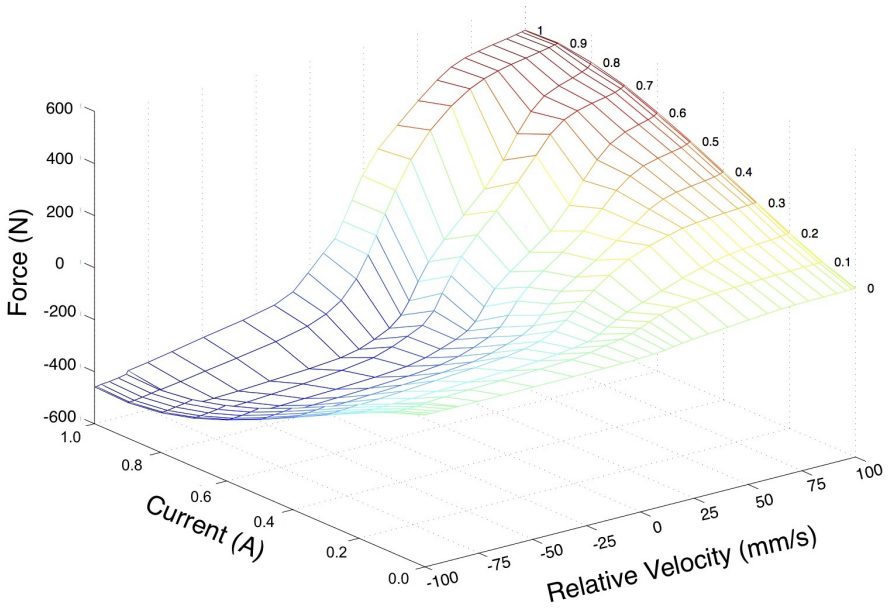

Figure 3.11: The damping force provided by a variable damper undergoing positive acceleration.

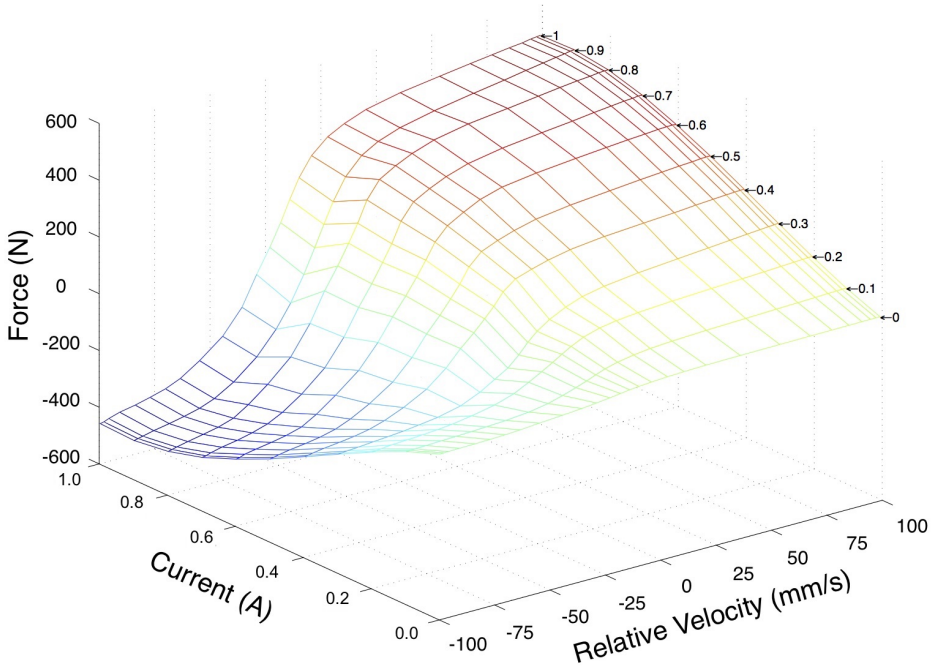

Figure 3.12: The damping force provided by a variable damper undergoing negative acceleration.

The lookup tables provide force data for known current and velocity values. Because there is a table for both accelerating and decelerating deflections for reasons relating to hysteresis as described above, relative acceleration is also required. As accelerometers are normally used and subsequently integrated to provide vibration measurements this information is readily available.

It is important to also obtain an inverse model that provides the required current to produce a given damping force. This is because most control policies yield an optimal force while the physical MR damper only accepts current as an input. To transform the tables such that current values are yielded from given force and velocity values, each table was looped through two-dimensional and one-dimensional interpolations. Performing these approximations introduced the possibility for poor accuracy of the models, however comparing the resulting values with experimental data showed that the model was still acceptable. The resulting inverse current models for accelerating and decelerating conditions are shown in Figures 3.13 and 3.14.

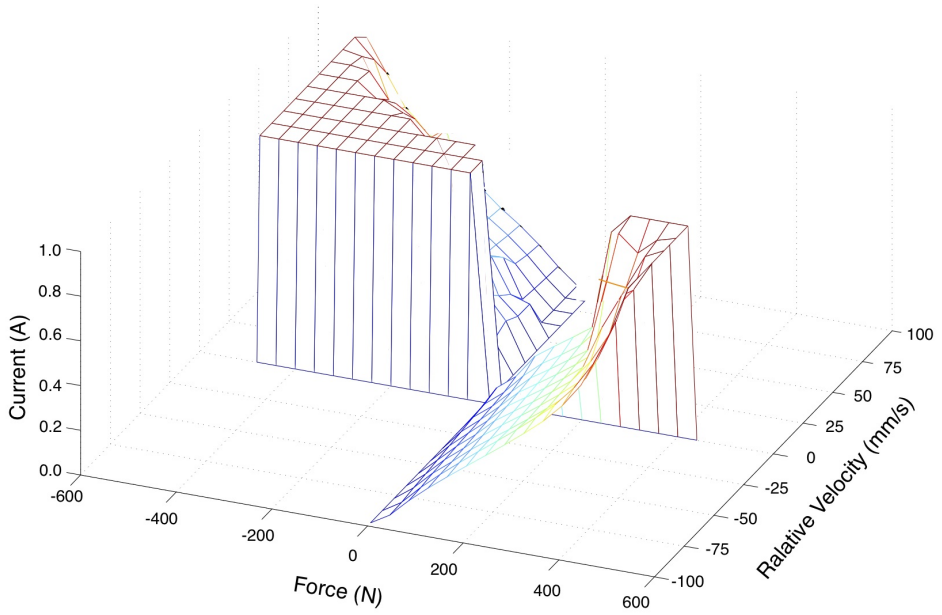

Figure 3.13: For a damper undergoing relative acceleration, the current required given a desired damping force and the suspension velocity.

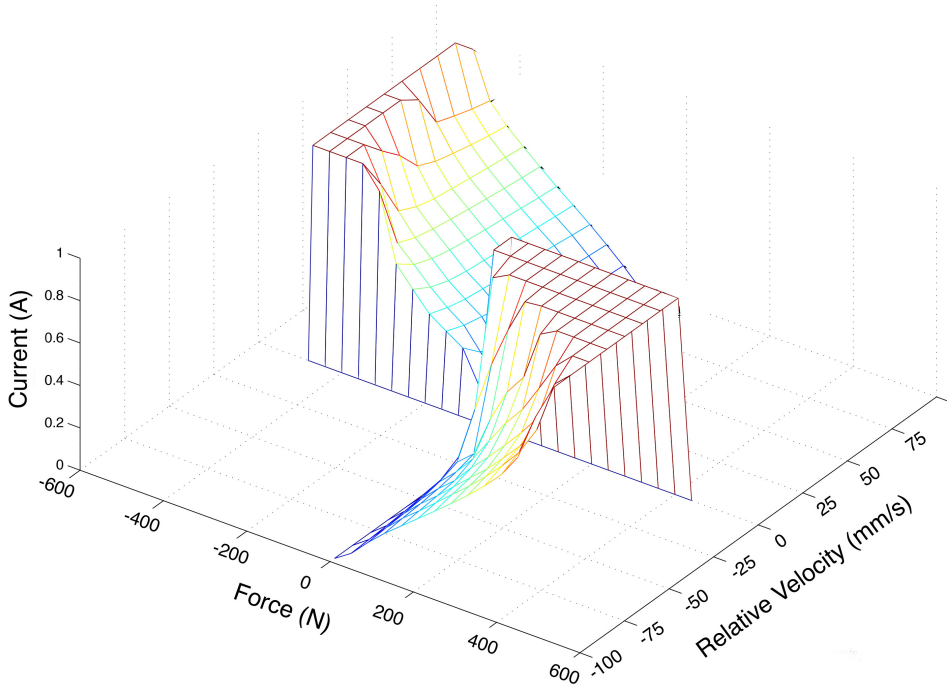

Figure 3.14: For a decelerating damper, the current required given a desired damping force and the suspension velocity.

As expected, current requirements increase as the magnitude of the damping force increases and decreases as the magnitude of the relative velocity increases for both accelerating and decelerating scenarios. Noticeable differences in surface shape do exist however, justifying the requirement to account for hysteresis. The large flat portions of Figures 3.13 and 3.14 shown in crimson are a result of operating currents for the Lord damper being unable to exceed 1.1 A.

4 Modeling of a Damped Rotary-Wing Crew Seat

This thesis explores semi-active vibration control in the context of rotary wing cockpit. It is therefore necessary to examine seat characteristics to determine how to best integrate MR dampers to create an effective suspension system. Due to the age of the CH-124 Sea King helicopter and a lack of modern approaches for steadying rotor aerodynamics that are the primary source of vibration, it was deemed a suitable platform to investigate for the purpose of this research.

Diagrams and specifications for the CH-124 Sea King aircrew seat were required to establish an accurate model, especially in the event that a physical seat could not be obtained. All technical documents are subjected to the Controlled Goods Program (CGP), presided over by Public Works and Government Services Canada. As such, registration with the CGP was carried out before receiving the material. Furthermore, because the seat was manufactured by the American-based Sikorsky Aircraft Corporation, compliance with the International Traffic in Arms Regulations also necessitated the completion of a training course in U.S. Export Controls. All images in this thesis have received explicit approval for their publishing from the relevant authorities.

Attempts were made to obtain a rotary-wing aircrew seat from the Air Force, focusing on the Sea King platform after advisement suggested the possibility of an excess of spare parts being available. Communication with Life Cycle Material Manager (LCMM) was established, however spare equipment was not deemed to be available at the time. Focus shifted to obtaining a CH-146 Griffon seat following contact with the Weapon Systems Manager (WSM) at the Calgary WSM Detachment, however all three storage aircraft under their control were being used for other purposes. Accepting that all viable options had been exhausted, plans were made to forgo experimental testing

with an aircrew seat and focus on modelling results instead.

This chapter outlines the steps taken to create a model of an active seat suspension. Depictions of a CH-124 aircrew seat are shown and a method for integrating MR dampers to form a suspension system is presented. A simplified analogous model is derived for simulation purposes, and subsequent simulations are performed with constant minimum and maximum currents given as inputs to the MR damper model to provide a baseline for comparisons of control policies.

4.1 System Description

The seat to be investigated is the pilot seat for the Sikorsky CH-124 Sea King. The complete seat is shown in Figure 4.1 [41].

Figure 4.1: The crew seat of the CH-124 Sea King [41]

A schematic is shown in Figure 4.2 [41].

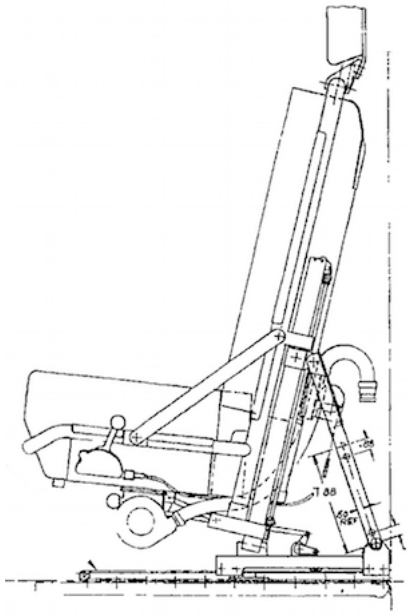

Figure 4.2: Technical drawing for a complete CH-124 Sea King. All units are in inches [41]

Stripped of cushions and adjustment mechanisms, the seat frame is shown in Figure 4.3.

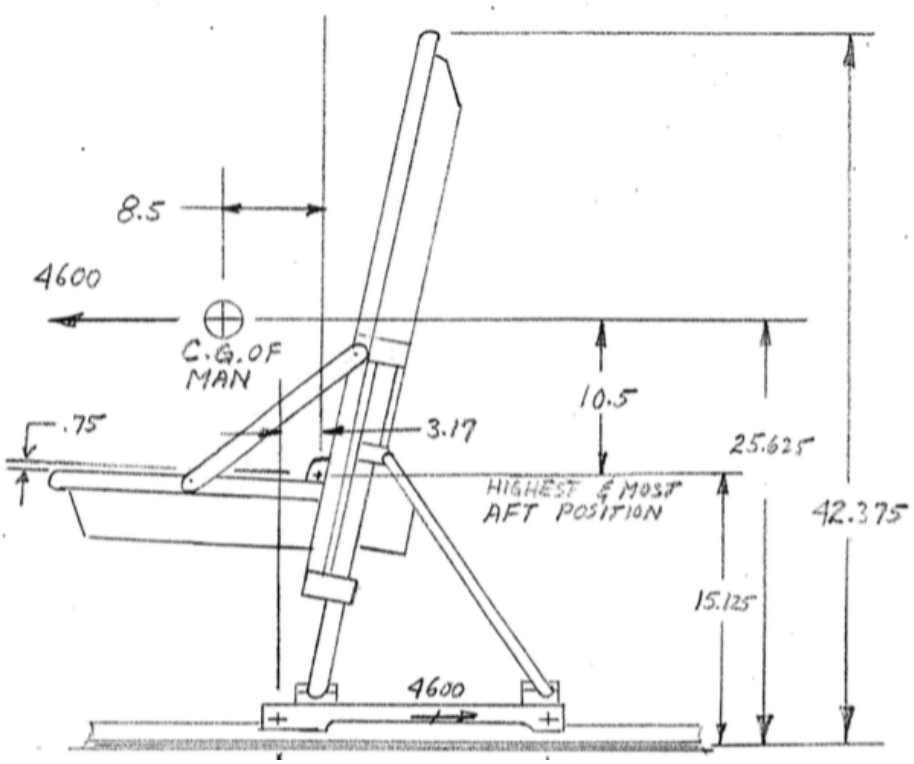

Figure 4.3: Technical drawing for a complete CH-124 Sea King

A SolidWorks model was created to include the MR dampers with the seat. This is shown in Figure 4.4. The damper placement was chosen based on minimizing modifications to the original seat. The seat slides on a rail, and by removing the lock that secures the seat to the rail and adding stiffness in the form of a spring, in conjunction with the MR damper, the seat would become a sprung mass system.

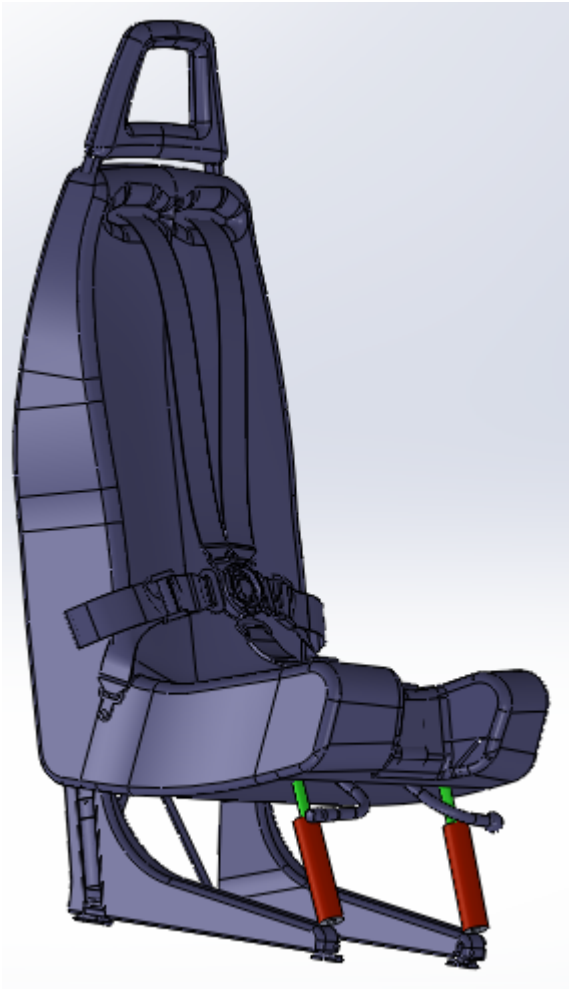

Figure 4.4: A SolidWorks drawing of the Sea King seat modified with MR dampers (shown in red and green).

Aircraft structures, including seats, must meet strict regulations set out by Airworthiness Directives. Failing to comply to static and dynamic strength criteria could result in injuries to flight crew during emergency landing conditions. Static standards generally require any seat structure to be able to withstand up to 9g's of acceleration, while dynamic, or sudden impact, loads need to be tested up to 16g's [41]. Static testing is accomplished through compression using a hydraulic press whereas dynamic testing requires a method to generate an impact pulse through acceleration, deceleration, or impact with

rebound. Facilities that can perform dynamic testing include a horizontal sled design or a vertical droptower arrangement. In an airplane crash, the impact takes place as a deceleration, so loads are applied more naturally in test facilities that create the test impact pulse as a deceleration. Since it is simpler to design test facilities to extract energy in a controlled manner than to impart energy in a controlled manner, several different deceleration sled facilities can be found. These tests are expensive and although airworthiness design is outside the scope of this research, it needs to be addressed when retrofits or modifications are introduced to aircraft structures.

As the seat is constrained to move along a rail attached to the seat back, the system can be simplified to one consisting of a sprung mass undergoing single degree-of-freedom motion and a controllable magnetorheological damper subjected to a sinusoidal base excitation. This simplified system is shown in Figure 4.5.

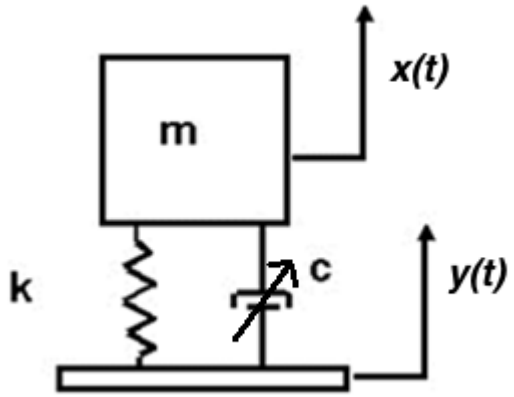

Figure 4.5: A schematic of the sprung mass - MR damper system to be controlled.

The system is given by the following equation:

$$m\ddot{x} + k(x - y) + F_d = 0 \tag{4.1}$$

$$F_d = c_0\dot{x} + k_0(x - x_0) + \alpha z \tag{4.2}$$

$$\dot{z} = -\gamma|\dot{x}|\, z|z|^{n-1} - \beta\dot{x}|z|^n + A\dot{x} \tag{4.3}$$

where x and y are the displacements of the equivalent mass and base excitation respectively, k is the equivalent stiffness, and F_d is the nonlinear, adjustable force provided by the MR damper, given by the Bouc Wen equations.

Given that the seat is constrained by rails to vertical up-down movement, the simplified system was chosen to represent half of a helicopter seat and occupant and one MR damper. Figure 4.6 depicts how the full seat model was divided to yield a half-seat model.

Figure 4.6: Division of an aircrew seat to yield a half-seat model.

The effective values for the simplified system are provided in Table 4.1.

The mass and stiffness values result in a natural frequency ω_n of 12.75 $\frac{rad}{s}$ or 2.03 Hz. With a base excitation ω of 5 Hz, the frequency ratio $\frac{\omega}{\omega_n}$ is 2.46.

Table 4.1: Force and Displacement results summarized for each control scenario.

Mass	80 kg
Stiffness	13 $\frac{N}{mm}$
Damping	Single Lord RD 1005-3 MR Damper

4.2 Constant Input Current Simulations

Now that a damper model has been developed, it can be incorporated into the mass-spring-damper seat suspension model. To create a reference point for the controllers to be discussed subsequently, the system was simulated with constant minimum and maximum input currents of 0.0 A and 1.0 A respectively. Because the input currents are kept constant, a control component is not required. Figure 4.7 depicts a flowchart for simulating the results for constant input scenarios.

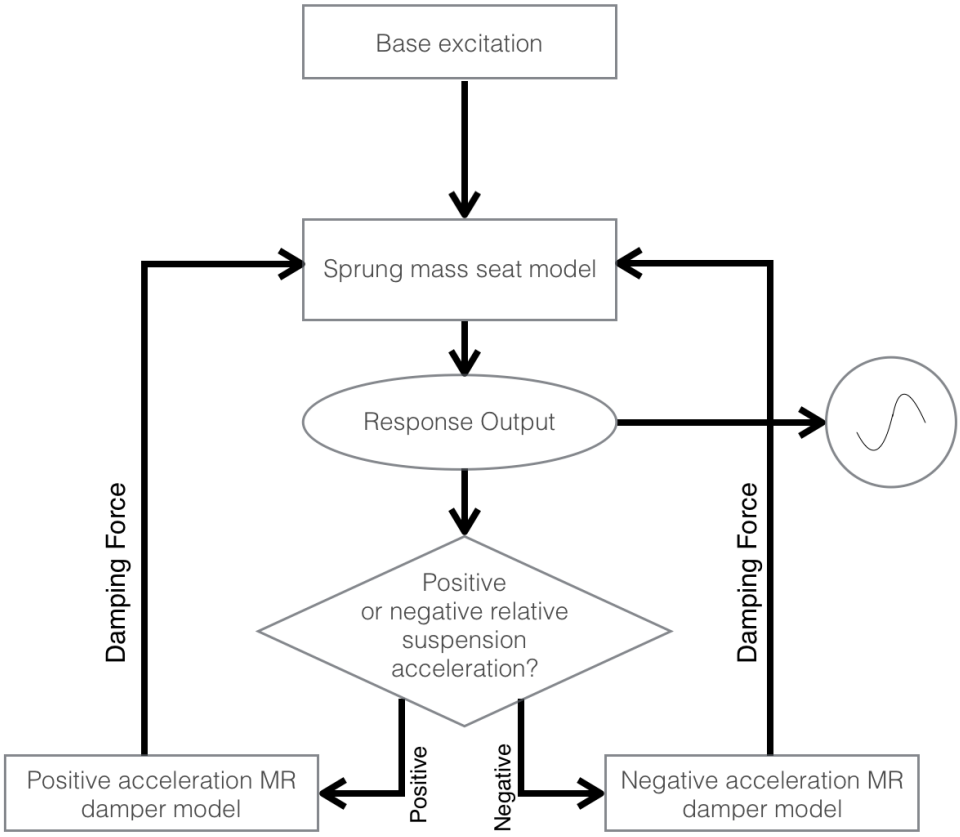

Figure 4.7: Flow diagram for the simulation of constant input current scenarios.

The resulting displacement data is shown in Figures 4.8 and 4.10, and the corresponding damping forces in Figures 4.9 and 4.11. The output in both cases is shifted up by $2mm$ relative to the base excitation in large part due to the sudden in upward force from the sinusoidal base excitation, but also because of the nitrogen accumulator which constantly supplies an upward force of 40 N.

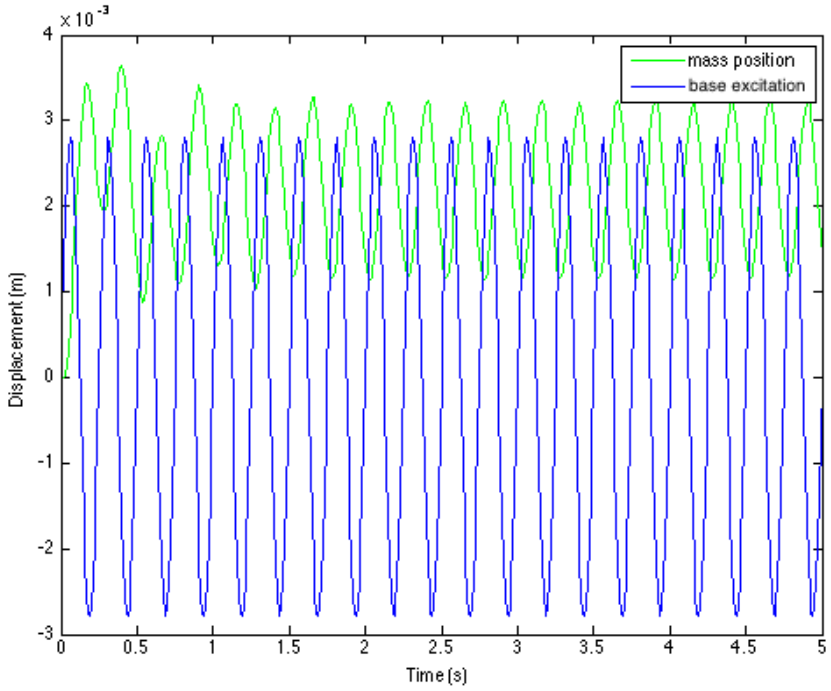

Figure 4.8: Displacement of the half-seat model with minimum constant damping.

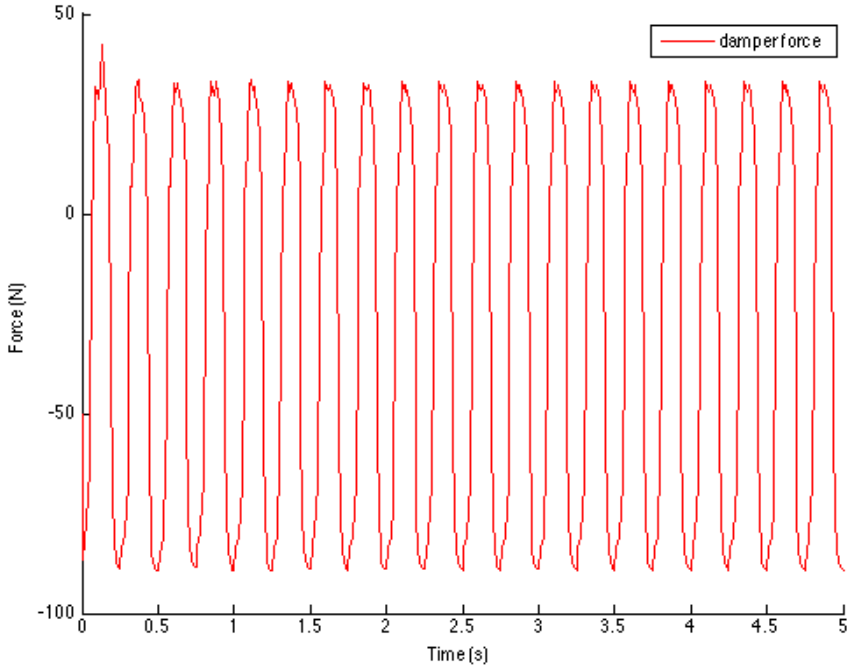

Figure 4.9: The force exherted by the MR damper with minimum input current.

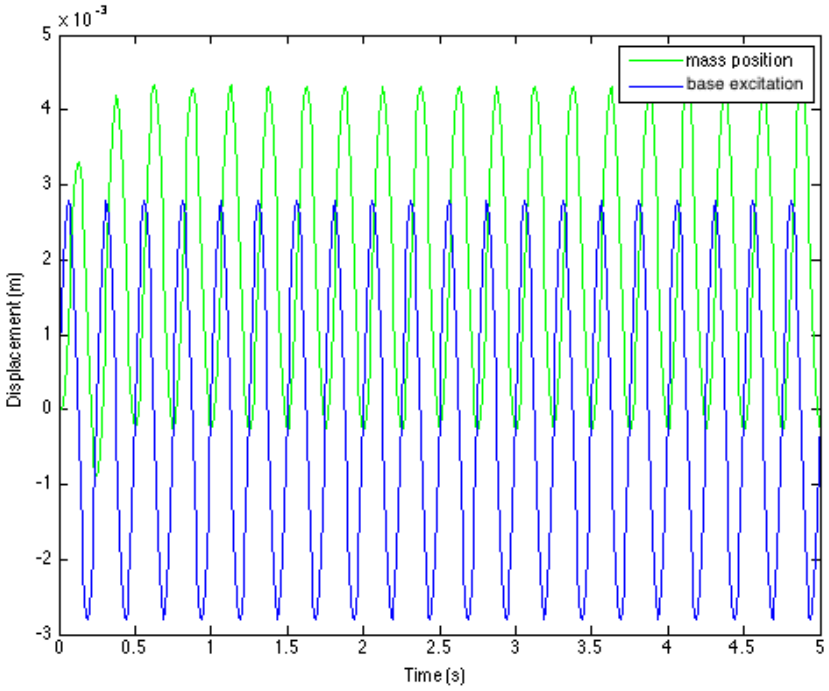

Figure 4.10: Displacement of the half-seat model with maximum constant damping.

The displacement of the mass undergoing maximum damping follows the base excitation closely, exhibiting less lag than the minimum damping case as is to be expected.

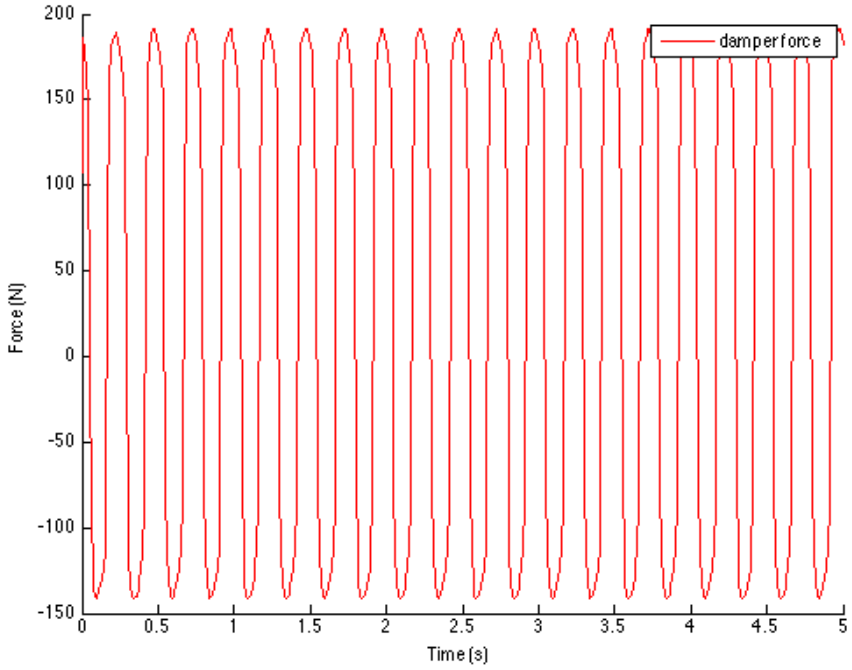

Figure 4.11: The force exherted by the MR damper with maximum input current.

A comparison of accelerations for the sprung-mass at different damping levels is shown in Figure 4.12:

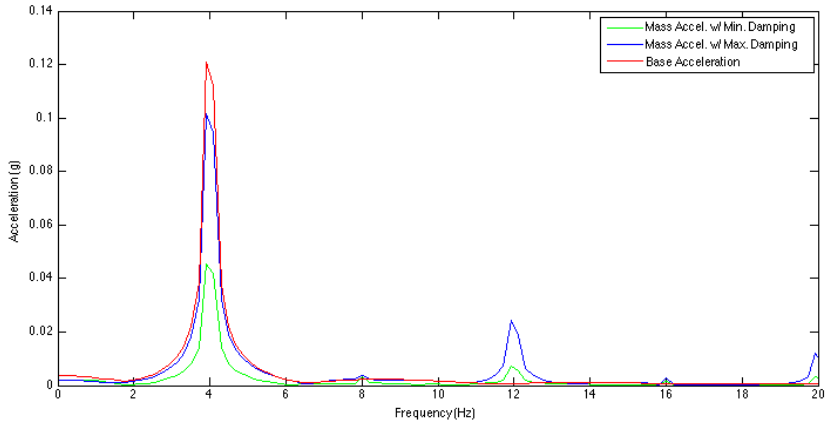

Figure 4.12: A comparison of accelerations for the sprung-mass at different damping levels.

Referring to Figure 4.13, which gives transmissibility values for various damping and frequency ratios, it can be seen that lower damping ratios result in lower transmissibility values at a 2.46 frequency ratio calculated in Section 4.1. Thus it can be expected that a lower constant input current to the damper will provide more favourable vibration isolation than higher inputs.

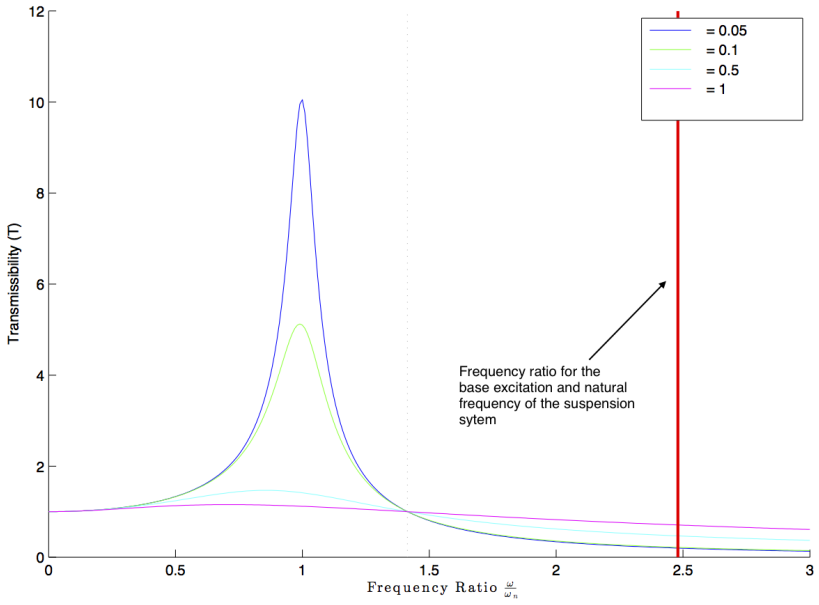

Figure 4.13: Transmissibility values for the frequency ratio observed in the excited system in question (shown in red).

5 MR Damper Semi Active Control

Taking advantage of the adaptability of MR dampers requires a control policy to be put in place. This is done generally as shown in the block diagram represented in Figure 5.1. The controller functions by determining the optimal damping force that isolates the sprung mass from vibration for a given state.

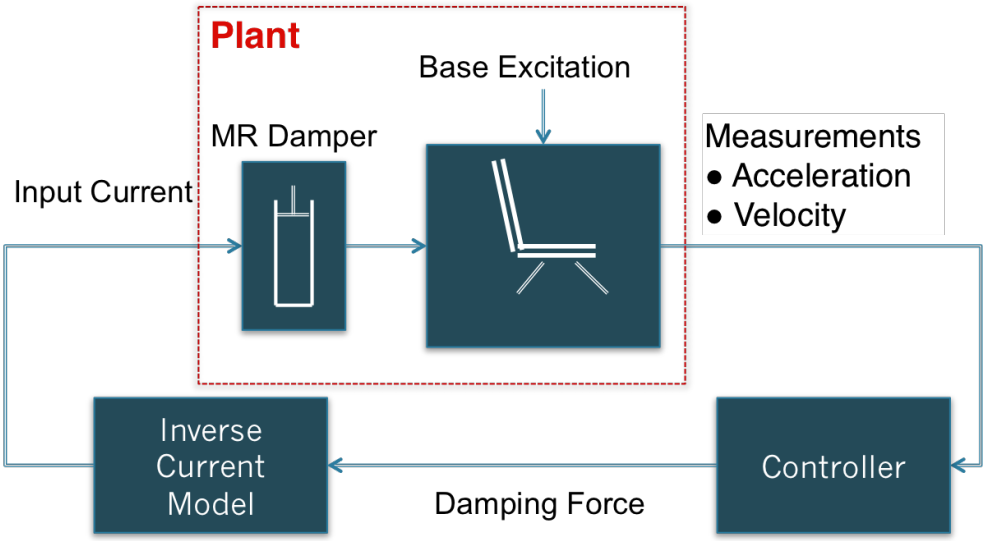

Figure 5.1: This block diagram shows the closed-loop system that results when a control policy is introduced.

The plant is comprised of the MR damper and seat. Accelerometers provide inputs for the controller in the form of relative suspension acceleration

and, following differentiation, relative suspension velocity and absolute seat velocity. The controller uses the local velocity data to determine the optimal damping force that the MR damper is capable of providing. The desired damping force must be converted into a control current using an inverse model that calculates the required current to provide a damping force at a certain relative velocity. This current control signal is sent to the MR damper, affecting an alteration within the plant in response to the base excitation.

5.1 Skyhook Control

As shown in Section 2.6.1, the Skyhook Linear Approximation control method takes full advantage of continuously variable dampers [34], and is restated here for convenience. Again, $\dot{s}$ represents the relative suspension velocity, or the difference between the absolute sprung-mass velocity $\dot{x}$ and the absolute base excitation velocity $\dot{y}$.

$$c = \begin{cases} c_{min} & \text{if } \dot{x}\dot{s} < 0 \\ sat_{c \in [c_{min}\ ;\ c_{max}]} \left(\frac{\alpha c_{max} \dot{s} + (1-\alpha) c_{max} \dot{x}}{\dot{s}} \right) & \text{if } \dot{x}\dot{s} > 0 \end{cases}$$

Figure 5.2 is a surface plot that visualizes how the Skyhook control policy varies the damping coefficient depending on the absolute seat velocity and the relative suspension velocity. As the defining equations above would suggest, the damping coefficient is increased when the two velocities are either both positive or both negative. Conversely they're at a minimum when both velocities are in opposing directions.

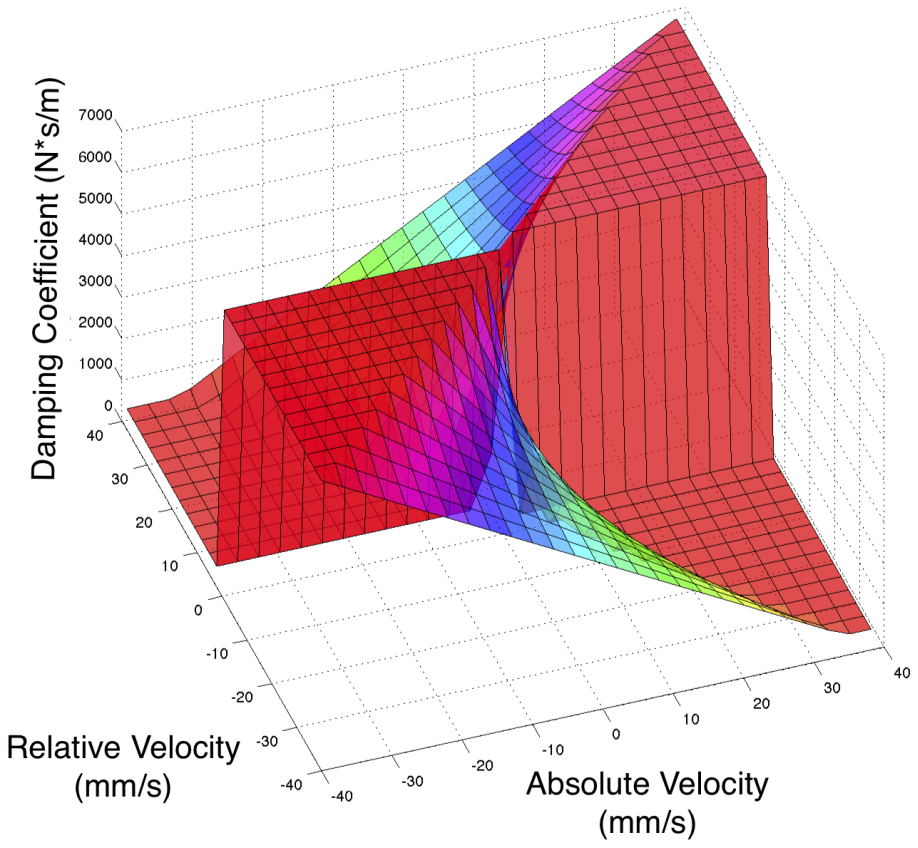

Figure 5.2: The continuous Skyhook control policy governing the change in variable damping coefficient c with respect to absolute and relative velocities, $\dot{x}$ and $\dot{s}$.

If the MR damper model includes hysteresis as the Bouc-Wen model does, it is difficult to interpret a damping coefficient c. It is therefore useful to convert c_{sky} into a controllable damping force F_d using the simple relation:

$$\begin{aligned} F_d &= c_{sky}\dot{s} \qquad (5.1) \\ &= \begin{cases} F_{min} & \text{if } \dot{x}\dot{s} < 0 \\ sat_{F_d \in [F_{min}\ ;\ F_{max}]}\ \alpha F_{max}(\dot{s}) + (1-\alpha)F_{max}(\dot{x}) & \text{if } \dot{x}\dot{s} > 0 \end{cases} \end{aligned}$$

This variation of Skyhook control allows for the incorporation of a hysteresis model when determining maximum and minimum damping forces. $F_{max}(\dot{s})$ represents the force provided by the damper at the given suspension velocity $\dot{s}$ with maximum current supplied, whereas $F_{max}(\dot{x})$ is a theoretical force value for a damper subjected to maximum input current and a relative velocity equaling the absolute sprung-mass velocity. The saturation condition is added to ensure that the final controllable damping force F_d remains within what the MR damper is capable of producing.

Figure 5.3 is a surface plot of the ideal controllable damping force for given relative and absolute velocities ($\dot{s}$ and $\dot{x}$ respectively). It demonstrates traits that are shared by all MR dampers, namely that the available damping force is constrained by the local suspension velocity of the system. Referring to Figure 5.3, it can be seen that no damping force is available when the suspension velocity is zero, irrespective of the seat velocity.

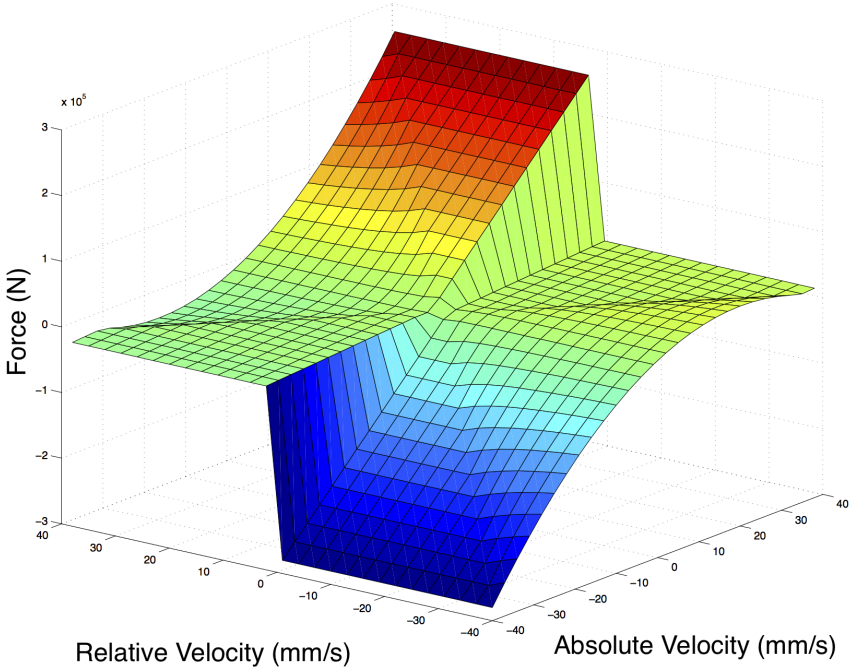

Figure 5.3: The Continuous Skyhook control policy governing the change in variable damping force F_d with respect to absolute and relative velocities, $\dot{x}$ and $\dot{s}$.

Using the control law stated in Equation 5.2 as well as the damping force model and reverse current model that account for hysteresis, a response can be generated as shown in Figure 5.5. The method in which the various control and modelling blocks were integrated are described by the flowchart in Figure 5.4, and the relevant code can be found in the appendix.

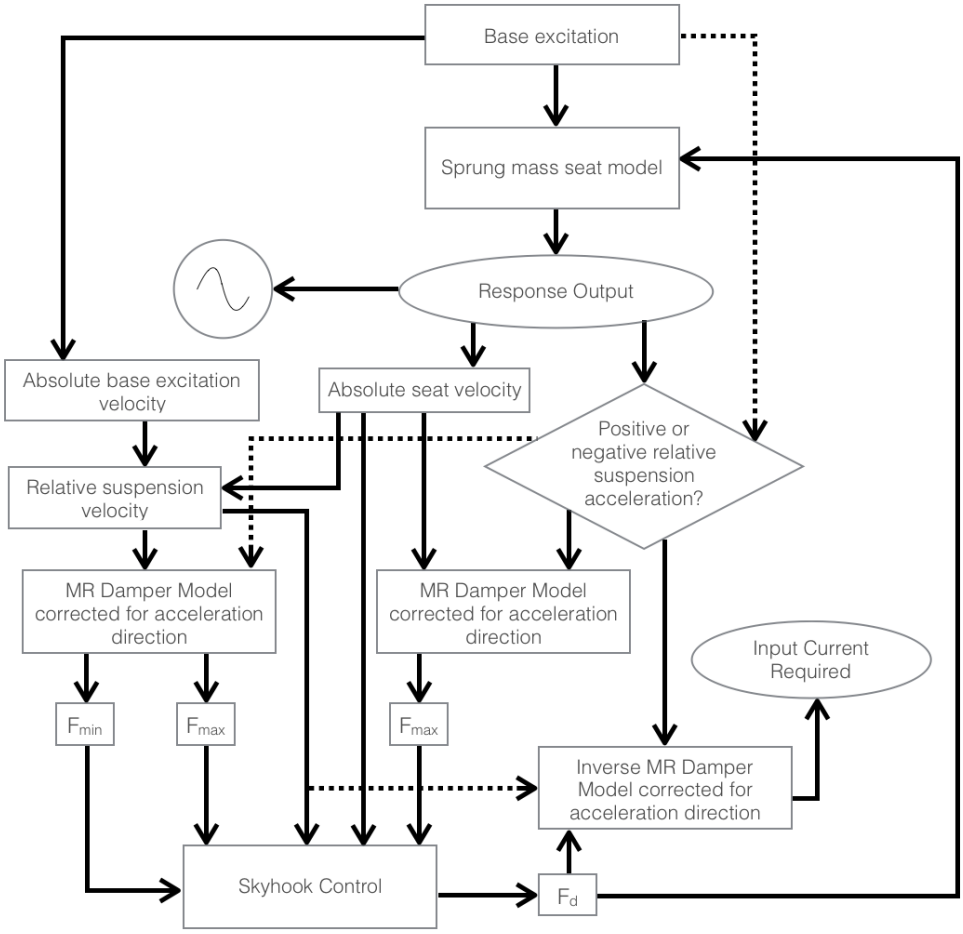

Figure 5.4: Flowchart representing the simulation process for Skyhook control.

Note that the dotted arrows in Figure 5.4 are not of significance and only serve to prevent confusion with overlapping connectors.

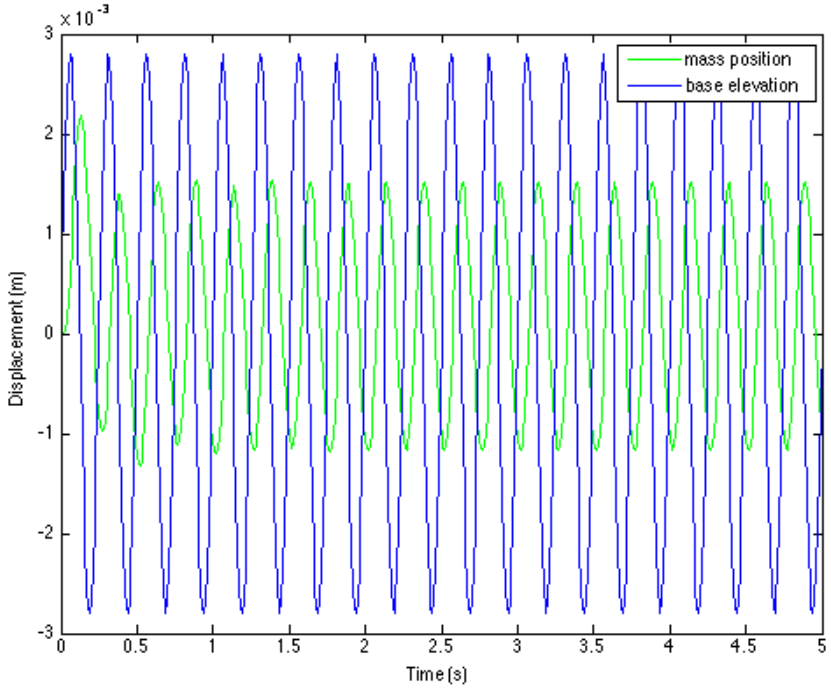

Figure 5.5: Displacement of the sprung mass governed by skyhook control.

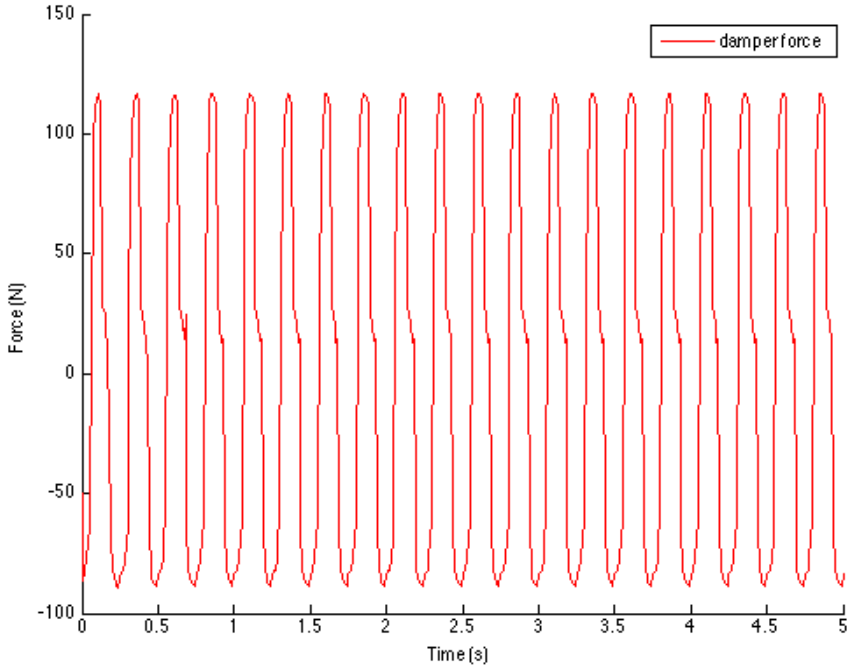

Figure 5.6: The force produced by the MR damper when governed by Skyhook control.

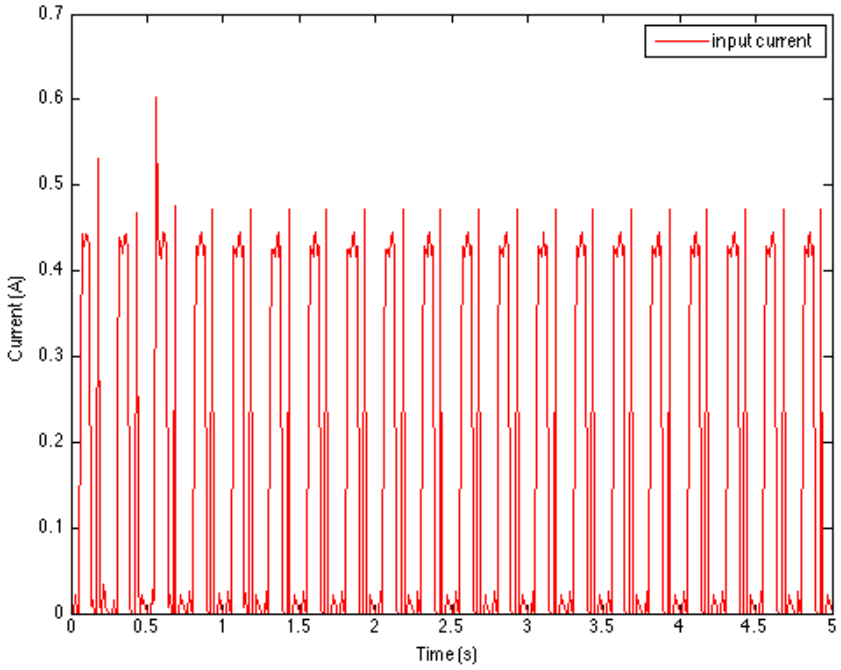

Figure 5.7: The required input current to produce the response as shown in Figure 5.5

5.2 Fuzzy Logic Skyhook Control

As the name suggests, rules for the Fuzzy Logic Skyhook Controller stem from Skyhook Control discussed in the previous section. The linguistic variables were chosen to be the suspension deflection velocity $\dot{s}$ and the absolute velocity of the sprung-mass $\dot{x}$ for the input, and the current as the control signal output. Six linguistic values were assigned to both of the two input variables: "Negative Small", "Negative Medium", "Negative Large", "Positive Small", "Positive Medium", and "Positive Large". Four linguistic values were assigned to the output variable, current: "Zero", "Small", "Medium", and "Large". 36 rules were generated using these variables and values. They were found by inspecting the control surface for the Skyhook algorithm represented in Figure 5.3. These rules are outlined in Table 5.1. The first two rules have been presented to represent 18 rules in total for the sake of convenience, taking

advantage of the fact that the input current should always be zero if the directions of $\dot{s}$ and $\dot{x}$ differ, regardless of their magnitudes. Also note that when $\dot{s}$ and $\dot{x}$ have the same direction, the current is proportional only to the magnitude of the absoulte seat velocity $\dot{x}$ as is also demonstrated in Figure 5.3.

Table 5.1: Base Rules for Fuzzy Skyhook Controller

No.	**Rule**
1-9	IF $\dot{s}$ is **Negative *** AND $\dot{x}$ is **Positive *** THEN *current* is **Zero**
10-18	IF $\dot{s}$ is **Positive *** AND $\dot{x}$ is **Negative *** THEN *current* is **Zero**
19	IF $\dot{s}$ is **Positive Small** AND $\dot{x}$ is **Positive Small** THEN *current* is **Small**
20	IF $\dot{s}$ is **Negative Small** AND $\dot{x}$ is **Negative Small** THEN *current* is **Small**
21	IF $\dot{s}$ is **Positive Medium** AND $\dot{x}$ is **Positive Medium** THEN *current* is **Medium**
22	IF $\dot{s}$ is **Negative Medium** AND $\dot{x}$ is **Negative Medium** THEN *current* is **Medium**
23	IF $\dot{s}$ is **Positive Large** AND $\dot{x}$ is **Positive Large** THEN *current* is **Large**
24	IF $\dot{s}$ is **Negative Large** AND $\dot{x}$ is **Negative Large** THEN *current* is **Large**
25	IF $\dot{s}$ is **Positive Small** AND $\dot{x}$ is **Positive Large** THEN *current* is **Large**
26	IF $\dot{s}$ is **Positive Medium** AND $\dot{x}$ is **Positive Large** THEN *current* is **Large**
27	IF $\dot{s}$ is **Negative Small** AND $\dot{x}$ is **Negative Large** THEN *current* is **Large**
28	IF $\dot{s}$ is **Negative Medium** AND $\dot{x}$ is **Negative Large** THEN *current* is **Large**
29	IF $\dot{s}$ is **Positive Small** AND $\dot{x}$ is **Positive Medium** THEN *current* is **Medium**
30	IF $\dot{s}$ is **Positive Large** AND $\dot{x}$ is **Positive Medium** THEN *current* is **Medium**
31	IF $\dot{s}$ is **Negative Small** AND $\dot{x}$ is **Negative Medium** THEN *current* is **Medium**
32	IF $\dot{s}$ is **Negative Large** AND $\dot{x}$ is **Negative Medium** THEN *current* is **Medium**
33	IF $\dot{s}$ is **Positive Medium** AND $\dot{x}$ is **Positive Small** THEN *current* is **Small**
34	IF $\dot{s}$ is **Positive Large** AND $\dot{x}$ is **Positive Small** THEN *current* is **Small**
35	IF $\dot{s}$ is **Negative Medium** AND $\dot{x}$ is **Negative Small** THEN *current* is **Small**
36	IF $\dot{s}$ is **Negative Large** AND $\dot{x}$ is **Negative Small** THEN *current* is **Small**

5.2.1 Triangular Membership Functions

The resulting input and output membership functions are shown in Figures 5.8, 5.9 and 5.10 respectively. Triangular membership functions were chosen for the two input variables, $\dot{s}$ and $\dot{x}$, while singular membership functions were selected for the output variable, current. Based on initial simulations with constant minimum and maximum damping, and confirmed by the fact that the frequency ratio was greater than $\sqrt{2}$, the output membership function was constrained to vary from 0.0 to 0.2 A.

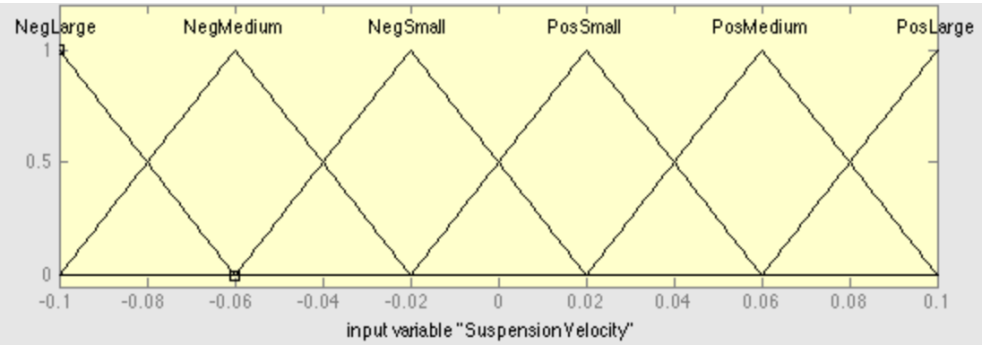

Figure 5.8: Triangular-shaped input membership function for the relative velocity.

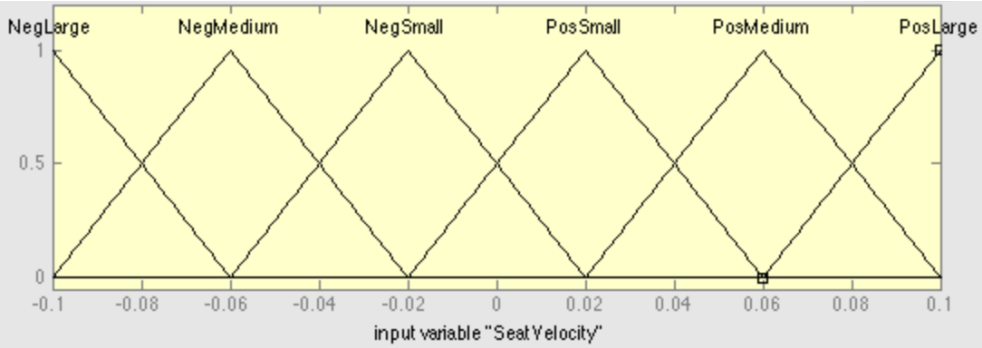

Figure 5.9: Triangular-shaped input membership function for the seat velocity.

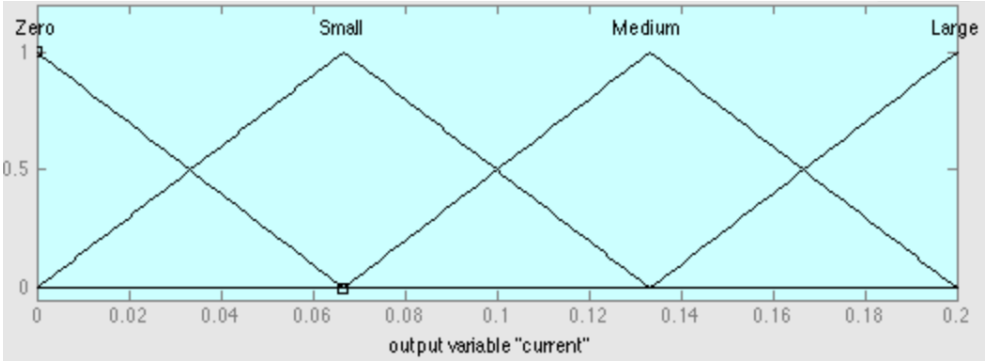

Figure 5.10: Singular output membership function for the control signal.

The resulting control surface is shown in Figure 5.11 for inputs of seat and relative deflection velocities and the current control signal output.

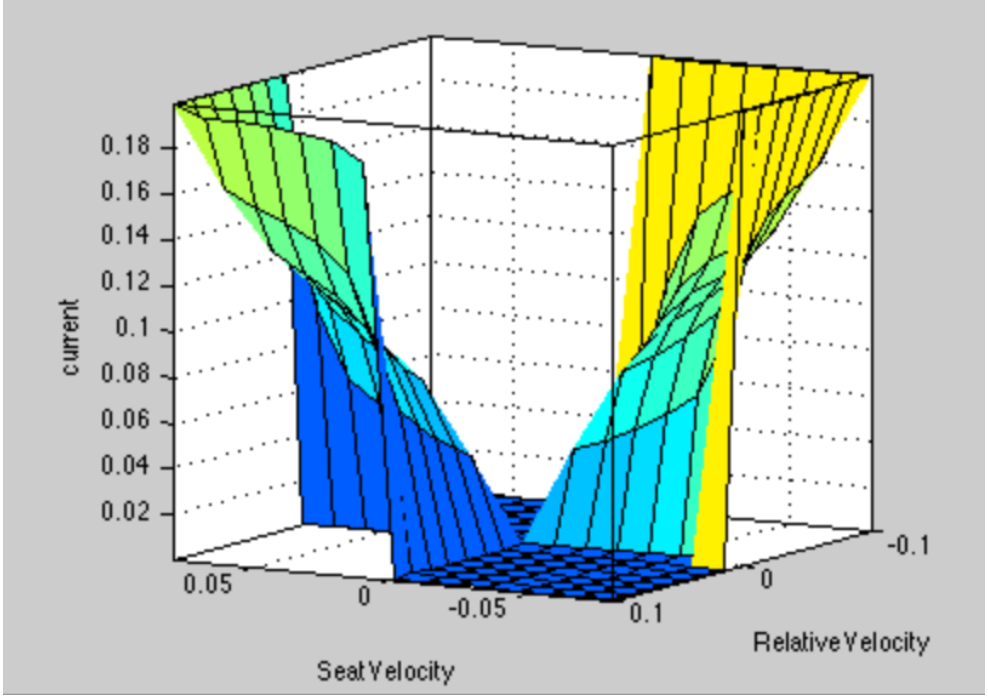

Figure 5.11: Input-output graph for the 5-rule fuzzy controller

This control surface is visual representation of the base rules shown in Table 5.1, providing the desired current for the measured velocities. It is convenient in that current is yielded immediately if the relative suspension velocity and absolute seat velocity are known. Therefore the control signal can be sent directly to the plant and an inverse current model is not required.

Simulation results for acceleration and input current with the same half-seat model used in the previous section are shown in Figures 5.12 and 5.13.

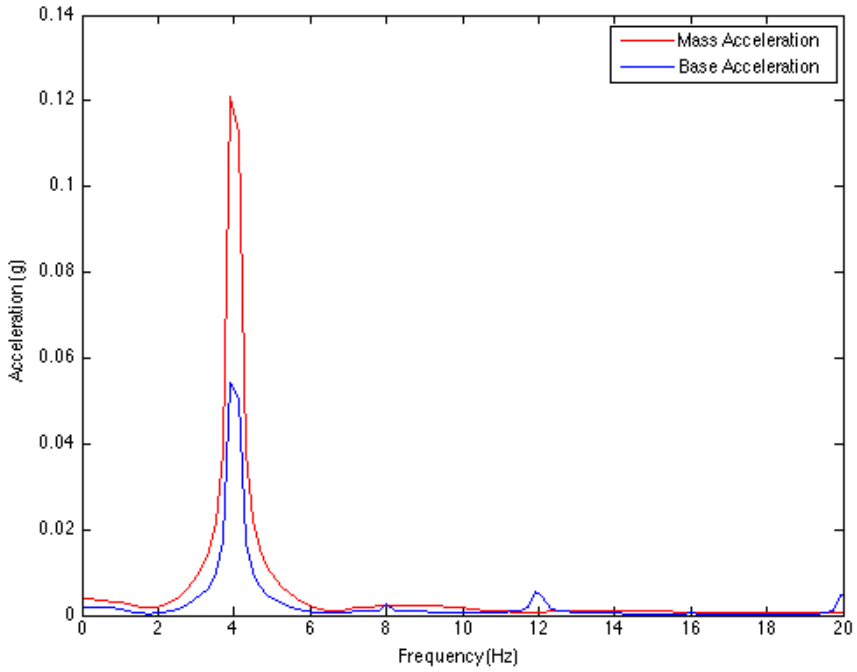

Figure 5.12: Acceleration attenuation of the sprung mass governed by an FLC.

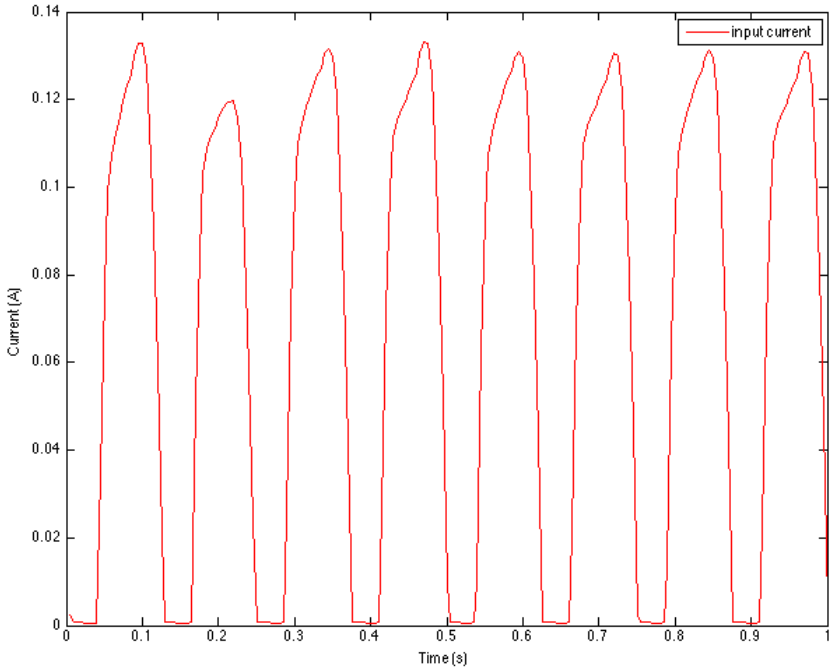

Figure 5.13: The required input current to produce the response as shown in Figure 5.12

5.2.2 Gaussian Membership Functions

Gaussian membership functions were also tested. To further differentiate the tests from those involving triangular membership functions, the upper limit on the current output was removed to allow for outputs ranging from $0.0 - 1.0\ A$. Both input membership functions for the relative and absolute membership functions differed in shape from the triangular input membership functions but maintained the same maximums.

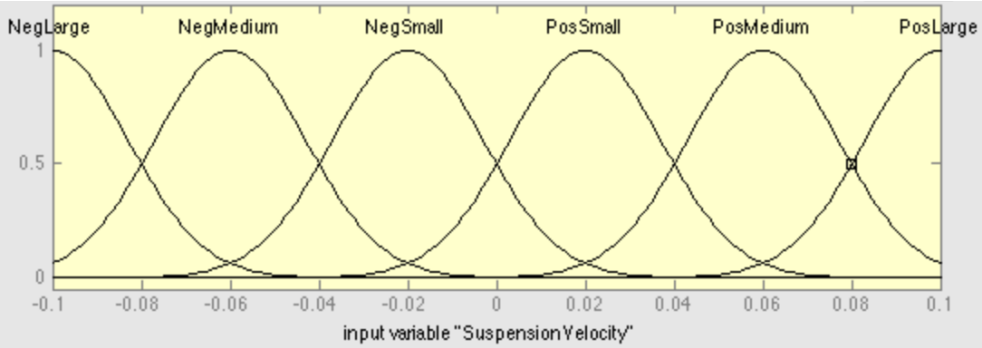

Figure 5.14: Gaussian-shaped input membership function for the relative velocity $\dot{s}$.

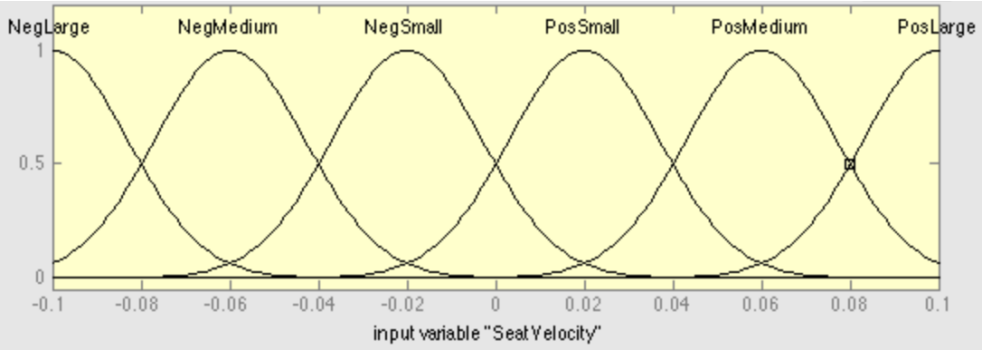

Figure 5.15: Gaussian-shaped input membership function for the seat velocity $\dot{x}$.

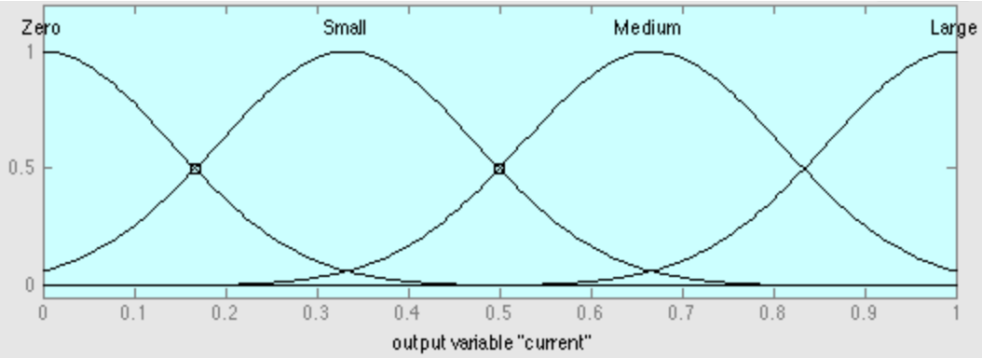

Figure 5.16: Singular output membership function for the control signal.

The resulting control surface is shown in Figure 5.17, providing a visual of the desired control current for inputs of seat and relative deflection velocities. Like the previous FLC, current is yielded directly, negating the need for a reverse force-to-current model. Comparing the control surface to that of the previous FLC, transitions are much smoother due to the continuous Gaussian output membership function, and the full 0.0 to 1.0 A range of currents is available. The triangular FLC used a singular output membership function constrained between 0.0 and 0.2 A. Because both FLC's are predicated upon Skyhook control, these control surfaces exhibit similar characteristics to the damping coefficient surface shown in Figure 5.2. That is, current (and therefore damping coefficient) is maximized when the relative suspension and absolute seat velocities are in the same direction and minimized when they are in opposing directions.

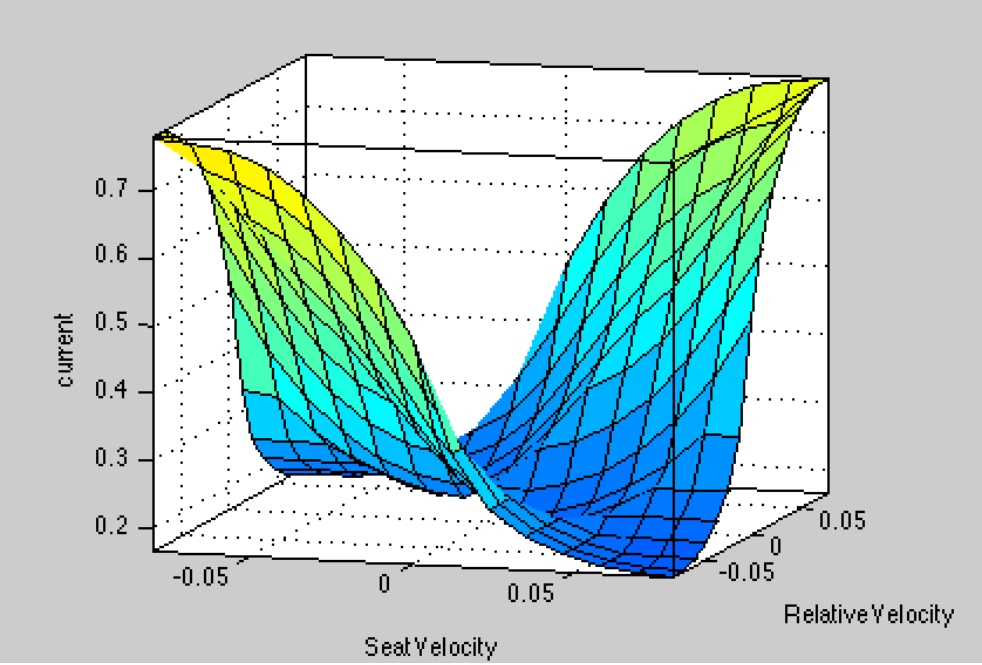

Figure 5.17: Input-output surface plot of the Fuzzy Gaussian rule system.

Simulation results for acceleration and force are shown in Figures 5.18 and 5.19.

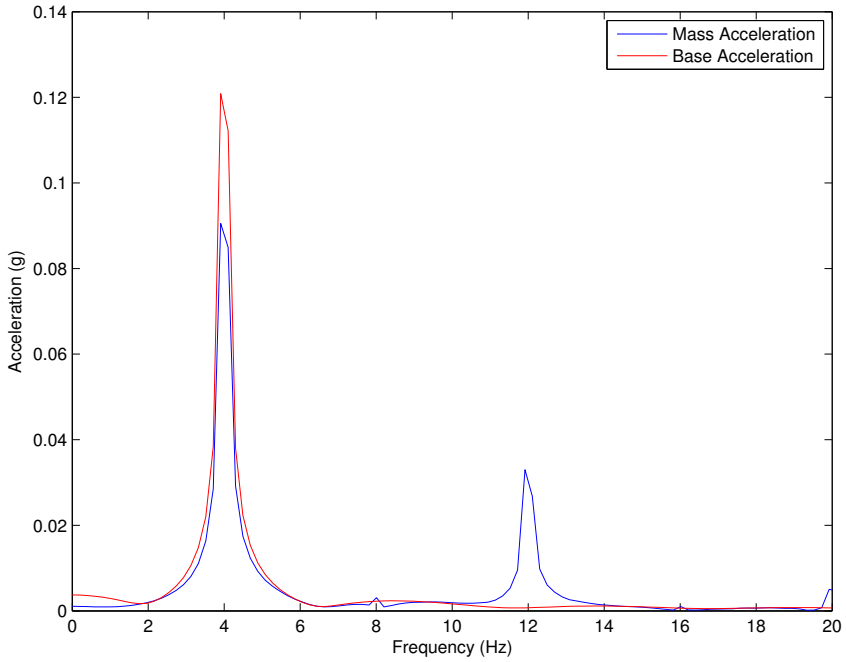

Figure 5.18: The acceleration of the sprung mass when governed by Gaussian Fuzzy control.

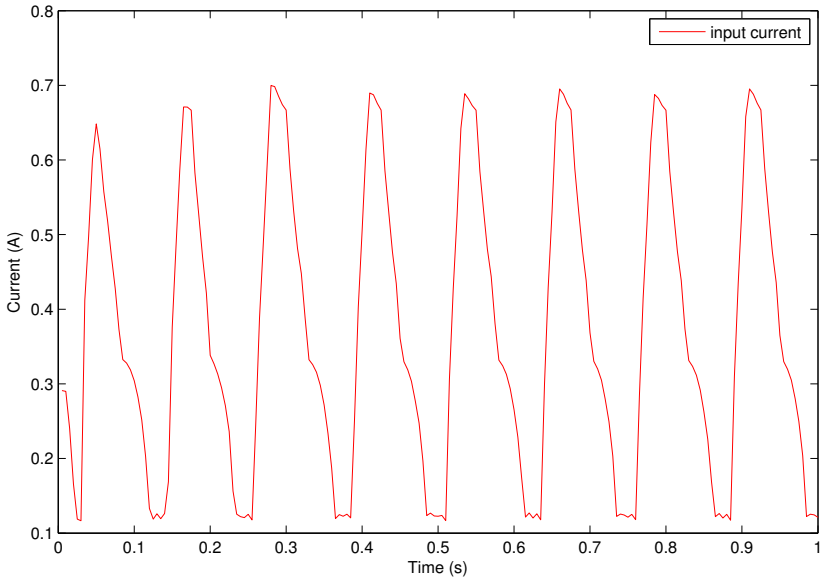

Figure 5.19: The required input current to produce the response as shown in Figure 5.18

5.3 Optimal Control Strategies for Semi-Active Systems

Replacing the MR damper with an actuator, the following dynamic equation results for the half-seat suspension model:

$$m\ddot{y} + k(y - y_g) = f(t) \tag{5.2}$$

where y is the displacement of the mass,y_g is the displacement of the ground excitation and f is the force provided by the actuator.

Using the state variables x_1 and x_2 to represent the displacement and velocity respectively of the sprung mass, the following state-space representation results:

$$\begin{bmatrix} \dot{x_1} \\ \dot{x_2} \end{bmatrix} = \begin{bmatrix} 0 & 1 \\ -\frac{k}{m} & 0 \end{bmatrix} \begin{bmatrix} x_1 \\ x_2 \end{bmatrix} + \begin{bmatrix} 0 & 0 \\ \frac{k}{m} & \frac{1}{m} \end{bmatrix} \begin{bmatrix} y_g \\ f \end{bmatrix}$$

It's important to note that in the state-space model as written above, the vector $\vec{u}$ technically comprises of two inputs - the base excitation and actuator force - however it is only the force component that can be controlled and fed back into the system. To distinguish between the disturbance and control vectors, the **B** matrix can be rearranged as follows:

$$\begin{bmatrix} \dot{x_1} \\ \dot{x_2} \end{bmatrix} = \begin{bmatrix} 0 & 1 \\ -\frac{k}{m} & 0 \end{bmatrix} \begin{bmatrix} x_1 \\ x_2 \end{bmatrix} + \begin{bmatrix} 0 \\ \frac{k}{m} \end{bmatrix} y_g + \begin{bmatrix} 0 \\ \frac{1}{m} \end{bmatrix} f$$

LQR techniques can now be employed to provide an optimal output force for a given base excitation. The optimal force is shown in Figure 5.21 and provides displacement results as shown in Figure 5.20. Here Q and R were chosen to be as follows:

$$Q = \begin{bmatrix} 100 & 0 \\ 0 & 1 \end{bmatrix}$$

$$R = 0.1$$

These values were chosen to put emphasis on regulating the displacement of the sprung mass as opposed to the velocity, as well as prevent the actuator force from being so large that it would be unfeasible to match to a damping force.

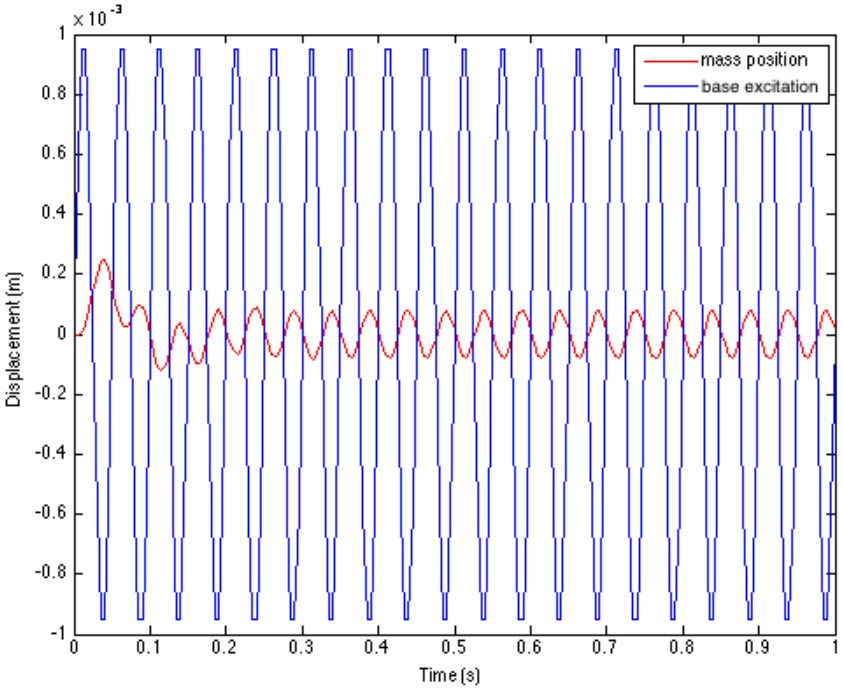

Figure 5.20: Displacement of the sprung mass governed by full LQR control.

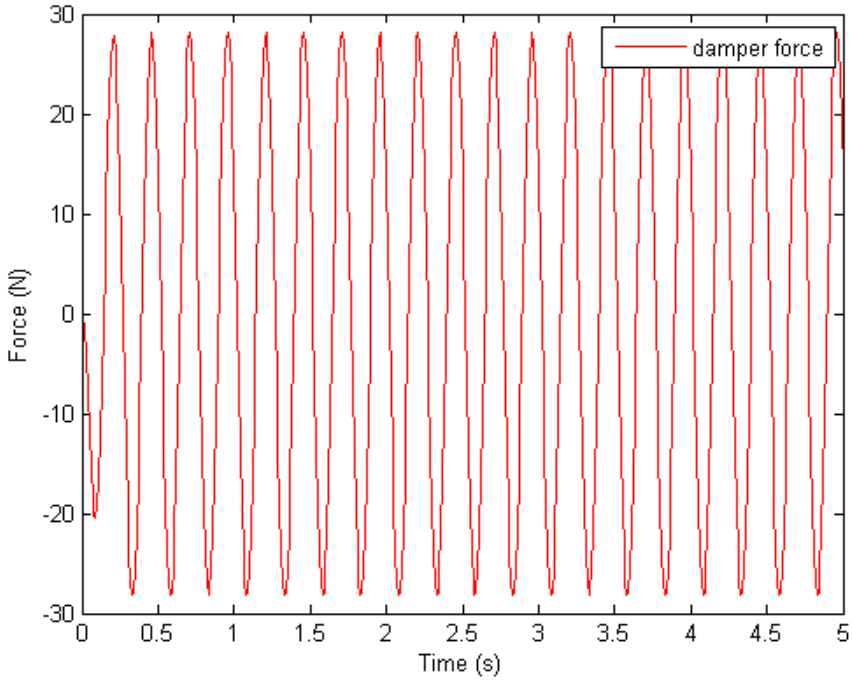

Figure 5.21: Force provided by a theoretical actuator governed by full LQR control.

5.3.1 Clipped Optimal Control

The command signal to the MR damper should always attempt to generate the corresponding desired optimal control force f. If it is able to do so, the current supplied to the damper should remain at the present level. However if the magnitude of the force produced by the damper is smaller than the magnitude of the desired optimal force and the two forces have the same sign, the current applied is increased to the maximum level so as to increase the force produced by the damper to match the desired control force. Otherwise the input current is set to zero. The control policy is shown schematically in Figure 5.22.

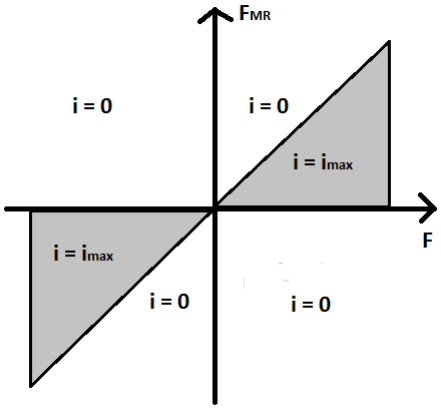

Figure 5.22: A schematic of the control policy that governs clipped optimal control [39].

The implementation of clipped optimal control is represented by a flowchart in Figure 5.23, with the corresponding code available in the appendix.

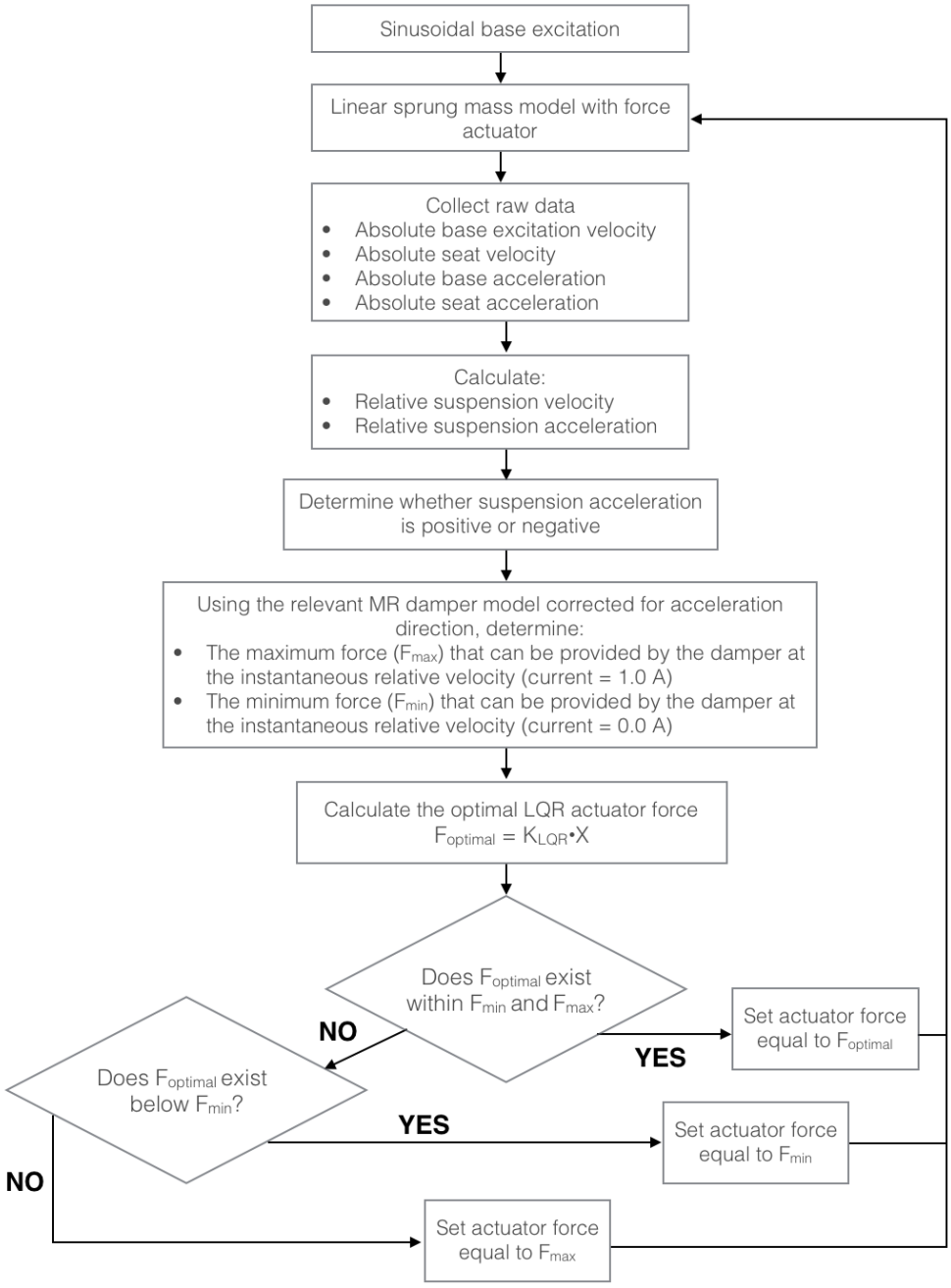

Figure 5.23: A flowchart for the implementation of clipped optimal control.

The displacement and damping force results are shown in Figures 5.24 and 5.25 respectively, with the matrices Q and R being the same as what was used in the full LQR policy.

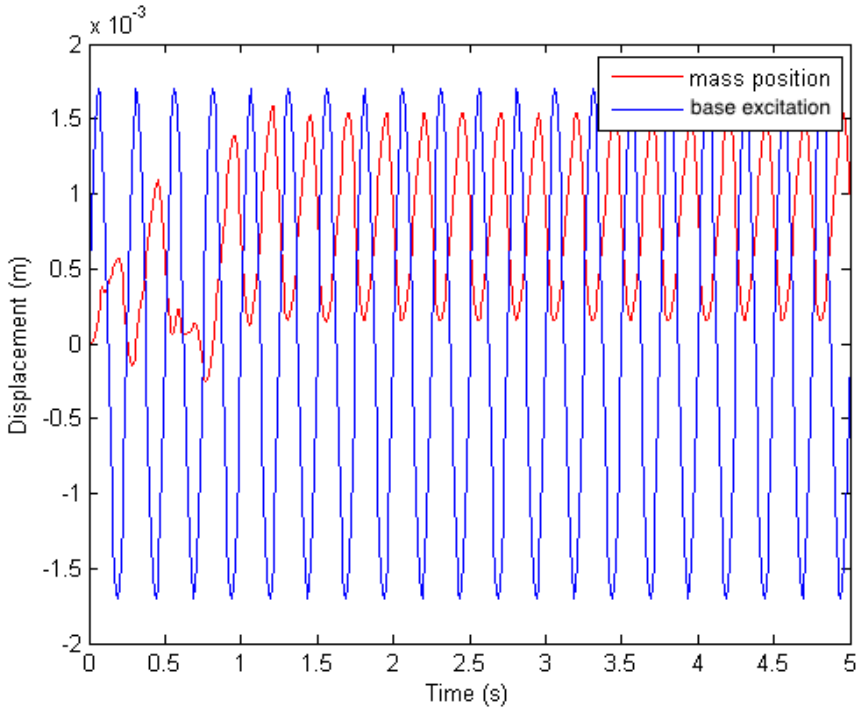

Figure 5.24: Displacement of the half-seat model governed by clipped LQR control.

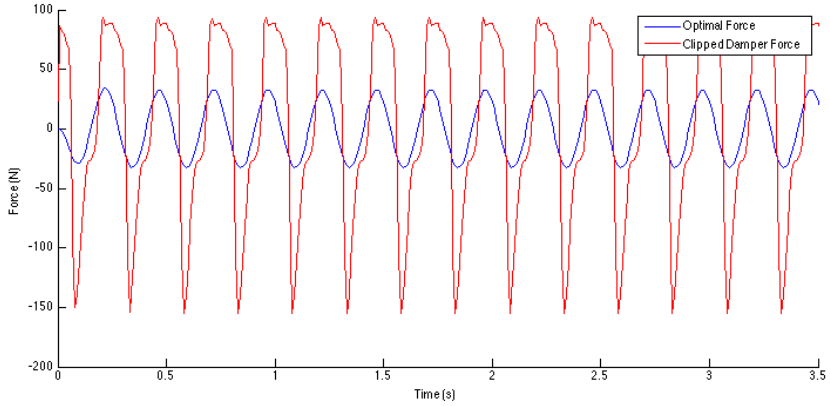

Figure 5.25: Force provided by the MR damper model governed by clipped LQR control (red)compared to that given by Full LQR control (blue).

Using the reverse current model developed in the previous chapter, the input current required for this response is shown in Figure 5.26.

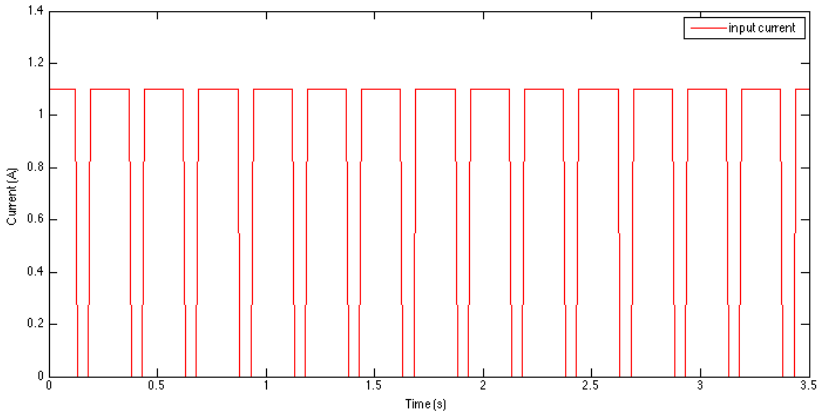

Figure 5.26: The required input current to produce the response as shown in Figure 5.24

6 Discussion

6.1 Response to Uniform Harmonic Base Excitation

The displacement and force results for each controller are summarized numerically in Table 6.1.

Table 6.1: Force and Displacement results summarized for each control scenario.

Control	Amplitude of Mass Disp. (mm)	Min/Max Force (N)	Accel. at 4 Hz (g)
Constant Minimum Damping	0.125	-80/20	0.045
Constant Maximum Damping	0.800	-590/430	0.145
Full LQR Control	0.01	-12/12	0.010
Clipped LQR Control	0.80	-78/20	0.055
Skyhook Control	1.4	-91/130	0.079
Triangular Fuzzy Logic	1.0	-59/101	0.050
Gaussian Fuzzy Logic	1.8	-150/200	0.090

The acceleration data for constant minimum and maximum damping was compared to determine which was more suitable for a baseline that controller results could be measured to. Figure 6.1 compares these accelerations.

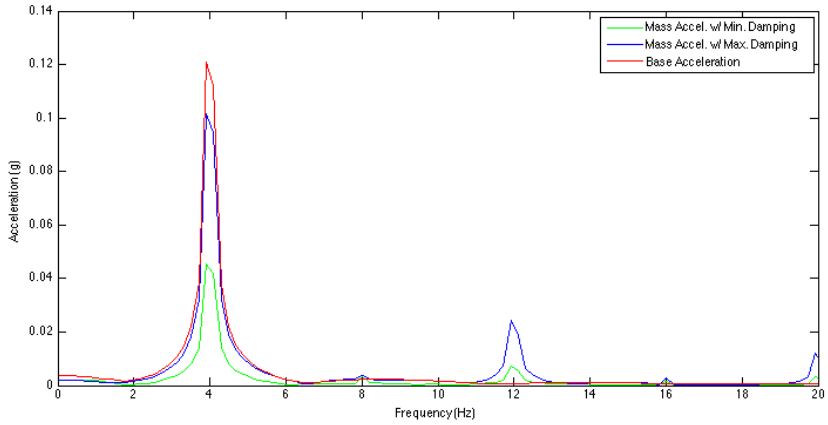

Figure 6.1: A comparison of accelerations given by constant minimum and maximum damping

Clearly minimum damping provides superior vibration attenuation, reducing acceleration at the first harmonic by a factor of 3. Maximum damping performs poorly in comparison. The stiffness of the system in this scenario contributes to this, as shown by the displacement data shown in Figure 6.2.

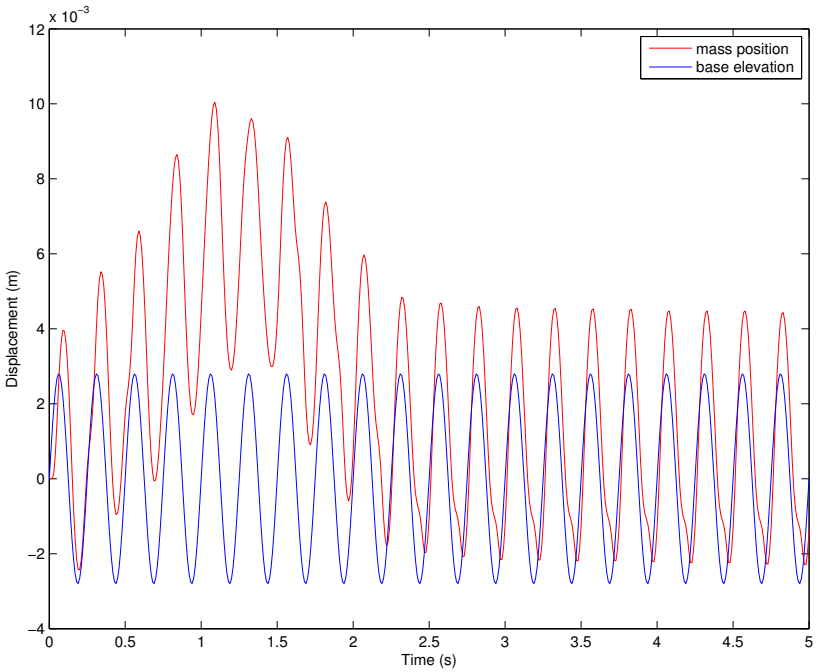

Figure 6.2: Displacement data with maximum damping. The sprung mass follows the base excitation closely as is expected with a stiff system.

Figure 6.3 compares acceleration data using the various controllers to the baseline provided by constant minimum damping. The perspective is centred around the the peaks of the frequency plots for ease of comparison.

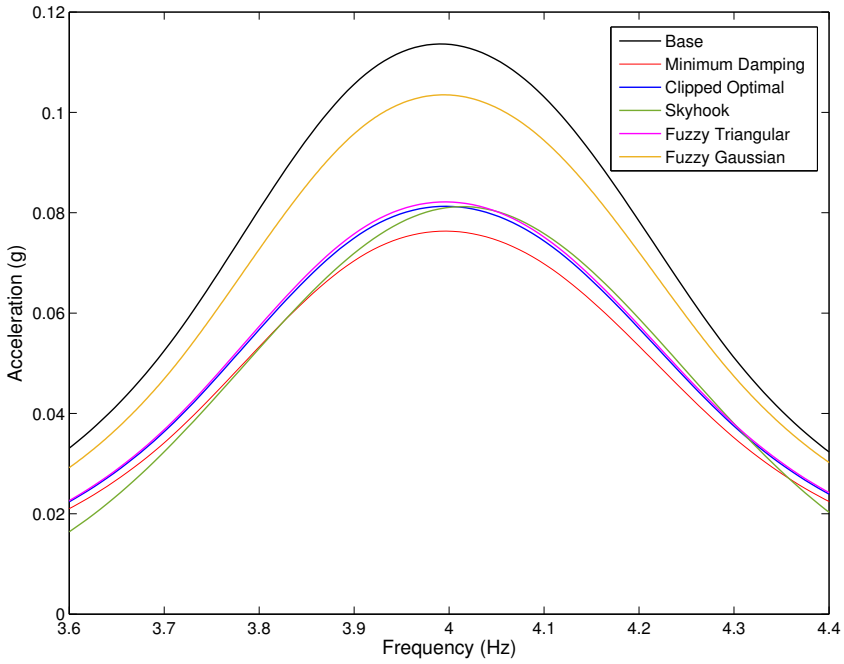

Figure 6.3: A comparison of accelerations given by constant minimum damping and the various controllers

It can be seen that minimum constant damping, Triangular Fuzzy control, Skyhook control, and Clipped Optimal control respectively provide the best vibration isolation results in regards to acceleration, mitigating the harmful forces transmitted to the sprung mass. Although the results for these three scenarios are relatively similar, displacement results shown in Figure 6.4 reveal more differences.

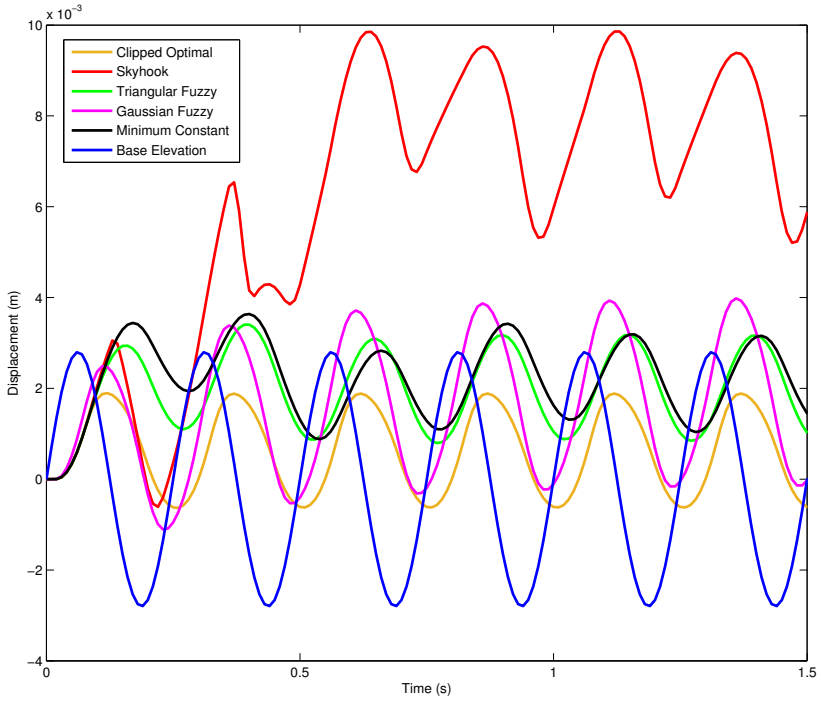

Figure 6.4: A comparison of sprung mass displacements given by constant minimum damping and the various controllers

Constant minimum damping provides slightly better isolation than clipped optimal control, however, because optimal control strives to minimize displacement, it provides more stable results when comparing displacement data.

The controllers can be split into two broad classes: continuous controllers, encompassing Skyhook and Clipped Optimal control, and Fuzzy Logic control. A comparison of input currents within the two classes are shown in Figures 6.5 and 6.6.

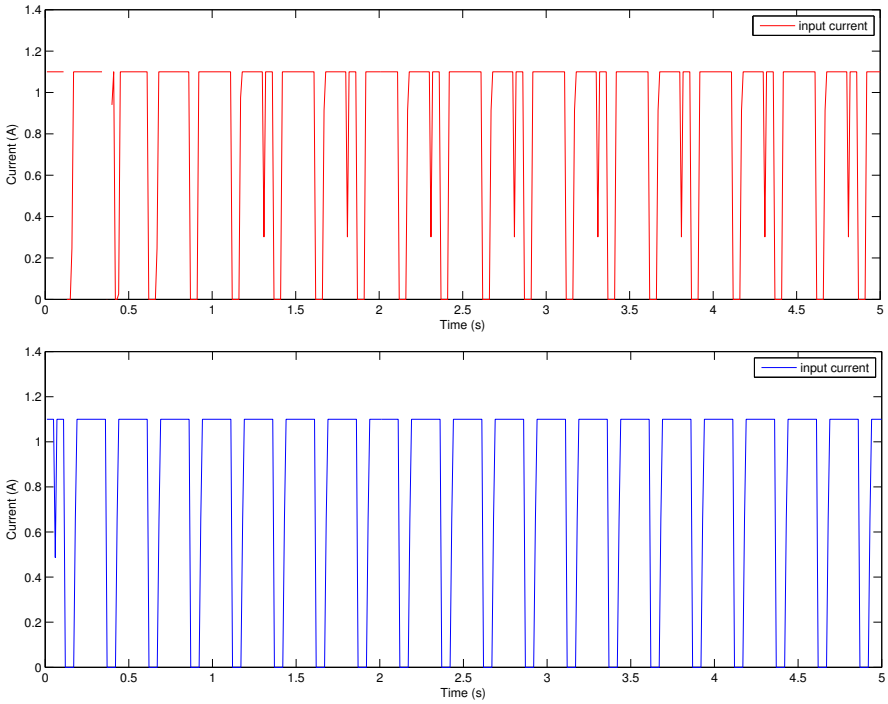

Figure 6.5: A comparison of input currents required by Skyhook (red) and Clipped Optimal (blue) control

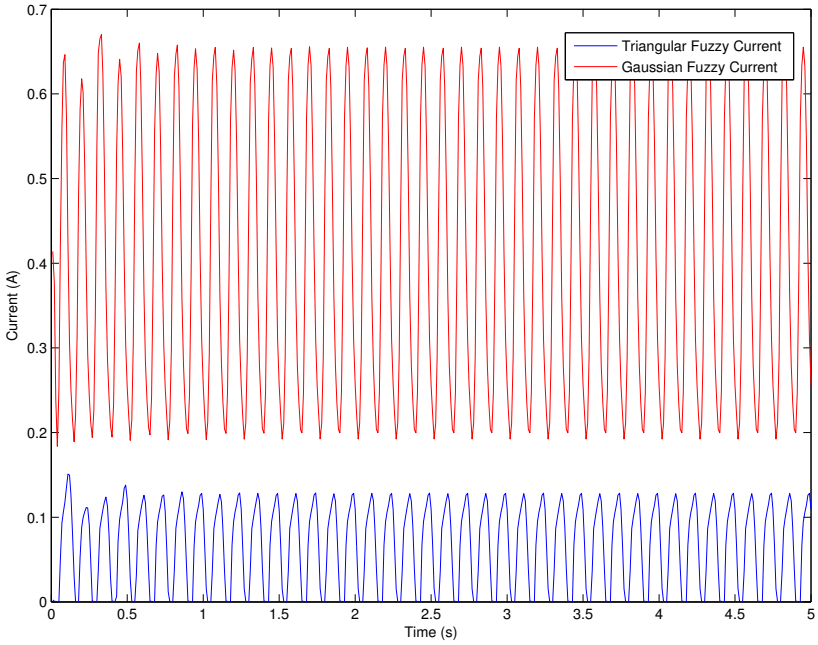

Figure 6.6: A comparison of input currents required by Triangular and Gaussian Fuzzy control

A current ceiling restriction was added to the Triangualr Fuzzy controller after it was noted that lower input currents performed better when subject to the constant base excitation used in the simulation. This restriction wasn't used in the Gaussian Fuzzy controller to magnify its effects, hence the differences noted in Figure 6.6.

6.2 Response to a Sudden Jerk Disturbance

A sudden jerk was added to the base excitation in the form of a step function with an amplitude of 50 mm to test the benefit of adaptability with semi-active systems compared to fixed vibration control. Sudden non-uniform disturbances occur in flight when turbulence is encountered and on impact with the ground. A hard landing can occur after mechanical or engine damage or failure when the rotors are still intact and free to turn and even though

autorotation, where airflow over the rotors keeps them turning, provides some lift and can allow limited pilot control during descent, potentially dangerous force is still supplied to the pilot. The displacement results of this simulation are shown in Figure 6.7.

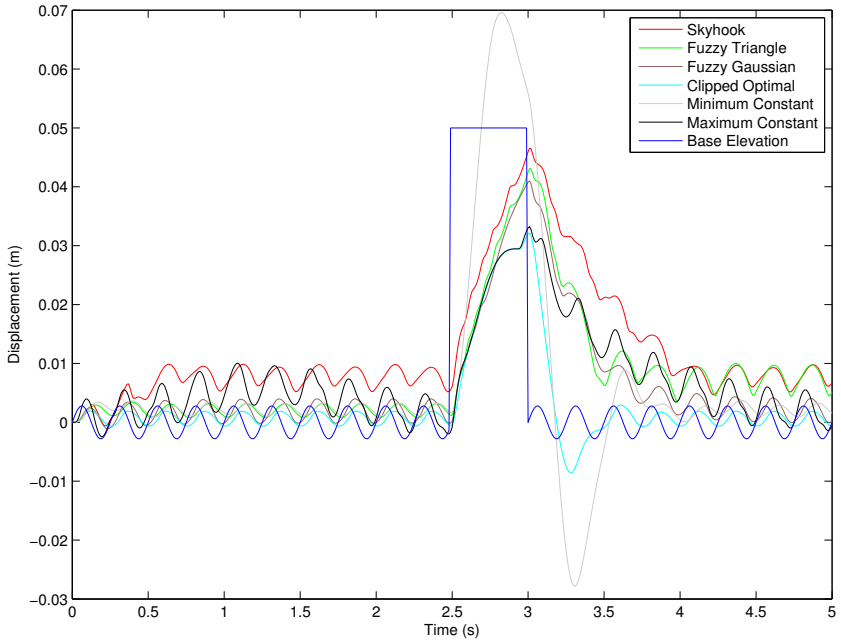

Figure 6.7: A comparison of displacements given by respective controllers (defined in legend) exposed to a sudden jerk excitation (blue).

It can be seen that minimum fixed damping (shown in grey in Figure 6.7) provides the worst attenuation performance when subjected to a jerk, as opposed to its relatively effective performance with a uniform excitation. Fixed maximum damping is particularly effective at mitigating the sudden disturbance but is not as effective attenuating constant harmonic vibration. These results provide reasonable grounds for semi-active control to provide effective results when subject to varying disturbances. Within a helicopter, although the rotor rotation speed provides the dominant vibration frequency, ground-effect and rotor-wash turbulence can contribute to sudden excitation that require mitigation.

Clipped optimal control appears to combine the benefits of maximum and minimum damping most effectively, and is especially evident when reviewing the input current results shown in Figure 6.8. The Gaussian Fuzzy controller performs well in this instance compared to the Triangular Fuzzy version due to the lack of a current restriction, also evident in Figure 6.8.

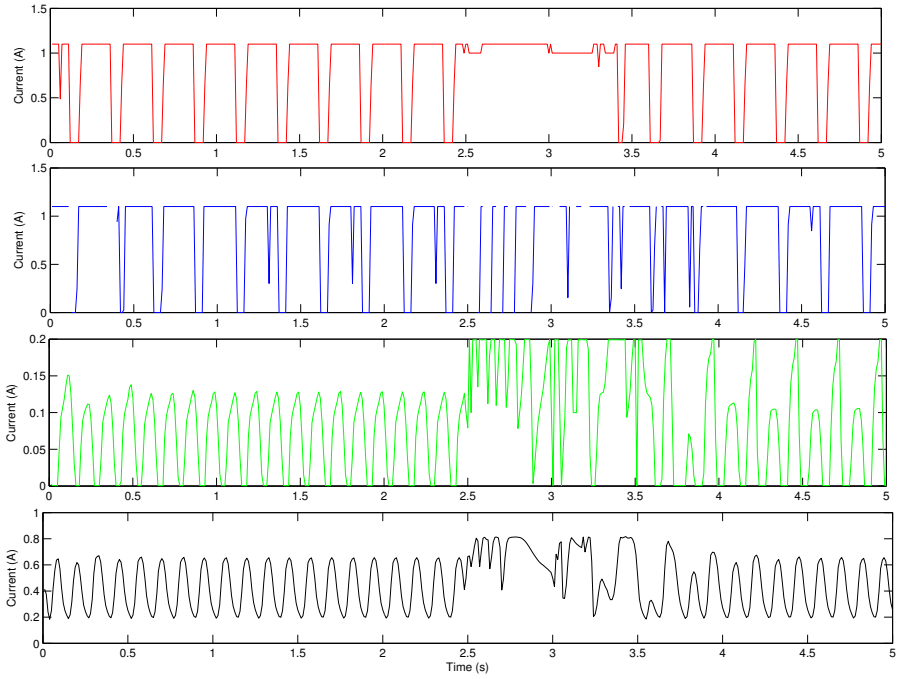

Figure 6.8: A comparison of current inputs demanded by controllers exposed to a sudden jerk excitation. Clipped optimal, Skyhook, Fuzzy triangular and Fuzzy Gaussian controls are shown in red, blue, green and black respectively.

6.3 Validation

6.3.1 ISO 2631 Standard for Vibration and Human Health

As seen in Figure 6.3, Clipped-Optimal control attenuates vibration to 0.08 g. Referring to the ISO 2631 standard for vibration and human health shown in Figure 2.1, an aircrew member subjected to accelerations of 0.08 g at frequencies of 4 Hz could operate under such conditions for a maximum of 3.5

hours before fatigue and resulting damage becomes a factor. Currently, due to the minimal isolation provided by seat cushions alone, the Royal Canadian Air Force estimates that aircrew members are exposed to 0.1 g accelerations, reducing potential missions to just 1.5 hours in order to remain compliant within ISO 2631. The use of semi-active control could therefore potentially double the length of flights at comfortable vibration levels for aircrew.

6.3.2 Comparison to Other Research

As discussed in Chapter 2, Hiemenz [11] showed that the use of MR dampers reduced 4/rev vibrations transmitted to the crew in the vertical axis by 76%, excluding cushions. Simulating a base excitation of 0.12 g, 0.08 g vibration at the seat constitutes a 34% reduction. The dampers used in Hiemenz's research were specifically designed to operate at low frequencies centered upon 4 Hz by minimizing friction. This may constitute the difference seen in results.

7 Conclusions and Recommendations

7.1 Conclusions

Many different solutions are available to the harmful vibration problem that exists within rotary-wing cockpits. Semi-active control using magnetorheological dampers offers unique advantages that are important when operating within the strict limitations that exist in aviation. A variety of control strategies can be implemented, but simulating results from these requires an accurate model of the MR damper being used. Hysterisis and non-linearities provide complexity to these models, however fitting experimental data to known hysterisis models provides an adequate estimate. This thesis examined several control schemes, namely the Skyhook, Clipped Optimal, Fuzzy Triangular and Fuzzy Gaussian controllers. Relying on absolute and relative velocities, and acceleration of the sprung mass, all controllers successfully mitigated vibration within the half-seat model to varying degrees, with Clipped Optimal control providing the best performance in both constant 4 Hz harmonic and sudden jerk excitation scenarios, which have demonstrably proved to be most harmful to rotary-wing aircrew. Ultimately, MR dampers with a proper semi-active control policy were found to potentially increase mission times to 3.5 hours, compared to just 1.5 hours, while still remaining compliant with ISO 2631.

7.2 Recommendations

An obvious extension to the research presented in this thesis is experimental implementation of the system that was simulated in Chapter 5. An LDS V-411 shaker, similar to the one shown in Figure 7.1, was intended to be used in conjunction with a testing rig.

Figure 7.1: An LDS V-411 shaker that was used to attempt an experimental implementation

This rig was to consist of a base platform which would be attached to the shaker, and a floating upper platform which would hold the sprung mass. Between the platforms would be a spring to provide stiffness and an MR damper suspended by clevis joints. The overall rig is shown in Figure 7.2.

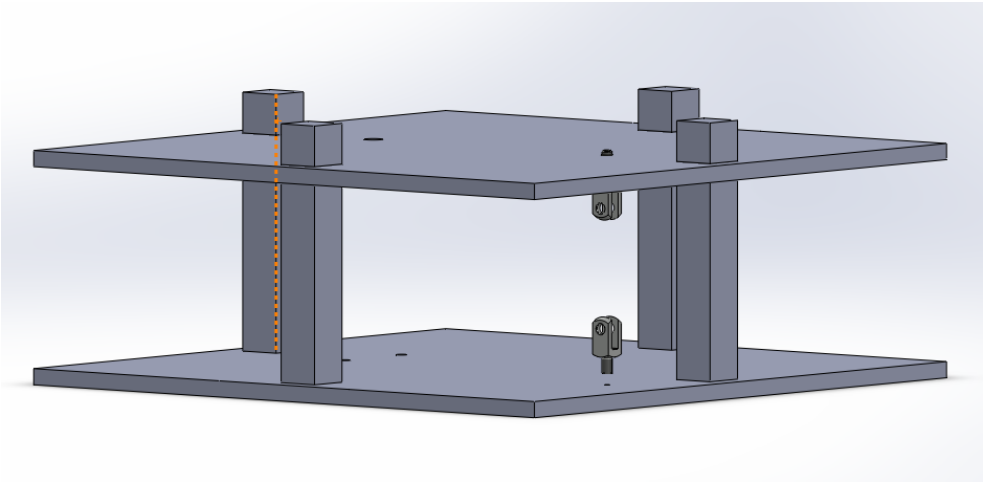

Figure 7.2: The proposed test rig for vibration testing

This particular magnetic shaker is capable of supplying a peak force of 250 N. However due to the size of the MR damper and the force it's capable of producing, a mass of at least 80 kg and a stiffness of 13000 $\frac{N}{m}$ is required to cause sufficient deflection at the excitation frequency in question. These requirements are well outside the capabilities of a magnetic shaker and halted testing. Despite this, a data collection interface was created, using accelerometers attached to the base and sprung mass to generate relative and absolute parameters. With the use of a more powerful hydraulic shaker, a simple experimental implementation can take place and be compared to simulated results.

Bibliography

[1] Steven J Gaydos. Low back pain : Considerations for rotary-wing aircrew. *United States Army Aeromedical Research Laboratory*, 2013.

[2] International Organization of Standards. Iso-2631/1 mechanical vibration and shock - evaluation of human exposure to whole-body vibration. part 1: General requirements. *International Standard*, 1997.

[3] PM Bongers, CTJ Hulshof, L Dukstra, and HC Boshuizen. Back pain and exposure to whole body vibration in helicopter pilots. *Ergonomics*, 33:1007–1026, 1990.

[4] RS Bridger, MR Groom, H Jones, RJ Pethybridge, and N Pullinger. Task and postural factors are related to back pain in helicopter pilots. *Aviation, Space and Environmental Medicine*, 73:805 – 811, 2002.

[5] LK Cunningham, S Docherty, and AW Tyler. Prevalence of low back pain (lbp) in rotary wing aviation pilots. *Aviation, Space and Environmental Medicine*, 81:774 – 778, 2010.

[6] P Froom, R Hanegbi, J Ribak, and M Gross. Low back pain in the ah-1 cobra helicopter. *Aviation, Space and Environmental Medicine*, 58:315–318, 1987.

[7] OB Hansen and AS Wagstaff. Low back pain in norwegian helicopter aircrew. *Aviation, Space and Environmental Medicine*, 72:161–164, 2001.

[8] SC Sheard, RJ Pethybridge, JM Wright, and GHG McMillan. Back pain in aircrew - an initial survey. *Aviation, Space and Environmental Medicine*, 67:474–477, 1996.

[9] MK Thomae, JE Porteous, JR Brock, GD Allen, and RF Heller. Back pain in australian military helicopter pilots: a preliminary study. *Aviation, Space and Environmental Medicine*, 69:468–473, 1998.

[10] Jeffrey R. Davis MD MS, Robert Johnson MD MPH MBA, and Jan MD MPH Stepanek. *Fundamentals of Aerospace Medicine*. Lippincott Williams and Wilkins, 4 edition, april 2008.

[11] Gregory J. Hiemenz. S-A MR Seat Suspensions for Enhanced Crashworthiness and Vibration Isolation of Rotocraft Seats.

[12] B.F. Jr. Spencer, S.J. Dyke, M.K. Sain, and J.D. Carlson. Phenomenological model of a magnetorheological damper. *Journal of Engineering Mechanics*, 123:230–238, 1997.

[13] S. S. Rao. *Mechanical Vibrations*. Addison-Wesley, Reading, MA, 19.

[14] S.J. Mcmanus, K.a. St. Clair, P.É. Boileau, J. Boutin, and S. Rakheja. Evaluation of Vibration and Shock Attenuation Performance of a Suspension Seat With a Semi-Active Magnetorheological Fluid Damper. *Journal of Sound and Vibration*, 253(1):313–327, May 2002.

[15] Viresh Wickramasinghe, Yong Chen, and David Zimcik. Development of an Active Suspension System for Adaptive Control of Helicopter Seats. *Active Suspension Technologies for Military Vehicles and Platforms*, pages 1–13, 2012.

[16] Geoffrey Geldhof. Semi-Active Vibration Dynamics Control of Multi-Cart Systems Using a Magnetorheological Damper. 2013.

[17] R Stanway, J.L Sproston, and N.G Stevens. Non-linear modelling of an electro- rheological vibration damper. *Journal of Electrostatics*, 1987.

[18] Kyoung Kwan Ahn, Dinh Quang Truong, and Muhammad Aminul Islam. Modeling of a magneto-rheological (MR) fluid damper using a self tuning fuzzy mechanism. *Journal of Mechanical Science and Technology*, 23(5):1485–1499, may 2009.

[19] Weng Wai Chooi and S. Olutunde Oyadiji. Mathematical Modeling, Analysis, and Design of Magnetorheological (MR) Dampers. *Journal of Vibration and Acoustics*, 131(6):061002, 2009.

[20] D.R. Gamota and F.E. Filisko. Dynamic mechanical studies of electrorheologicalmaterials: Moderate frequency. *Journal of Rheology*, 35(1):399–425, 1991.

[21] R. Bouc. Forced vibration of mechanical systems with hysterisis. *Conference on Nonlinear Oscillation, Prague*, 1967.

[22] Y. K. Wen. Method for random vibration of hysterisis system. *Journal of the Engineering Mechanics Division*, 102(2):249–263, 1976.

[23] Weng Wai Chooi and S. Olutunde Oyadiji. Experimental Testing and Validation of a Magnetorheological (MR) Damper Model. *Journal of Vibration and Acoustics*, 131(6):061003, 2009.

[24] Bogdan Sapinski and Filuś Jacek. Analysis of Parametric Models of MR Linear Dampers. *Theoretical, Journal O F Mechanics, Applied*, pages 215–240, 2003.

[25] D Q Truong and K K Ahn. MR Fluid Damper and Its Application to Force Sensorless Damping Control System. 2012.

[26] Torsten Butz. Modelling and simulation of rheological fluid devices. *SFB-438-9911, Sonderforschungsbereich*, (438):99–110, may 1999.

[27] Shuqi Guo and Shaohua Li. Semi-active Vehicle Suspension Systems with Magnetorheological Dampers. (17):403–406, 2006.

[28] I. Maciejewski. Control system design of active seat suspensions. *Journal of Sound and Vibration*, 331(6):1291–1309, mar 2012.

[29] S.R. Hong, S.B. Choi, Y.T. Choi, and N.M. Wereley. A hydro-mechanical model for hysteretic damping force prediction of er damper: experimental verification. *Journal of Sound and Vibration*, 285(1):1180–1188, january 2005.

[30] Rene Jimenez and Luis Alvarez-Icaza. Lugre friction model for a magnetorheological damper. *Structural Control and Health Monitoring*, 12(1):91–116, october 2004.

[31] Fernando D Goncalves and Daniel Inman. Dynamic Analysis of Semi-Active Control Techniques for Vehicle Applications by Dynamic Analysis of Semi-Active Control Techniques for Vehicle Applications. August 2001.

[32] Y. Shen. Semi-active Vibration Control Schemes for Suspension Systems Using Magnetorheological Dampers. *Journal of Vibration and Control*, 12(1):3–24, January 2006.

[33] C Spelta, O Sename, S M Savaresi, and L Dugard. Survey on some automotive semi-active suspension control methods : a comparative study on a single-corner model. 2011.

[34] R.S. Prabakar, C. Sujatha, and S. Narayanan. Response of a quarter car model with optimal magnetorheological damper parameters. *Journal of Sound and Vibration*, 332(9):2191–2206, April 2013.

[35] Xubin Song. Cost-Effective Skyhook Control for Semiactive Vehicle Suspension Applications. *The Open Mechanical Engineering Journal*, 3(1):17–25, February 2009.

[36] Mehdi Ahmadian, Xubin Song, and Steve C. Southward. No-Jerk Skyhook Control Methods for Semiactive Suspensions. *Journal of Vibration and Acoustics*, 126(4):580, 2004.

[37] A. Kauffman. *Introduction to the theory of fuzzy sets*. Academic Press, New York, 1975.

[38] R. Caponetto, O. Diamante, G. Fargione, A. Risitano, and D. Tringali. A soft computing approach to fuzzy sky-hook control of semiactive suspension. *IEEE Transactions on Control Systems Technology*, 11(6):786–798, November 2003.

[39] S.J. Dyke, B.F. Spencer Jr., M.K. Sain, and J.D. Carlson. An Experimental Study of MR Dampers for Seismic Protection. *Smart Materials and Structures: Special Issue on Large Civil Structures*, 1(1):51–58, May 2001.

[40] P. Bickel and K. Doksum. *Mathematical Statistics: Basic Ideas and Selected Topics*. Holden-Day, San Francisco, 1977.

[41] Aerospace Engineering Test Establishment. Ch124 technical guide - crew seats, 2006.

Appendices

```
%PARAMETERIZED BOUC-WEN ALGORITHM TO BE USED IN CONJUCTION WITH
%THE LEAST SQUARES ALGORITHM


%par(1) = gamma
%par(2) = beta
%par(3) = A
%par(4) = c
%par(5) = k
%par(6) = alpha
%par(7) = f0

function F=boucwen(par,X)

    vv = [30;diff(X(:,2))/0.00125];
    t = X(:,1);
    tt = t;
    function dz = DiffEq(t,z,vv,tt)

        vv = interp1(tt,vv,t);

        dz = -par(1).*abs(vv).*z.*abs(z)...
            -par(2).*vv.*abs(z).^2+par(3).*vv;

    end


    [T Z] = ode15s(@DiffEq,t,0,[],vv,tt); %SOLVES ODE FOR PROGRESSION
                                          %VARIABLE


F = par(4).*vv+par(5).*X(:,2)+par(6).*Z+par(7);

end
```

```
%DAMPER DATA ANALYSIS AND FITTING

PAR=[];

for i=1

    load([num2str(i) 'A4Hz.mat']) %load data file

    [b,a]=butter(2,0.09); %smooth data using a Butterworth Filter

    F_filter = filter(b,a,C2V)*1000;
    x_filter = filter(b,a,C1V);
    v = diff(C1V)/0.00125;
    v_filter = filter(b,a,v);

    span =100:350;

    t = 0:0.00125:0.00125*(length(span)-1);

    X = [t' x_filter(span) v_filter(span)];


   %Make an initial estimate for the Least Squares Algorithm

    par0 = [2.0005;0.0992;30.0404;2.3690;5.7678;66.5138;-31.2081];

    options=optimoptions(@lsqcurvefit,...
        'MaxFunEval',2000,'MaxIter',2000,'TolX',1e-09);

    [par,resnorm,residual,exitflag,output,lambda,jacobian] =...
   lsqcurvefit(@boucwen,par0,X,F_filter(span),[],[],options);

PAR=[PAR par];

end

F = boucwen(par,X);

  figure(1)
  clf;
  plot(t,F_filter(span),'r')
  hold on
  plot(t,F)

  figure(2)
  clf;
  plot(v_filter(span),F_filter(span),'r')
  hold on
  plot(v_filter(110:350),F(11:length(F)))

% figure(3)
% clf;
% plot(i)
```

```
%CREATE FORCE LOOKUP TABLES FOR A GIVEN CURRENT, DEFLECTION VELOCITY,
%AND ACCELERATION

for i=0.0:0.1:1.1
    load([num2str(i) 'A4Hz.mat'])

    [b,a]=butter(2,0.09); %SMOOTH DATA

    C2V_filter=filter(b,a,C2V);
    C1V_filter=filter(b,a,C1V);
    C1V_velocity=diff(C1V_filter)/0.00125; %DERIVE FOR VELOCITY
    C1V_accel=diff(C1V_velocity)/0.00125; %DERIVE FOR ACCELERATION

    span =126:345;

    X=[C1V_velocity(span) C1V_accel(span) C2V_filter(span)*1000];
    va=[];
    vd=[];
    FFa=[];
    FFd=[];
    for j=1:length(X)
        if X(j,2)>0
            va=[va;X(j,1)];
            FFa=[FFa;X(j,3)];
        else
            vd=[vd;X(j,1)];
            FFd=[FFd;X(j,3)];
        end
    end

    v=-96:1:99;
    Fa(round(i*10+1),v+97) = interp1(va,FFa,v);
    Fd(round(i*10+1),v+97) = interp1(vd,FFd,v);
end

     [vq,iq]=meshgrid(-96:1:99,0:0.01:1.1); %CREATE VELOCITY/CURRENT ARRAYS
     Fqa = interp2(v,0:0.1:1.1,Fa,vq,iq);
     Fqd = interp2(v,0:0.1:1.1,Fd,vq,iq);   %CREATE FORCE MATRIX

     figure
     surf(vq,iq,Fqa,'EdgeColor','none');
     hold on
     surf(vq,iq,Fqd,'EdgeColor','none');
```

```
%CREATE CURRENT LOOKUP TABLES

%DEFLECTIONS UNDERGOING DECELERATIONS
Id1=[];
Id=[];
Fid=[];
vid=[];

for vvdi=-96:1:99 %reverse-interpret current with respect to velocity
    for FFdi=-540:10:480
        Zd=interp2(vq,iq,Fqd,vvdi,iq);
        IId=interp1(Zd,iq,FFdi);
        Id1=[Id1 IId];
    end
    vid=[vid;vvdi];
    Id=[Id;Id1];
    Id1=[];
end

for FFdi=-540:10:480 %create force array
    Fid=[Fid FFdi];
end

%DEFLECTIONS UNDERGOING ACCELERATION
Ia1=[];
Ia=[];
Fia=[];
via=[];

for vvai=-96:1:99 %reverse-interpret current with respect to velocity
    for FFai=-540:10:480
        Za=interp2(vq,iq,Fqa,vvai,iq);
        IIa=interp1(Za,iq,FFai);
        Ia1=[Ia1 IIa];
    end
    via=[via;vvai];
    Ia=[Ia;Ia1];
    Ia1=[];
end

for FFai=-540:10:480 %create force array
    Fia=[Fia FFai];
end

IaH=Ia(:,1:46);

Ia(isnan(Ia))=1.1; %iliminate NAN values due to reverse interpretation
Id(isnan(Id))=1.1;

save('CurrentLookup.mat','Fia','Fid','via','vid','Ia','Id')
```

```
%ANIMATE QUARTER-CAR MODEL

function plotsusp(x,road_x,road_z,curr_x,umf)
% Plots quarter car suspension model at a single instant of time.

% Vehicle positions:
z0 = x(1);          % road elevation
z1 = x(2);          % sprung mass cm deviation
t = x(3);           % current time

% Geometric suspension parameters:
h1 = 0.2;          % resting position of unsprung cm
h2 = 0.9;           % resting position of sprung cm
h3 = 0.3;          % height of sprung mass block
w1 = 0.4;           % width of unsprung mass block
w2 = 0.5;           % width of sprung mass block
w3 = 0.15;          % width of suspension spring
w4 = 0.25;          % spring/damper spacing

% Plotting parameter
fw = 0.7;           % half of figure width

% Preliminary calculations:
x0_r = z0;          % tire spring base position
x0_s = z0+h1;  % suspension spring base position
x0_t = h1+z0;  % unsprung mass block base position
x0_b = h2+z1-h3/2;  % spring mass block base position
L2 = x0_b-x0_s;     % suspension spring length

% Display current simulation time
text(fw/2,1.4,[num2str(t,'%2.1f') ' sec']);

% Plot road profile
dx = road_x(2) - road_x(1);
xstart = max([curr_x-fw,0]);
[~,istart] = min(abs(xstart-road_x));
xend = curr_x + fw;
[~,iend] = min(abs(xend-road_x));
xpstart = xstart-curr_x;
xpend = fw;
zp = road_z(istart:iend)*umf;
xp = xpstart:dx:xpend;
maxi = min([length(xp),length(zp)]);
figure(1);clf
plot(xp(1:maxi),zp(1:maxi),'k-'); hold on

% Plot unsprung mass block
 x0t = [0;x0_t];
 x1t = x0t + [-w1/2;0];
 x4t = x0t + [w1/2;0];
 fill([x1t(1) x4t(1)],[x1t(2) x4t(2)], ...
     [65 105 225]/255); hold on
 axis([-fw fw -0.25 1.5])

% Plot sprung mass block
x0b = [0;x0_b];
x1b = x0b + [-w2/2;0];
x2b = x0b + [-w2/2;h3];
x3b = x0b + [w2/2;h3];
```

```
x4b = x0b + [w2/2;0];
fill([x1b(1) x2b(1) x3b(1) x4b(1)],[x1b(2) x2b(2) x3b(2) x4b(2)], ...
    [65 105 225]/255)

% % Plot tire spring
 x0r = [0;x0_r];
 plot(x0r(1),x0r(2),'ko','MarkerSize',10,'MarkerFaceColor','k')
 x1r = x0r + [0;h1];
 plot([x0r(1) x1r(1)], [x0r(2) x1r(2)], 'k-','LineWidth',2)

% Plot suspension spring
x0s = [-w4/2;x0_s];
u = L2/9;
x1s = x0s + [0;u];
x2s = x0s + [-w3/2;3/2*u];
x3s = x2s + [w3;u];
x4s = x3s + [-w3;u];
x5s = x4s + [w3;u];
x6s = x5s + [-w3;u];
x7s = x6s + [w3;u];
x8s = x7s + [-w3;u];
x9s = x8s + [w3/2;u/2];
x10s = x9s + [0;u];
plot([x0s(1) x1s(1) x2s(1) x3s(1) x4s(1) x5s(1) ...
    x6s(1) x7s(1) x8s(1) x9s(1) x10s(1)], ...
    [x0s(2) x1s(2) x2s(2) x3s(2) x4s(2) x5s(2) ...
    x6s(2) x7s(2) x8s(2) x9s(2) x10s(2)], 'k-','LineWidth',3)

% Plot suspension damper
x0d = [w4/2;x0_s];
a = 0.7*(h2-h1-h3/2); b = L2-a; c = 0.3*w3;
x1d = x0d + [-c;a];
x2d = x0d + [-c;0];
x3d = x0d + [c;0];
x4d = x0d + [c;a];
x5d = x0d + [-c;b];
x6d = x0d + [c;b];
x7d = x0d + [0;L2];
x8d = x0d + [0;b];
plot([x1d(1) x2d(1) x3d(1) x4d(1)], ...
    [x1d(2) x2d(2) x3d(2) x4d(2)], 'k-','LineWidth',2);
plot([x5d(1) x6d(1)],[x5d(2) x6d(2)], 'k-','LineWidth',4);
plot([x7d(1) x8d(1)],[x7d(2) x8d(2)],'k-','LineWidth',2);
```

```
% Clear workspace and set plotting flags
clear;
ploton1 = 1;            % animate qcar response
ploton2 = 2;            % plot response
ploton3 = 3;
ploton4 = 4;
ploton5 = 5;
ploton6 = 6;
% Initialize vehicle parameters:

k = 13000;
m = 150;                                % 1/4 sprung mass (kg)
dt = 0.01;                             % simulation time step
tmax = 5;                               % simulation time length
t = 0:dt:tmax;                          % time/space steps for output

G=1000;
maxcur=0.5;
% Initialize simulation
x0 = [0 0]';                            % initial state

u1 = 0.0028*sin(2*pi*4*t)+0*sin(2*pi*20*t);
v2 = [0 diff(u1)/dt];

load DataLookup                        % damper characteristics data
load CurrentLookup             % reverse current model
load Currents

ii=[0 0.1 0.2 0.3 0.4 0.5 0.6 0.7 0.8 0.9 1];

umf = 1;

% Construct linear state space model
Aqcar = [0 1;-k/m 0];
Bqcar = [0 0; k/m 1/m]; Cqcar = [1 0; 0 1];
Dqcar = 0;
qcar = ss(Aqcar,Bqcar,Cqcar,Dqcar);


% Matrices Required for Reduced Order Observer
Aaa = Aqcar(1,1);
Aab = Aqcar(1,2);
Aba = Aqcar(2,1);
Abb = Aqcar(2,2);

Ba = Bqcar(1);
Bb = Bqcar(2);
Lo = 3;

% Definition of System States:
% x(1) = z1             mass displacement
% x(2) = z1dot          mass velocity

y = [0 0];
ff= zeros(1,2);
force= 0;
current=[];
f=0;
```

```
method='nearest';

%%%%%%%%%%%%%%%%%%%%%%%%%%%%%%%%%%%%%%%%%%%%%%%%%%%%%%%%%%%%%%%%%%%%%%%%%%%%
%%%%%%%%%%%%%%%%%%%%%%%%%%%%%%%%%%%%%%%%%%%%%%%%%%%%%%%%%%%%%%%%%%%%%%%%%%%%

% CASE 1:         CLIPPED OPTIMAL CONTROL
% CASE 2:         FULL LQR CONTROL
% CASE 3:         SKYHOOK CONTROL
% CASE 4:         FIXED MINIMUM DAMPING
% CASE 5:         FIXED MAXIMUM DAMPING
% CASE 6:         FUZZY SKYHOOK CONTROL

%%%%%%%%%%%%%%%%%%%%%%%%%%%%%%%%%%%%%%%%%%%%%%%%%%%%%%%%%%%%%%%%%%%%%%%%%%%%
%%%%%%%%%%%%%%%%%%%%%%%%%%%%%%%%%%%%%%%%%%%%%%%%%%%%%%%%%%%%%%%%%%%%%%%%%%%%


C = 6;                % SPECIFY CONTROLLER CASE
switch C
    case 1
        %-----------------------------------------------------------------
        %-----------------------------------------------------------------
        %
        %                          CLIPPED LQR CONTROL
        %
        %-----------------------------------------------------------------
        %-----------------------------------------------------------------

        % LQR Parameters
        Q = [100 0; 0 1];
        R = 0.0000001;
        [K,S,e] = lqr(Aqcar,Bqcar(:,2),Q,R);

        for i=1:length(t)-1

            u = [u1(i:i+1);ff]';
            yy = lsim(qcar,u*umf,0:dt:dt,x0);
            y =[y; yy(end,:)];
            x0 = y(end,:);
            v1=yy(:,2);
            a1=diff(v1)/dt;
            a1=a1(end);
            v12=v1-v2(i:i+1)';
            a12=diff(v12)/dt;
            a12=a12(end);
            vv1=v1(end);
            vv12=v12(end);


            if a12>=0
                F_v12_max = -interp2(vq,iq,Fqa,vv12*G,maxcur,method);
                F_v12_min = -interp2(vq,iq,Fqa,vv12*G,0,method);
            else
                F_v12_max = -interp2(vq,iq,Fqd,vv12*G,maxcur,method);
                F_v12_min = -interp2(vq,iq,Fqd,vv12*G,0,method);
            end

            f = -K*x0';

            if F_v12_max>=0
```

```
            if f>0
                if F_v12_max<f
                    f = F_v12_max;
                elseif F_v12_min>f
                    f = F_v12_min;
                end
            else f = F_v12_min;
            end
        else
            if f<0
                if F_v12_min<f
                    f = F_v12_min;
                elseif F_v12_max>f
                    f = F_v12_max;
                end
            else f=F_v12_min;
            end
        end

%           if abs(F_v12_max)<abs(f)
%               f = F_v12_max;
%           elseif abs(F_v12_min)>abs(f)
%               f = F_v12_min;
%           end

        ff = [ff(end) f];

        force = [force f];

        if a12>=0
            current_i = interp2(Fia,via,Ia,f,vv12*G,method,1);
        else
            current_i = interp2(Fid,vid,Id,f,vv12*G,method,1);
        end
        current = [current current_i];

    end


case 2
    %-----------------------------------------------------------------
    %-----------------------------------------------------------------
    %
    %                          FULL LQR CONTROL
    %
    %-----------------------------------------------------------------
    %-----------------------------------------------------------------

    % LQR Parameters
    Q = [100 0; 0 1];
    R = 0.0000001;
    [K,S,e] = lqr(Aqcar,Bqcar(:,2),Q,R);

    for i=1:length(t)-1

        u = [u1(i:i+1);ff]';
        yy = lsim(qcar,u*umf,0:dt:dt,x0);
        y =[y; yy(end,:)];
        x0 = y(end,:);
```

```
        v1=yy(:,2);
        a1=diff(v1)/dt;
        a1=a1(end);
        v12=v1-v2(i:i+1)';
        a12=diff(v12)/dt;
        a12=a12(end);
        vv1=v1(end);
        vv12=v12(end);


        f = -K*x0';


        ff = [ff(end) f];

        force = [force f];

        if a12>=0
            current_i = interp2(Fia,via,Ia,f,vv12*G,method);
        else
            current_i = interp2(Fid,vid,Id,f,vv12*G,method);
        end
        current = [current current_i];
    end


case 3
    %-----------------------------------------------------------------
    %-----------------------------------------------------------------
    %
    %                        SKYHOOK CONTROL
    %
    %-----------------------------------------------------------------
    %-----------------------------------------------------------------

    alpha=0.9;


    for i=1:length(t)-1
        %ff= zeros(1,2);
        u = [u1(i:i+1);-ff]';
        yy = lsim(qcar,u*umf,0:dt:dt,x0);
        y =[y; yy(end,:)];
        x0 = y(end,:);
        v1=yy(:,2);
        a1=diff(v1)/dt;
        a1=a1(end);
        v12=v1-v2(i:i+1)';
        a12=diff(v12)/dt;
        a12=a12(end);
        vv1=v1(end);
        vv12=v12(end);

        if a12>=0
            F_v12_max = interp2(vq,iq,Fqa,vv12*G,maxcur,method);
            F_v12_min = interp2(vq,iq,Fqa,vv12*G,0,method);
        else
            F_v12_max = interp2(vq,iq,Fqd,vv12*G,maxcur,method);
```

```
            F_v12_min = interp2(vq,iq,Fqd,vv12*G,0,method);
        end
        if a1>=0
            F_v1_max = -interp2(vq,iq,Fqa,vv1*G,maxcur,method);
            F_v1_min = -interp2(vq,iq,Fqa,vv1*G,0,method);
        else
            F_v1_max = -interp2(vq,iq,Fqd,vv1*G,maxcur,method);
            F_v1_min = -interp2(vq,iq,Fqd,vv1*G,0,method);
        end

        if vv1*vv12>0
            f=alpha*F_v12_max+(1-alpha)*F_v1_max;
            if f>F_v12_max
                f=F_v12_max;
            end
            if f<F_v12_min
                f=F_v12_min;
            end
        else
            f=F_v12_min;
        end

        ff=[ff(end) f];

        force = [force f];

        if a12>=0
            current_i = interp2(Fia,via,Ia,f,vv12*G,method);
        else
            current_i = interp2(Fid,vid,Id,f,vv12*G,method);
        end
        current = [current current_i];
    end


case 4
    %-----------------------------------------------------------------
    %-----------------------------------------------------------------
    %
    %                         Minimum Damping
    %
    %-----------------------------------------------------------------
    %-----------------------------------------------------------------

    for i=1:length(t)-1
        %ff= zeros(1,2);
        u = [u1(i:i+1);-ff]';
        yy = lsim(qcar,u*umf,0:dt:dt,x0);
        y =[y; yy(end,:)];
        x0 = y(end,:);
        v1=yy(:,2);
        a1=diff(v1)/dt;
        a1=a1(end);
        v12=v1-v2(i:i+1)';
        a12=diff(v12)/dt;
        vv1=v1(end);
        vv12=v12(end);

        if a12>=0
```

```
            f = interp2(vq,iq,Fqa,vv12*G,0,method);
        else
            f = interp2(vq,iq,Fqd,vv12*G,0,method);
        end

        ff=[ff(end) f];

        force = [force f];

        if a12>=0
            current_i = interp2(Fia,via,Ia,f,vv12*G,method);
        else
            current_i = interp2(Fid,vid,Id,f,vv12*G,method);
        end
        current = [current current_i];
    end

case 5
    %-----------------------------------------------------------------
    %-----------------------------------------------------------------
    %
    %                        Maximum Damping
    %
    %-----------------------------------------------------------------
    %---------------------------------------------------------------


    for i=1:length(t)-1
        %ff= zeros(1,2);
        u = [u1(i:i+1);ff]';
        yy = lsim(qcar,u*umf,0:dt:dt,x0);
        y =[y; yy(end,:)];
        x0 = y(end,:);
        v1=yy(:,2);
        a1=diff(v1)/dt;
        a1=a1(end);
        v12=v1-v2(i:i+1)';
        a12=diff(v12)/dt;
        a12=a12(end);
        vv1=v1(end);
        vv12=v12(end);

        if a12>=0
            f = -interp2(vq,iq,Fqa,vv12*G,maxcur,method);
        else
            f = -interp2(vq,iq,Fqd,vv12*G,maxcur,method);
        end

        ff=[ff(end) f];

        force = [force f];

        if a12>=0
            current_i = interp2(Fia,via,Ia,f,vv12*G,method);
        else
            current_i = interp2(Fid,vid,Id,f,vv12*G,method);
        end
        current = [current current_i];
```

```
        end


%-----------------------------------------------------------------
%-----------------------------------------------------------------
%
%                       Fuzzy Skyhook Control
%
%-----------------------------------------------------------------
%-----------------------------------------------------------------
    case 6

        fismat = readfis('SkyhookFuzzy');

        for i=1:length(t)-1
            u = [u1(i:i+1);-ff]';
            yy = lsim(qcar,u*umf,0:dt:dt,x0);
            y =[y; yy(end,:)];
            x0 = y(end,:);
            v1=yy(:,2);
            a1=diff(v1)/dt;
            a1=a1(end);
            v12=v1-v2(i:i+1)';
            a12=diff(v12)/dt;
            a12=a12(end);
            vv1=v1(end);
            vv12=v12(end);

            cur = evalfis([vv1; vv12],fismat);

            if a12>=0
                f = interp2(vq,iq,Fqa,vv12*G,cur,method);
            else
                f = interp2(vq,iq,Fqd,vv12*G,cur,method);
            end

            ff=[ff(end) f];

            force = [force f];

            current = [current cur];
        end

end

%-----------------------------------------------------------------
%-----------------------------------------------------------------
%-----------------------------------------------------------------
%-----------------------------------------------------------------

deltamaxf = max(abs(y(:,1)));           % max x3 amplitude
z2dotdot = [0 diff(y(:,2))'/dt]./9.8;       % sprung mass acceleration
z0dotdot = [0 diff(v2)/dt]./9.8;

%-----------------
%  PLOT CONTROL
%-----------------
```

```
% % animate response
% if ploton1
%     z0 = u1'; % road elevation
%     z1 = y(:,1);
% z1 = z0 + y(:,1);             % mass position
% zmf = 1;                       % exaggerate response for visualization
%     for i=1:length(t)
%         plotsusp([z0(i), z1(i)*zmf, t(i)],u1');
%         refresh
%     end
% end

% % plot response
% if ploton2
%     figure(2);clf
%     plot(t,y(:,1),'g-')
%     hold on
%     plot(t,u1*umf)
%     legend('mass position', ...
%         'base elevation')
%     xlabel('Time (s)')
%     ylabel('Displacement (m)')
% end

% % plot force
% if ploton3
%     figure(3);hold on
%     plot(t,force,'r-')
%     legend('damper force')
%     xlabel('Time (s)')
%     ylabel('Force (N)')
% end

% % plot acceleration
% if ploton4
%     figure(4);clf
%     plot(t,z2dotdot,'r-')
%     hold on
%     plot(t,z0dotdot,'b-')
%     legend('mass acceleration','base acceleration')
%     xlabel('Time (s)')
%     ylabel('acceleration (N)')
% end

% plot current
if ploton4
    figure(4);clf
    plot(t(2:end),current,'r-')
    legend('input current')
    xlabel('Time (s)')
    ylabel('Current (A)')
end

% if ploton5
%     figure(5);clf
%     NFFT = 2^nextpow2(length(t)); % Next power of 2 from length of y
% % Y = fft(z2dotdot,NFFT)/length(t);
% Y = fft(y(:,1),NFFT)/length(t);
% YG = fft(u1,NFFT)/length(t);
```

```
% fHz = 0.5*1/dt*linspace(0,1,NFFT/2+1);
%
% % Plot single-sided amplitude spectrum
% plot(fHz,2*abs(Y(1:NFFT/2+1)))
% hold on
% plot(fHz,2*abs(YG(1:NFFT/2+1)),'r-')
% % title('Single-Sided Amplitude Spectrum of y(t)')
% xlabel('Frequency (Hz)')
% ylabel('|Y(f)|')
% end

if ploton6
    figure(6);
    start=10;
    NFFT = 2^nextpow2(length(t-start+1)); % Next power of 2 from length of y
    Ya = fft(z2dotdot(start:end),NFFT)/(length(t-start+1));
    YGa = fft(z0dotdot(start:end),NFFT)/(length(t-start+1));
    fHz = 0.5*1/dt*linspace(0,1,NFFT/2+1);

    % Plot single-sided amplitude spectrum
    plot(fHz,2*abs(YGa(1:NFFT/2+1)),'r-')
    hold on
    plot(fHz,2*abs(Ya(1:NFFT/2+1)),'b-')
    xlabel('Frequency (Hz)')
    ylabel('Acceleration (g)')
    legend('Mass Acceleration','Base Acceleration')
    xlim([0 20])
end
```

```
%CREATE TRANSMISIBILITY GRAPH WITH FREQUENCY RATIO IN QUESTION

zeta=[0.05 0.1 0.5 1];

r=0:0.01:3;
clf
hold on
c=['b' 'g' 'c' 'm'];

for i=1:length(zeta)
    T=sqrt((1+(2.*zeta(i).*r).^2)./((1-r.^2).^2+(2.*zeta(i).*r).^2));
    plot(r,T,'Color',c(i))
end

hx2 = graph2d.constantline(sqrt(2), 'LineStyle',':', 'Color',[.7 .7 .7]);
changedependvar(hx2,'x'); %DRAW VERTICAL LINE AT DESIRED FREQUENCY RATIO

xlabel('Frequency Ratio $\frac{\omega}{\omega_n}$','interpreter','latex')
ylabel('Transmissibility (T)')

legend('\zeta = 0.05','\zeta = 0.1','\zeta = 0.5','\zeta = 1')
```